Quantum Field Theoretical Aspects of Black-Hole Formation

-

On Propagation, Consistency and Quantum Graphs

Maximilian Kögler

München 2022

Quantum Field Theoretical Aspects of Black-Hole Formation

-

On Propagation, Consistency and Quantum Graphs

Maximilian Kögler

Dissertation
an der Fakultät für Physik
der Ludwig–Maximilians–Universität
München

vorgelegt von
Maximilian Kögler
aus Fürstenfeldbruck

München, den 27. Mai 2022

Erstgutachter: Prof. Dr. Stefan Hofmann
Zweitgutachter: Prof. Dr. Gerhard Buchalla
Tag der mündlichen Prüfung: 21. Juli 2022

Contents

List of Figures

Zusammenfassung

Die vorliegende Arbeit wirft Licht auf die Entstehung Schwarzer Löcher und ihre Quantenkonsistenz. Die Kombination der fundamentalsten Theorien, Quantenfeldtheorie und Allgemeinen Relativitätstheorie, führt bei der Betrachtung Schwarzer Löcher zum Informationsparadoxon, welches auf die Unvereinbarkeit beider Theorien hinweist. Da dieses Paradoxon in seiner Art einzigartig ist, stellt es eine herausragende Gelegenheit dar, durch seine Auflösung grundlegende Gesetzmäßigkeiten der Natur zu entdecken.

In dieser Arbeit untersuchen wir, ob bereits die Entstehung eines Schwarzen Lochs zu Inkonsistenzen führt und so auf das Informationsparadoxon schließen lässt. Zu diesem Zweck verwenden wir eine massive Schale und halten diese im Gleichgewicht für verschiedene Radien. Mit diesem Aufbau simulieren wir die Entstehung eines Schwarzen Lochs, unmittelbar davor, währenddessen und danach. Auf diesem gravitativen Hintergrund verwenden wir Quantenfelder um mögliche Inkonsistenzen aufzuspüren.

Ein wesentlicher Teil dieser Arbeit besteht in der Herleitung der Dynamik von Quantenfeldern im System einer ruhenden Schale. Hierfür entwickeln wir zwei unterschiedliche Herangehensweisen, die die Dynamik von Quantenfeldern über Grenzflächen hinweg bestimmt. Da es sich hierbei um ein Paradebeispiel der Optik handelt, leiten wir diese Techniken an bereits vollständig gelösten optischen Systemen ab und erhalten dadurch zugleich neue Methoden zur Lösung komplizierter optischer Systeme.

Mit diesem Vorgehen bestimmen wir die Quantenfelder in einer lokalen Umgebung der Schale einerseits mit Hilfe des Äquivalenzprinzips und andererseits mit Informationsnetzwerken. Letztere konstruieren wir aus Quantengraphen, welche einen neuartigen Ansatz zur Bestimmung von Quantenfeldern in komplizierten Umgebungen darstellen. Insbesondere der Kompromiss zwischen technischer Einfachheit und Präzision kann so auf einzigartiger Weise gestaltet werden.

Mit diesem lokalen Ansatz untersuchen wir die Vakuumpersistenz auf Inkonsistenzen. Im Rahmen unserer Untersuchung stellen wir fest, dass die Entstehung eines Schwarzen Lochs keine Widersprüche erzeugt und somit nicht als relevanter Teil des Informationsparadoxes angesehen werden kann. Darüber hinaus legen wir dar, wie weitere Anwendungen von Quantenfeldern in komplizierten gravitativen oder optischen Hintergründen mit unseren entwickelten Methoden analysiert werden können.

Abstract

This thesis sheds light on the quantum consistency of black-hole formation. When examining black-holes, the combination of the most fundamental theories, quantum field theory and general relativity, leads to the information paradox. This paradox exposes the incompatibility of these theories and since it is one of a kind, solving it offers an unparalleled opportunity to discover fundamental laws of nature.

In this work, we investigate whether the formation of a black-hole already hints to inconsistencies and consequently to the information paradox. For this purpose, we construct a massive shell and maintain it balanced at various radii. With this arrangement, we simulate a collapsing shell before, during, and after it has formed a black-hole. Quantum fields are then utilized to reveal possible inconsistencies during these stages.

Deriving the dynamics of quantum fields in the system of a stabilized shell is an essential element of this work. To this end, we develop two distinct techniques to determine the dynamics of quantum fields across interfaces. Since this is a prime example of optics, we derive these approaches from fully solved optical systems, thereby acquiring novel opportunities for the analysis of sophisticated optical systems.

With this procedure, we determine the quantum fields in a local environment of the shell using the equivalence principle on the one hand and information networks on the other. The latter are constructed by quantum graphs, which provide a new technique for deriving quantum fields in complicated environments. Most notably, the trade-off between technical simplicity and precision may be individually tailored in this approach.

Using this local framework, we examine the vacuum persistence for inconsistencies. Within the scope of our study, the formation of a black-hole does not cause anomalies and thus cannot be regarded as a relevant aspect of the information paradox. In addition, we elaborate how the techniques we have developed can be used to study other applications of quantum fields in challenging gravitational or optical environments.

1. Introduction

Black-holes have emerged as one of physics' most fascinating phenomena, providing both astounding predictions and a deeper understanding of our most fundamental theories. Recently, ground-breaking observational studies of black-hole mergers [1] and of the black-holes at the cores of Messier 87 [2] and the Milky Way [3] have been published. With this solidified foundation in place, we can address other intriguing black-hole mysteries, such as those that go beyond the classical level. Most notably, quantum effects in a black-hole system ultimately lead to the information paradox [4–6]. Due to this paradox, it is still unclear how the most profound theories, general relativity and quantum field theory, can be combined to adequately describe black-holes [7,8]. As a result, this paradox represents an unparalleled opportunity to push the boundaries of knowledge.

In this thesis, we investigate whether traces of this puzzle can be identified during the formation of a black-hole in a classical gravitational collapse. Despite significant progress, technical difficulties have so far prevented a complete semiclassical description of black-hole formation [9–11]. As we argued in [12], due to the locality of quantum field theory we believe that inconsistencies in black-hole formation can be detected in a local environment that includes a fraction of the forming horizon. This local perspective allows for the application of the equivalence principle and simplifies the investigation greatly. We use quantum field theory in curved spacetimes to study the formation of black-holes by posing the following questions in a local framework:

- How does the emergence of an apparent horizon disrupt quantum communication and affect the entanglement entropy?
- Do quantum fields evolve consistently during black-hole formation?

The first question concerns whether and how causality is respected, which requires that once the black-hole is formed, no information is allowed to leave its interior. The second question seeks to determine whether the semiclassical approach breaks down during the formation process, hence pointing to the information paradox. This observation would be in line with other arguments that a non-perturbative description of black-holes[1] is required to solve the information paradox [21–24].

[1]Explicit non-perturbative models of black-holes are for example discussed in [13–20].

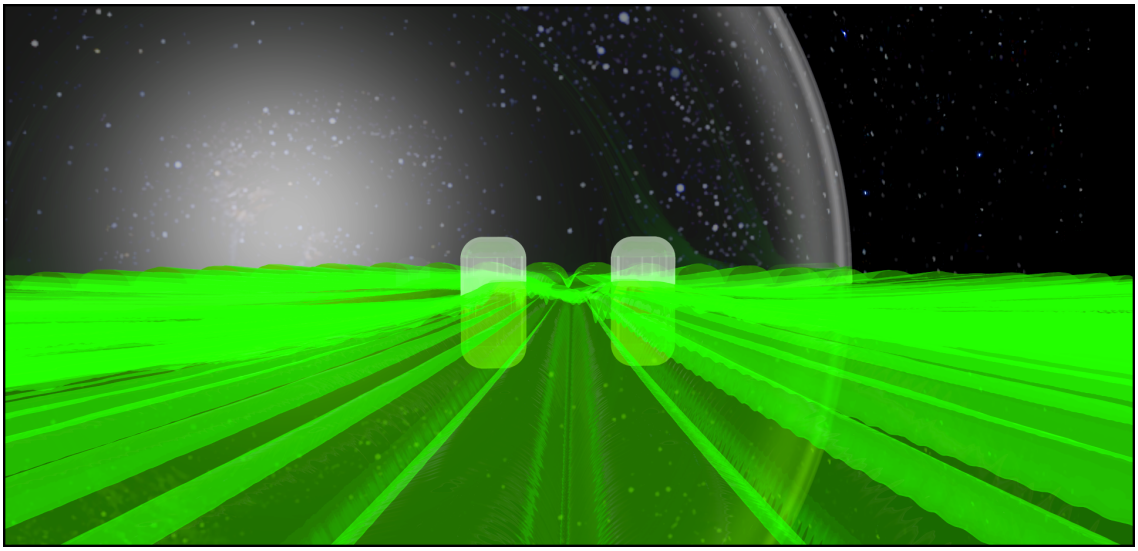

Figure 1.1.: The probability density of a quantum field displayed in green due to the influence of two glass pillars in a Double-slit-like arrangement placed in the gravitational background of a thin shell. The probability density is calculated using the methods presented in this thesis, and the artistic rendering is done using ray-tracing.

To address these questions, we will develop techniques that determine how a quantum field propagates in the gravitational background of a collapsing thin shell, and hence in systems with interfaces. These methods allow the investigation of a wide range of other applications, such as the study of decoherence in gravitational backgrounds [25–27]. In Fig. 1.1, we illustrate a potential Double-slit-like setup for investigating decoherence in the presence of a forming black-hole. The key features here are the propagation in a curved background through interfaces, such as through the surface of the shell and equivalently the glass columns depicted in Fig. 1.2b) and Fig. 1.2c), respectively. We create and test our ideas in optical and gravitational systems which possess different interfaces to demonstrate their broad applicability in Chapter 2.

As we will see, near the formation of a black-hole through a collapsing shell, non-perturbative techniques must be used to compute quantum fields in this background. In Sec. 3.1, we apply the equivalence principle to describe the geometry of a thin shell in a local environment using normal coordinates [28–35] as illustrated in Fig. 1.2a). We use the procedure developed in [36] to determine the size of the normal environment and the allowed frequency range for the shell geometry. Because of these constraints, we must limit ourselves to high-frequency field modes, making our investigation complementary to the well-known gray body calculation performed in the low-frequency regime [21]. We continue in Sec. 3.2 by examining a massive thin shell made up of matter that satisfies the condition of strong and dominant energy. Stabilizing the shell, we treat its radius as a free parameter to investigate the various stages of black-hole formation individually.

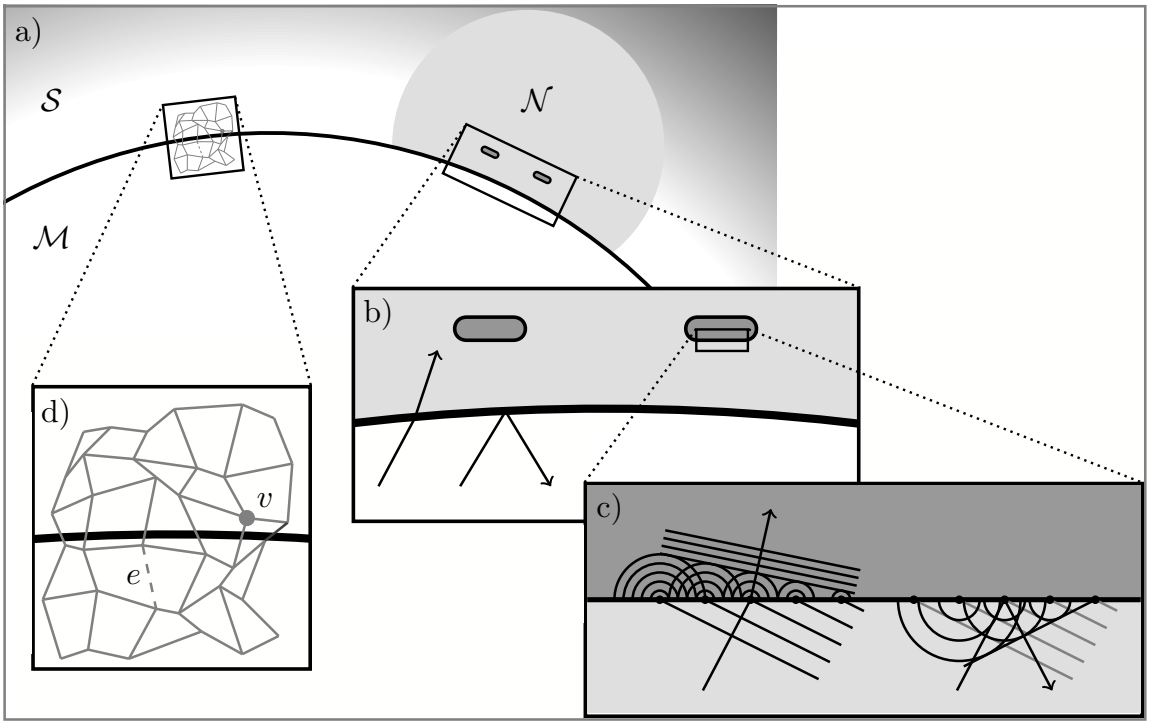

Figure 1.2.: Overview over the different setups we consider throughout the thesis to obtain the propagation of a quantum field in the gravitational geometry of a collapsing thin shell. In a) is a collapsing shell schematically depicted with Minkowski background $\mathcal{M}$ in its interior and Schwarzschild geometry $\mathcal{S}$ in its exterior. Additionally, a normal neighborhood $\mathcal{N}$ is constructed in which the two glass columns of the setup in Fig. 1.1 are placed. The propagation across the shell surface is seen in b) in a zoomed-in view of the glass column configuration. In c), the Huygens principle is depicted schematically for transmission and reflection at a vacuum-glass interface. We also explore the propagation of a quantum field for a collapsing shell background on a quantum graph composed of straight edges such as e and vertices such as v in d).

With the local description of a stabilized shell, we derive the propagation of quantum fields in Sec. 3.3, and investigate the two questions outlined above. First, we conduct a communication experiment by transmitting a signal from the inside to the outside of the shell in Sec. 3.3.3. Second, in Chapter 4 we calculate the vacuum persistence amplitude of the Minkowski vacuum inside the shell to check whether quantum fields evolve consistently during black-hole formation. In particular, we place an external source inside the shell and test for an inertial observer whether the vacuum state of a scalar field evolves according to the principles of quantum field theory. For that matter, in Sec. 4.2 and [37], we first study dynamical vacuum effects in the setting of atom physics. There, vacuum effects induced by the Coulomb potential serve as a well-tested analogue for vacuum effects caused by a black-hole geometry. All of these vacuum-induced phenomena are anticipated from the viewpoint of open quantum systems, from which we adapt renormalization techniques to quantum field theory in curved spacetimes and obtain a fundamental physical

interpretation. In particular, we interpret quantum field theory in curved spacetimes as an open quantum system in Sec. 4.1 and [38].

In Chapter 5, a second approach is used to extend this research to dynamical black-hole formation with a collapsing shell. In this framework, we embed quantum graphs made up of edges connected by vertices in the background of a thin shell as depicted in Fig. 1.2d). The edges provide an inherently $(1+1)$ dimensional support for the quantum fields, whilst the vertices are reflecting and transmitting impurities that encode physical properties of the background. Since this technique allows us to calculate local observables in a totally different manner compared to the normal neighborhood approach, we may use both to verify and supplement each other's results. For example, when the gravitational background can be adequately described through adiabatic expansion, as we establish for a fixed shell in Chapter 3, the local description of quantum fields in normal neighborhoods is especially favorable. This technique, however, reaches its limits when the geometry is more challenging, such as that of a collapsing shell. Because the latter includes the formation of an apparent horizon, we intend to employ quantum graphs, which can circumvent the technical challenges of obtaining observables like the entanglement entropy, as demonstrated in Sec. 5.2 and [39].

Quantum graphs offer two important features that make computing observables of quantum fields in curved spacetimes simpler than ever before. To begin, the induced spacetime on each $(1+1)$ dimensional edge is conformally flat, considerably simplifying the calculations of observables. This simplification, in particular, allows us to do analytic and non-perturbative calculations of quantum fields while still addressing $(3+1)$ dimensional physics. Furthermore, the complexity of the quantum graph may be adjusted to the situation at hand. Morally, this is similar to restricting the path integral in $(3+1)$ dimensions to a subset of particularly relevant paths. This greatly reduces the parameter space of quantum field theory, allowing us to explore apparent horizon formation and many more applications of quantum fields in complicated optical or gravitational backgrounds.

Finally, in Chapter 6, we summarize our findings and offer some suggestions for future projects. In this work we use the metric signature $\mathrm{diag}(-,+,+,+)$ and Planck units with $c = G = \hbar = 1$. The indices of the equation numbers denote acronyms for principles, approximations, and constraints on which the equation in question relies. These acronyms are defined in App. A.

2. Propagation Across Interfaces

As outlined in the introduction, we begin by analyzing how fields evolve in optical systems that have boundaries and interfaces. Therefore, as a first step we consider a massless, real scalar field ϕ coupled to an external source J in a spacetime filled with a medium. We choose a medium which effect on the field can be described by a constant susceptibility ε, modifying the dispersion relation. In the rest frame of the medium, the equation of motion in three spatial dimensions using the Cartesian coordinates $(t, \mathbf{x})$ reads

$$\Box_x^\varepsilon \phi := \left(-\varepsilon \partial_t^2 + \partial_{\mathbf{x}}^2\right) \phi = J \,. \tag{2.1}$$

This differential equation is solved with a plane wave ansatz $\exp\{i(\omega_k^\varepsilon t - \mathbf{kx})\}$ with momentum $\mathbf{k}$. The resulting dispersion relation is thus $(\omega_k^\varepsilon)^2 = \mathbf{k}^2/\varepsilon$.

The equation of motion (2.1) can be conveniently obtained by introducing an auxiliary metric $\eta_\varepsilon = \mathrm{diag}(-1/\varepsilon, 1, 1, 1)$ for the kinetic contraction of a scalar field action in a Minkowski background. This action is composed of the free part S_0^ε, the source term S_J and is expressed by

$$S_0^\varepsilon + S_J = -\frac{1}{2} \int_B \mathrm{d}\mu_x \, \left(\eta_\varepsilon^{\mu\nu} \partial_\mu \phi \partial_\nu \phi + 2\phi J\right) , \tag{2.2}$$

with measure $\mathrm{d}\mu_x = \mathrm{d}^4x \sqrt{-\det(\eta)}$, Minkowski metric η and with support of the integral over the whole Minkowski spacetime, i.e. $B = \{x : x \in \mathbb{R}^4\}$.

To answer the questions raised in the introduction, we will utilize quantum fields and thus promote ϕ to operators. The key object we are interested in is the Feynman propagator, which is obtained by computing the time-ordered correlator evaluated in the vacuum state $|0\rangle$,

$$\Delta_{xy}^\varepsilon := i\langle \mathrm{T}\phi_x \phi_y \rangle \,, \tag{2.3}$$

where T denotes the time ordering, $\langle \,.\, \rangle := \langle 0| \,.\, |0\rangle$ and where we take the shorthand notation $f_x := f(x)$ and $f_{xy} := f(x, y)$ for any function or distribution $f(x)$, $f(x, y)$. This

propagator satisfies the fundamental equation

$$\Box^{\varepsilon}\Delta^{\varepsilon}_{xy} = -\delta^{(4)}_{xy}\,, \tag{2.4}\,{}^{b}_{\mathcal{H}\mathcal{S}}$$

with the Dirac delta distribution δ and appropriate boundary conditions implied. The propagator (2.3) can then be expressed as [40]

$$\Delta^{\varepsilon}_{xy} = -\int \frac{\mathrm{d}^4k}{(2\pi)^4}\frac{e^{-ik(x-y)}}{\eta^{\mu\nu}_{\varepsilon}k_\mu k_\nu - i\epsilon} = \Theta_{x^t y^t}G^{\varepsilon}_{xy} + \Theta_{y^t x^t}G^{\varepsilon}_{yx}, \tag{2.5}\,{}^{b}_{\mathcal{H}\mathcal{S}}$$

with Heaviside step function Θ and Wightman distribution $G^{\varepsilon}_{xy} := i\langle\phi_x\phi_y\rangle$ given by

$$G^{\varepsilon}_{xy} = \int_k^{\varepsilon} e^{ik_\perp(x^\perp - y^\perp)}\,, \tag{2.6}\,{}^{b}_{\mathcal{H}\mathcal{S}}$$

with the shorthand

$$\int_k^{\varepsilon} := i\int \frac{\mathrm{d}^3k}{(2\pi)^3 2\omega^{\varepsilon}_k\,\varepsilon}e^{-i\omega^{\varepsilon}_k(x^t-y^t)}e^{i\mathbf{k}_\parallel(\mathbf{x}^\parallel-\mathbf{y}^\parallel)}\,. \tag{2.7}\,{}^{b}_{\mathcal{H}\mathcal{S}}$$

Here, for later convenience, the spacetime coordinates are denoted as $x^\mu = \left(x^t, x^\perp, \mathbf{x}^\parallel\right)$ and the spatial momenta $\mathbf{k} = (k_\perp, \mathbf{k}_\parallel)$. In the next Sections, we derive with different approaches an expression for the Feynman propagator that is valid in systems with boundaries and regions with different susceptibilities. Both approaches have significant advantages and applicability, and they will be crucial in determining the propagator in a black-hole scenario in Chapter 4.

2.1. Non-Perturbative Approach via Matching Conditions

2.1.1. Reflection at Boundaries

Let us now introduce a boundary to the system filled with a medium as described above. We do so by modifying the support of the integral B in Eq. (2.2) such that the action now describes a system that is spatially constrained. The external source J is then placed in the bulk, meaning it has no overlap with the boundary $\mathrm{Supp}(J)\cap\partial B = 0$, and the scalar field is used to analyze the boundary ∂B. For simplicity, we first consider a planar boundary with $x^\perp = 0$ using Cartesian coordinates as depicted in Fig. 2.1. With this

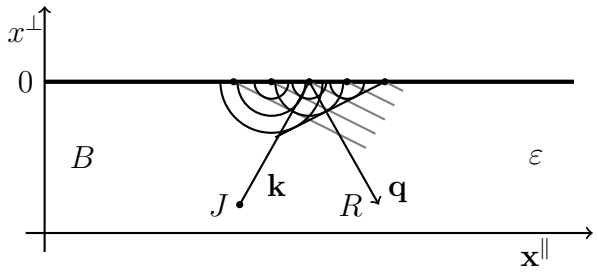

Figure 2.1.: Setup of a half-space $B = \{x : x^\perp < 0\}$ with susceptibility ε. This half-space system possesses a planar boundary at $x^\perp = 0$ and is unconstrained in the $\mathbf{x}^\parallel$ directions. The Huygens' principle is sketched for a plane wave caused by the external source J with a wave vector $\mathbf{k}$ and for the reflected wave R with a wave vector $\mathbf{q}$.

setup, varying the action (2.2) with $B = \{x : x^\perp < 0\}$ leads to the equation of motion

$$\Box_x^\varepsilon \phi + \delta_{x^\perp} \partial_{x^\perp} \phi = J \,. \tag{2.8}\,{}^b_{\mathcal{H}\,\mathcal{S}}$$

Interpreting this relation as the equation of motion in the bulk together with a condition for the field ϕ at the boundary, the propagator in the bulk Δ_{xy}^ε fulfills

$$\Box_x^\varepsilon \Delta_{xy}^\varepsilon = \delta_{xy}^{(4)} \,. \tag{2.9}\,{}^b_{\mathcal{H}\,\mathcal{S}}$$

This propagator is not affected by the boundary and therefore contains no reflection off the boundary. We take this effect into account by exploiting Huygens' principle $\mathcal{H}$.

According to the Huygens' principle, the field configuration on the boundary acts like a source for the reflected field as illustrated in Fig. 2.1. Thus, we take the following ansatz for the whole field configuration

$$\phi_x = \int \mathrm{d}\mu_z \left(\Delta_{xz}^\varepsilon J_z + \delta_{z^\perp} \Delta_{xz}^\varepsilon \overset{\leftrightarrow}{\partial}_{z^\perp} \phi_z \right) , \tag{2.10}\,{}^b_{\mathcal{H}\,\mathcal{S}}$$

where $f \overset{\leftrightarrow}{\partial}_{z^\perp} g = [\partial_{z^\perp}(f) g - f \partial_{z^\perp}(g)]/2$. This ansatz satisfies (2.8) since,

$$\Box_x^\varepsilon \phi_x = \int \mathrm{d}\mu_z \left(\delta_{xz}^{(4)} J_z + \frac{1}{2} \delta_{z^\perp} \left[\Box_x^\varepsilon \partial_{z^\perp} \Delta_{xz}^\varepsilon \phi_z - \delta_{xz}^{(4)} \partial_{z^\perp} \phi_z \right] \right) = J_x - \delta_{x^\perp} \partial_{x^\perp} \phi_x \,, \tag{2.11}\,{}^b_{\mathcal{H}\,\mathcal{S}}$$

where, in the second step, integration by parts was carried out using asymptotic fall-off conditions. Written in this form, it is clear that the boundary term on the right-hand side acts like a source term. The field configuration on the boundary itself can only be

caused by the external source and therefore reads

$$\delta_{z^\perp}\phi_z = \delta_{z^\perp}\int \mathrm{d}\mu_y\, \Delta^\varepsilon_{zy} J_y\,. \tag{2.12}{}^{b}_{\mathcal{H}\mathcal{S}}$$

Inserting this into Eq. (2.10) yields

$$\phi_x = \int \mathrm{d}\mu_z \left(\Delta^\varepsilon_{xz} J_z + \delta_{z^\perp}\Delta^\varepsilon_{xz}\overset{\leftrightarrow}{\partial}_{z^\perp}\int \mathrm{d}\mu_y\, \Delta^\varepsilon_{zy} J_y\right) = \int \mathrm{d}\mu_y \left(\Delta^\varepsilon_{xy} + \Delta^{\mathcal{R}}_{xy}\right) J_y\,, \tag{2.13}{}^{b}_{\mathcal{H}\mathcal{S}}$$

where we have renamed the z integral of the first term to a y integral and defined the reflection propagator

$$\Delta^{\mathcal{R}}_{xy} := \int \mathrm{d}\mu_z \delta_{z^\perp}\Delta^\varepsilon_{xz}\overset{\leftrightarrow}{\partial}_{z^\perp}\Delta^\varepsilon_{zy}\,. \tag{2.14}{}^{b}_{\mathcal{H}\mathcal{S}}$$

Therefore, as a direct consequence of Huygens' principle, fixing an intermediate point of a propagator Δ, here at the boundary ($z^\perp = 0$), leads to a consecutive action of two propagators. This procedure is by no means limited to one intermediate point, but can be generalized to any number.

In the following we investigate the retarded reflection propagator in order to examine its properties. Notice, we have only used the defining equation of the propagators in Eq. (2.9). Thus, denoting the incoming momentum $\mathbf{k}$ and the reflected wave momentum $\mathbf{q}$ as shown in Fig. 2.1, the retarded reflection propagator results to be

$$\begin{aligned}{}^{\mathrm{ret}}\Delta^{\mathcal{R}}_{xy} = i\Theta_{x^t y^t}\int \frac{\mathrm{d}^3k\,\mathrm{d}q_\perp}{(2\pi)^3 8\omega^\varepsilon_k\omega^\varepsilon_q\,\varepsilon^2}\,\delta(\omega^\varepsilon_k-\omega^\varepsilon_q)\,(q_\perp-k_\perp)\\ \times\left(e^{-i(\omega^\varepsilon_q x^t-\omega^\varepsilon_k y^t)}e^{i\mathbf{k}_\parallel(\mathbf{x}^\parallel-\mathbf{y}^\parallel)}e^{i(q_\perp x^\perp-k_\perp y^\perp)}-\mathrm{h.c.}\right),\end{aligned} \tag{2.15}{}^{br}_{\mathcal{H}\mathcal{S}}$$

where the z and $q_\parallel$ integration was performed with the restriction of a large temporal difference $x^t - y^t$, which we denote with the equation superscript r. Because of this restriction, the z^t integration yielded the delta distribution enforcing energy conservation $\delta(\omega^\varepsilon_k - \omega^\varepsilon_q)$ and thus all contributions which include $\delta(\omega^\varepsilon_k + \omega^\varepsilon_q)$ were neglected. We rewrite the delta distribution with $\delta(\omega^\varepsilon_k - \omega^\varepsilon_q) = \varepsilon\omega^\varepsilon_q/|q_\perp|\,[\delta(q_\perp - k_\perp) + \delta(q_\perp + k_\perp)]$ such that the first contribution setting $k_\perp = q_\perp$ vanishes in Eq. (2.15) due to the $q_\perp - k_\perp$ part. Applying this, the retarded propagator evaluates to

$${}^{\mathrm{ret}}\Delta^{\mathcal{R}}_{xy} = i\Theta_{x^t y^t}\int \frac{\mathrm{d}^3k}{(2\pi)^3 4\omega^\varepsilon_k\varepsilon}\frac{k_\perp}{|k_\perp|}\left(e^{-i\omega^\varepsilon_k(x^t-y^t)}e^{i\mathbf{k}_\parallel(\mathbf{x}^\parallel-\mathbf{y}^\parallel)}e^{-ik_\perp(x^\perp+y^\perp)}-\mathrm{h.c.}\right). \tag{2.16}{}^{br}_{\mathcal{H}\mathcal{S}}$$

Decomposing this propagator with ${}^{\mathrm{ret}}\Delta^{\mathcal{R}}_{xy} = (G^{\mathcal{R}}_{xy} - G^{\mathcal{R}}_{yx})\Theta_{x^t y^t}$ the Wightman distribution

for the reflection propagator reads

$$G^{\mathcal{R}}_{xy} = i \int \frac{\mathrm{d}^3 k}{(2\pi)^3 4\omega_k^\varepsilon \varepsilon} \frac{k_\perp}{|k_\perp|} e^{-i\omega_k^\varepsilon (x^t - y^t)} e^{i\mathbf{k}_\parallel (\mathbf{x}^\parallel - \mathbf{y}^\parallel)} e^{-ik_\perp (x^\perp + y^\perp)} \,. \tag{2.17}$$

In order to obtain a physical understanding we compute the k integral and use approximations when needed. First we use $\int_{\mathbb{R}} \mathrm{d}x\, x/|x| f(x) = \int_0^\infty \mathrm{d}x\, [f(x) + f(-x)]$, second we take a normal incidence setup n with $\mathbf{x}^\parallel = \mathbf{y}^\parallel$ and transform to spherical coordinates

$${}^{\mathrm{ret}}\Delta^{\mathcal{R}}_{xy} = i\Theta_{x^t y^t} \int \frac{\mathrm{d}k \mathrm{d}k_\theta \mathrm{d}k_\phi}{2(2\pi)^3} k \sin(k_\theta) \Big(e^{-ik/\varepsilon (x^t - y^t)} \cos\left[k\Delta x \cos(k_\theta)\right] - \mathrm{h.c.} \Big) \,, \tag{2.18}$$

where $\Delta x = \sqrt{(\mathbf{x}^\parallel - y^\parallel)^2 + (x^\perp + y^\perp)^2}$. Performing the k_ϕ integration and the k_θ integration results in

$${}^{\mathrm{ret}}\Delta^{\mathcal{R}}_{xy} = i\Theta_{x^t y^t} \int \frac{\mathrm{d}k\, \pi}{(2\pi)^3 \Delta x} \left(e^{-ik/\varepsilon (x^t - y^t)} \sin\left(k\Delta x\right) + \mathrm{h.c.} \right) . \tag{2.19}$$

With $\int_{\mathbb{R}} \mathrm{d}x\, e^{ikx} = 2\int_0^\infty \mathrm{d}x\, \cos(kx) = 2\pi\delta(k)$ and $\int_0^\infty \mathrm{d}x\, \sin(kx) = 1/k$ we evaluate the integral to be

$${}^{\mathrm{ret}}\Delta^{\mathcal{R}}_{xy} = \frac{\Theta_{x^t y^t}}{(2\pi)^2 \Delta x} \left[\pi\delta\left(\Delta x - \frac{x^t - y^t}{\varepsilon} \right) - \pi\delta\left(-\Delta x - \frac{x^t - y^t}{\varepsilon} \right) \right] . \tag{2.20}$$

Since the difference $x^t - y^t$ is strictly positive enforced by the Heaviside step function, the delta distribution of the second term does not contribute. Thus, the final result is

$${}^{\mathrm{ret}}\Delta^{\mathcal{R}}_{xy} = \frac{\Theta_{x^t y^t}}{4\pi\Delta x} \delta\left(\Delta x - \frac{x^t - y^t}{\varepsilon} \right) . \tag{2.21}$$

Therefore, the reflected field configuration can only propagate in negative $x^\perp$ direction, that is, away from the boundary. This is the expected physical result which we could have also obtained using mirror charges and thus validating the ansatz for the field in Eq. (2.10).

As a final consistency check we act with the d'Alembert operator onto this propagator,

$$\Box^\varepsilon_x \, {}^{\mathrm{ret}}\Delta^{\mathcal{R}}_{xy} = \delta(x^t - y^t)\delta(x^\perp + y^\perp)\delta^{(2)}(\vec{x}^\parallel - \vec{y}^\parallel) = 0 \,, \tag{2.22}$$

where in the second step we used $x^\perp + y^\perp < 0$. Thus, as required, the total propagator satisfies the fundamental equation

$$\Box^\varepsilon_x \left({}^{\mathrm{ret}}\Delta^\varepsilon_{xy} + {}^{\mathrm{ret}}\Delta^{\mathcal{R}}_{xy} \right) = \delta^{(4)}_{xy} \,. \tag{2.23}$$

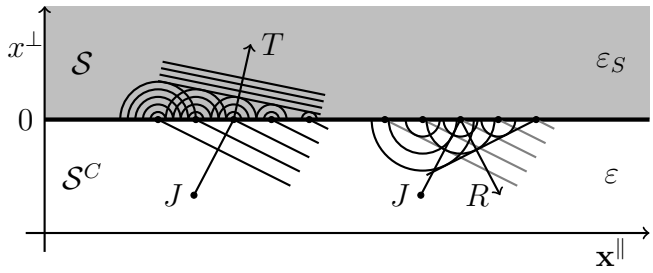

Figure 2.2.: System of two half-spaces $\mathcal{S}$ and $\mathcal{S}^C$ with susceptibilities ε_S and ε and a shared planar boundary separating them at $x^\perp = 0$. An external source J is localized in the lower half-space from which an optical ray is transmitted denoted with T and reflected denoted with R. For plane waves, the Huygens' principle is visualized to show how the angle of propagation changes upon transmission or reflection.

Having described systems with boundaries in this Section, we move on to systems with interfaces between different media in the next Section.

2.1.2. Reflection and Transmission at Interfaces

To study optical systems with interfaces, we now consider a scattering object, e.g. a sphere, with susceptibility ε_S and place it in a medium with susceptibility ε. We probe the scattering object from outside by using an external source J and thus prohibit any overlap between the scattering object and the source. With the support of the scattering object $\mathcal{S}$ the action of a real scalar field placed into this setup is given by

$$S = -\frac{1}{2}\int_{\mathcal{S}^C} \mathrm{d}\mu\, (\eta_\varepsilon^{\mu\nu}\partial_\mu\phi\partial_\nu\phi + 2\phi J) - \frac{1}{2}\int_{\mathcal{S}} \mathrm{d}\mu\, \eta_{\varepsilon_S}^{\mu\nu}\partial_\mu\phi\partial_\nu\phi\,, \qquad (2.24)\,{}^b_{\mathcal{H}\,\mathcal{S}}$$

with $\eta_{\varepsilon|\varepsilon_S} = \mathrm{diag}(-1/\varepsilon|\varepsilon_S, 1, 1, 1)$ and the complement of $\mathcal{S}$ denoted with $\mathcal{S}^C$.

For the time being, we consider a scattering object which is spread out to a whole half-space as depicted in Fig. 2.2, i.e. $\mathcal{S} = \{x \,:\, x^\perp \geq 0\}$ and $\mathcal{S}^C = \{x \,:\, x^\perp < 0\}$. Both half-spaces share a boundary at $x^\perp = 0$ and thus an interface with normal vector $n = \partial_{x^\perp}$. We choose this setup because its simplicity makes it the most suitable optical system for studying transitions at interfaces. Now we derive the reflection and transmission propagators of this system using the Huygens' principle, as sketched in Fig. 2.2.

Varying the action in the lower and upper half-space results in the following equations of motion

$$\Box^\varepsilon\phi + \delta_{x^\perp}\partial_{x^\perp}\phi = J\,, \quad \Box^{\varepsilon_S}\phi - \delta_{x^\perp}\partial_{x^\perp}\phi = 0\,, \qquad (2.25)\,{}^b_{\mathcal{H}\,\mathcal{S}}$$

where the d'Alembert operator of the respected half-space with $\Box_x^{\varepsilon|\varepsilon_S} := -\varepsilon|\varepsilon_S\,\partial_{x^t}^2 + \partial_{\mathbf{x}}^2$

was introduced. Interpreting this relation as the usual equation of motion together with a condition on the field ϕ at the interface, the propagators in the half-spaces are given by their defining equation

$$\Box_x^{\varepsilon|\varepsilon_S}\Delta_{xy}^{\varepsilon|\varepsilon_S} = \delta_{xy}^{(4)}\,. \tag{2.26}\,{}^{b}_{\mathcal{H}\mathcal{S}}$$

The external source J is located outside the scattering object, i.e. in the lower half-space $<$ as depicted in Fig. 2.2. With this setup, reflection from the lower half-space back to the lower half-space and transmission from the lower half-space to the upper half-space take place at the interface. The strength of these effects is represented by the reflection coefficient $\mathcal{R}$ and transmission coefficient $\mathcal{T}$. With this convention, we take analogous to the Wightman distribution of the reflection propagator for a boundary in (2.17) the following ansatz for the Wightman distribution in the lower half-space

$$G_{xy}^{<} = \int_k^{\varepsilon} \left[e^{ik_\perp(x^\perp - y^\perp)} - e^{-ik_\perp(x^\perp + y^\perp)}\mathcal{R}(\mathbf{k})\right]. \tag{2.27}\,{}_{\mathcal{H}\mathcal{S}}$$

Thus, in contrast to a total reflection as for boundaries in (2.17), we now allow partial reflection. This way, we can account for a non-vanishing transmission with $\mathcal{T} > 0$. A convenient ansatz for the Wightman distribution required for the transmission propagator then reads

$$G_{xy}^{>} = \int_k^{\varepsilon} e^{iq_\perp x^\perp - ik_\perp y^\perp}\,\mathcal{T}(\mathbf{k})\,, \tag{2.28}\,{}^{b}_{\mathcal{H}\mathcal{S}}$$

where $q_\perp(\mathbf{k}_\parallel, k_\perp)$ is determined as follows. Due to the different susceptibility in the upper half-space, the fields fulfill a different equation of motion as seen in (2.25). Therefore, also the Wightman distributions incorporate different dispersion relations such that $\Box_x^{\varepsilon_S} G_{xy}^{>} = 0$ and $\Box_x^{\varepsilon} G_{xy}^{\mathcal{R}} = 0$. Requiring the ansatz (2.28) to respect the dispersion relation of the upper half-space yields

$$q_\perp(\mathbf{k}) = \operatorname{sgn}(k_\perp)\sqrt{\left(\frac{\varepsilon_S}{\varepsilon} - 1\right)\mathbf{k}_\parallel^2 + \frac{\varepsilon_S}{\varepsilon}k_\perp^2}\,. \tag{2.29}\,{}^{b}_{\mathcal{H}\mathcal{S}}$$

Continuity of ϕ_x and its normal derivative $\partial_{x^\perp}\phi_x$, as required by Eq. (2.25), implies that the propagator Δ_{xy} and $\partial_{x^\perp}\Delta_{xy}$ are continuous across the interface. Therefore, the explicit boundary conditions for the Wightman distributions of the two half-spaces are

$$\lim_{x^\perp \to 0^-} G_{xy}^{<} = \lim_{x^\perp \to 0^+} G_{xy}^{>}\,, \quad \lim_{x^\perp \to 0^-} \partial_{x^\perp} G_{xy}^{<} = \lim_{x^\perp \to 0^+} \partial_{x^\perp} G_{xy}^{>}\,, \tag{2.30}\,{}^{b}_{\mathcal{H}\mathcal{S}}$$

where the limit for 0^+ is taken from the upper half-space and for 0^- from the lower

half-space. Inserting the Green functions (2.27) and (2.28), we obtain a relation for the reflection and transmission coefficient,

$$1 - \mathcal{R}(\mathbf{k}) = \mathcal{T}(\mathbf{k})\,, \qquad k_\perp + k_\perp \mathcal{R}(\mathbf{k}) = q_\perp \mathcal{T}(\mathbf{k})\,. \tag{2.31}\,{}^{b}_{\mathcal{H}\mathcal{S}}$$

Solving for these coefficients then results in

$$\mathcal{R}(\mathbf{k}) = \frac{q_\perp - k_\perp}{k_\perp + q_\perp} = \frac{\mathcal{A}-1}{\mathcal{A}+1}\,, \qquad \mathcal{T}(\mathbf{k}) = \frac{2k_\perp}{k_\perp + q_\perp} = \frac{2}{\mathcal{A}+1}\,, \tag{2.32}\,{}^{b}_{\mathcal{H}\mathcal{S}}$$

with $\mathcal{A} := [(\varepsilon_S/\varepsilon - 1)\tan^2(\alpha) + \varepsilon_S/\varepsilon]^{1/2}$ and α the angle of incidence which is defined through $\tan^2(\alpha) := \mathbf{k}_\parallel^2/k_\perp^2$.

A consistency check for this result is to investigate the charge flow of a complex scalar field across the interface. To this end, we calculate the current $j_\mu[\phi] = i\,(\phi^*\partial_\mu\phi - \partial_\mu\phi^*\phi)$ on both sides of the interface and demand continuity of the normal derivative of j across the interface. For the two half-spaces system this results in the condition

$$\lim_{x^\perp \to 0^-} \eta_\varepsilon^{\mu\nu} n_\mu j_\nu[\phi^<] = \lim_{x^\perp \to 0^+} \eta_{\varepsilon_S}^{\mu\nu} n_\mu j_\nu[\phi^>]\,. \tag{2.33}\,{}^{b}_{\mathcal{H}\mathcal{S}}$$

To illustrate that this equation is satisfied, we use the external source $J(k) \propto \delta^{(3)}(\mathbf{k} - \tilde{\mathbf{k}})$, which creates a monochromatic plane wave with spatial momentum $\tilde{\mathbf{k}}$. The resulting scalar field in the respective half-space is then given by $\phi_x^{<|>} = \int \mathrm{d}\mu_y\, \Delta_{xy}^{<|>} J_y$. Inserting these fields into Eq. (2.33) and normalizing the initial current to one, results in the following condition

$$1 = \left|\mathcal{R}(\tilde{k}_\perp)\right|^2 + \frac{\mathrm{Re}\big[q_\perp(\tilde{k}_\perp)\big]}{\tilde{k}_\perp}\left|\mathcal{T}(\tilde{k}_\perp)\right|^2\,. \tag{2.34}\,{}^{b}_{\mathcal{H}\mathcal{S}}$$

This relation is satisfied by the reflection and transmission coefficients in (2.32). Thus, the propagators in (2.27) and (2.28) account for a conserved charge flow across the interface. The first term on the right-hand side, $|\mathcal{R}|^2$, corresponds to the reflected fraction of the current, and the second term, $\mathrm{Re}(q_\perp)|\mathcal{T}|^2/k_\perp$, corresponds to the transmitted fraction. These fractions are the "reflectance" and "transmittance", respectively.

Taking into account the explicit form of the coefficients in Eq. (2.32) allows for the following phenomenological observations: First, the reflection and transmission coefficients fulfill the identity $\mathcal{R}(\bar{\omega}) + \mathcal{T}(\bar{\omega}) = 1$ and agree with the spin-averaged Fresnel equations. Second, total reflection, $|\mathcal{R}|^2 \to 1$, occurs for $\varepsilon_S/\varepsilon \to \infty$, describing a perfect mirror. Third, for $\varepsilon > \varepsilon_S$ total reflection can also be achieved for $\varepsilon_S/\varepsilon \to 0$ or $\alpha \to \pm\pi/2$. Both cases correspond to total internal reflection, which in optical experi-

ments is caused by the latter limit, as soon as the angle of incidence exceeds the critical angle $|\alpha| > |\alpha_c| = |\arctan(1/[\varepsilon/\varepsilon_S - 1])|$.

Since an infinitely sharp interface can at best be an approximation to a real interface in an experiment, we investigated in collaboration with Ka Hei Choi and Patrick Hager a smooth transition between the half-spaces [41, 42]. Even though this interface is more realistic, it shares the same reflection and transmission properties of an infinitely sharp interface if the incident wave has a wavelength which is large compared to the transition region. Therefore, if the incident field configuration cannot resolve the transition the interface can be replaced with an infinitely sharp one such that a technical more simple model can be used.

In the following Section, we use the results of the two half-space systems as a reference point for a different approach to describing propagation in this setup. This approach becomes necessary when the system is not simple enough so that we cannot solve the transition conditions in (2.30). For instance, this can be the case if the interface has a complicated time or spatial dependence, or the dispersion relation of a half-space is too complicated for the propagator of this half-space to be known.

2.2. Perturbative Approach via the Interaction Picture

In this Section, we explore an alternative approach to the one presented in the previous Section to derive the propagator in a system with two different media connected by an interface. As we will see, this approach has advantages over the previous consideration which we will exploit later on.

2.2.1. Different Dispersion Relations Encoded as Interaction

As in Sec. 2.1.2, we consider a Minkowski spacetime $(\mathcal{M}, \eta)$ with region $\mathcal{S}$ and its complement $\mathcal{S}^C$, which are characterized by the susceptibilities ε_S and ε, respectively. For convenience, we state the action (2.24) again,

$$S_0 = -\frac{1}{2}\int_{\mathcal{S}^C} \mathrm{d}\mu\, (\eta_\varepsilon^{\mu\nu}\partial_\mu\phi\partial_\nu\phi + 2\phi J) - \frac{1}{2}\int_{\mathcal{S}} \mathrm{d}\mu\, \eta_{\varepsilon_S}^{\mu\nu}\partial_\mu\phi\partial_\nu\phi =: \int_{\mathcal{S}^C} \mathrm{d}\mu\, \mathcal{L}_0^{\varepsilon} + \int_{\mathcal{S}} \mathrm{d}\mu\, \mathcal{L}_0^{\varepsilon_S}\,. \quad (2.35)\,{}^{b}_{\mathcal{H}\,\mathcal{S}}$$

The kinetic terms dictate the dispersion relation $(\omega_k^\varepsilon)^2 = \mathbf{k}^2/\varepsilon$ in $\mathcal{S}^C$ and $(\omega_k^{\varepsilon_S})^2 = \mathbf{k}^2/\varepsilon_S$ in $\mathcal{S}$. Instead of determining the propagator using matching conditions as in Sec. 2.1.2, we now adopt the following point of view. We require the field ϕ to propagate in the whole spacetime according to the first dispersion relation $(\omega_k^\varepsilon)^2 = \mathbf{k}^2/\varepsilon$, i.e. now also in the region S. This first leads to an incorrect description of the propagation within the scattering object, which is corrected by an interaction term S_I. Changing the perspective

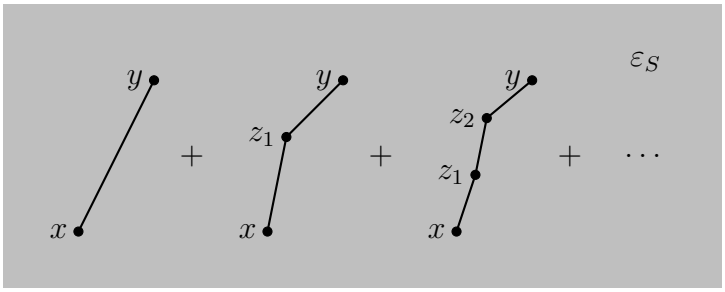

Figure 2.3.: Spatial projections of the terms in (2.38) to the propagator for a spacetime filled with a medium of susceptibility ε_S. Fundamentally, the fields propagate according to the dispersion relation with susceptibility ε and therefore interacting at every point. This means, z_1, z_2 and all subsequent z_i are integrated over the whole spacetime.

does not alter the theory at hand and thus we only regroup the action (2.35) with

$$S_0 = \int_{\mathcal{M}} \mathrm{d}\mu \; \mathcal{L}_0^{\varepsilon} - \frac{1}{2}\int_{\mathcal{S}} \mathrm{d}\mu \left[\eta_{\varepsilon_S}^{\mu\nu}\partial_\mu\phi\partial_\nu\phi - \eta_{\varepsilon}^{\mu\nu}\partial_\mu\phi\partial_\nu\phi\right] =: \int_{\mathcal{M}} \mathrm{d}\mu\, \mathcal{L}_0^{\varepsilon} + \int_{\mathcal{S}} \mathrm{d}\mu\, \mathcal{L}_I\,. \qquad (2.36)\,{}^{b}_{\mathcal{H}\,\mathcal{S}}$$

In this perspective, the "free" field ϕ evolves by means of the propagator Δ^{ε} in (2.5), i.e. as if the whole spacetime is filled with a uniform medium with susceptibility ε. In the rest state of the medium, the dispersion relation of the scattering object is then encoded through the Lagrangian $\mathcal{L}_I = \lambda_S \left(\partial_t\phi\right)^2/2$ and the coupling constant $\lambda_S = \varepsilon_S - \varepsilon$. Utilizing the interaction picture of quantum field theory, the non-perturbative propagator of the whole system is then

$$\Delta_{xy} = i\left\langle \mathrm{T}\,\phi_x\phi_y\,\exp\left\{i\int_{\mathcal{S}}\mathrm{d}\mu\,\mathcal{L}_I\right\}\right\rangle_{\mathrm{con}}, \qquad (2.37)\,{}^{b}_{\mathcal{H}\,\mathcal{S}}$$

where $\langle\cdot\rangle_{\mathrm{con}}$ includes only connected diagrams and we omit to explicitly write down the $i\epsilon$ prescription $\lim_{T_z\to\infty(1+\epsilon)}\int_{-T_z}^{T_z}\mathrm{d}z^t$.

Note that describing the dispersion relation in $\mathcal{S}^C$ as "free" and the one in the scattering object $\mathcal{S}$ as an interaction was a specific choice. We can equally consider the "free" propagation with respect to the region $\mathcal{S}$ and the action of the medium in $\mathcal{S}^C$ in terms of an interaction term. In this case, Δ^{ε_S} would be the propagator of the free field and $\varepsilon - \varepsilon_S$ would be the coupling constant. For the non-perturbative evaluation of (2.37) it is irrelevant which choice we make. However, if we wish to consider (2.37) at finite order in in the coupling constant, the choice is crucial.

To demonstrate this, we first consider a scattering object which covers the whole spacetime. This means, we take a system with the susceptibility ε_S, but describe fields that obey a dispersion relation based on ε. Therefore, the fields interact at any point in spacetime since now the interaction part of (2.36) is important everywhere. Including all these interactions, we obtain the full Green function according to (2.37):

$$\begin{aligned}\Delta_{xy} &= \Delta^{\varepsilon}_{xy} + \lambda_S \int_{\mathcal{M}} \mathrm{d}\mu_{z_1}\, \partial_{z_1^t} \Delta^{\varepsilon}_{xz_1} \partial_{z_1^t} \Delta^{\varepsilon}_{z_1 y} + \lambda_S^2 \int_{\mathcal{M}} \mathrm{d}\mu_{z_1} d\mu_{z_2}\, \partial_{z_1^t} \Delta^{\varepsilon}_{xz_1} \partial_{z_1^t} \partial_{z_2^t} \Delta^{\varepsilon}_{z_1 z_2} \partial_{z_2^t} \Delta^{\varepsilon}_{z_1 y} + \cdots \\ &= -\int \mathrm{d}^4 k\, \frac{e^{ik(x-y)}}{\eta^{\mu\nu}_{\varepsilon} k_\mu k_\nu} \left(1 - \frac{\eta^{\mu\nu}_{\varepsilon_S} k_\mu k_\nu - \eta^{\mu\nu}_{\varepsilon} k_\mu k_\nu}{\eta^{\mu\nu}_{\varepsilon} k_\mu k_\nu} + \left(\frac{\eta^{\mu\nu}_{\varepsilon_S} k_\mu k_\nu - \eta^{\mu\nu}_{\varepsilon} k_\mu k_\nu}{\eta^{\mu\nu}_{\varepsilon} k_\mu k_\nu} \right)^2 + \cdots \right) \\ &= -\int \mathrm{d}^4 k\, \frac{e^{ik(x-y)}}{\eta^{\mu\nu}_{\varepsilon_S} k_\mu k_\nu} = \Delta^{\varepsilon_S}_{xy}\,, \end{aligned} \tag{2.38}{}^{b}_{\mathcal{H}\mathcal{S}}$$

where we used the geometric series from the second to the third row and did not provide the $i\epsilon$ prescription of the propagators. The first three terms which are explicitly written here are depicted in Fig. 2.3. The resummed result is indeed the propagator Δ^{ε_S} which relies on the correct dispersion relation. In the very same way a massive propagator can be obtained from the resummation of the mass term $m^2\phi^2$ "interactions" as shown in the App. C. However, if one truncates the sum in (2.38) at a finite order in λ_S, one does not obtain Δ^{ε_S}. For a sufficiently small λ_S, a perturbative evaluation of (2.37) up to some order is nevertheless a viable approach which brakes down at latest when $|\lambda_S| \geq 1$.

If, on the other hand, one uses the susceptibility ε_S for the dispersion relation of the fields ϕ, then there is no interaction such that the integral in (2.37) has no support and vanishes. Thus one obtains Δ^{ε_S} in leading order no matter how many orders in λ_S are taken into account. For this example, choosing the dispersion relation which respects ε_S is therefore preferable. For each application we deal with in this thesis, we will investigate the best choice and discuss alternatives.

2.2.2. Connection of the Perturbative and the Non-Perturbative Approach

To demonstrate the connection between the perturbative and the non-perturbative approach we show their equivalent result for the system analyzed in Sec. 2.1.2. This means, we consider an interface separating two half-spaces with different media. However, this time we use the perturbative approach instead of the non-perturbative one. Again, the scattering object has susceptibility ε_S and covers the upper half-space $>$ with domain $\mathcal{S} = \{x \ : \ x^\perp \geq 0\}$. We place an external source in the lower half-space $<$ with domain $\mathcal{S}^C = \{x \ : \ x^\perp < 0\}$ and susceptibility ε.

We choose similar susceptibilities $\varepsilon \approx \varepsilon_S$ such that we can treat λ_S as a smallness parameter which allows us to expand (2.37) and take finite orders in λ_S into account. We thus compute the propagator perturbatively, which we indicate with the symbol p. Up to the second order in λ_S, the propagator (2.37) for the two half-spaces is then computed

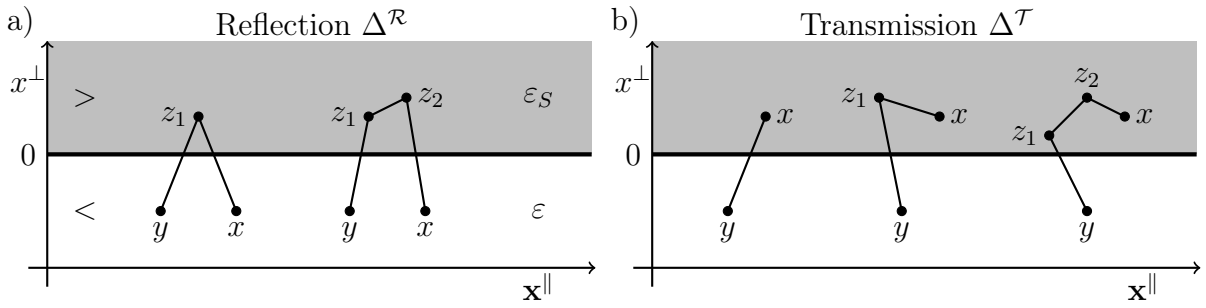

Figure 2.4.: Spatial projections of the contributions in (2.39) to the reflection propagator $\Delta^{\mathcal{R}}$ in a) and to the transmission propagator $\Delta^{\mathcal{T}}$ in b) for the system consisting of two media with different susceptibilities.

with

$$\Delta_{xy} = \Delta^{\varepsilon}_{xy} + \lambda_S \int_{\mathcal{S}} \mathrm{d}\mu_{z_1}\, \partial_{z_1^t} \Delta^{\varepsilon}_{xz_1} \partial_{z_1^t} \Delta^{\varepsilon}_{z_1 y} + \lambda_S^2 \int_{\mathcal{S}} \mathrm{d}\mu_{z_1} d\mu_{z_2}\, \partial_{z_1^t} \Delta^{\varepsilon}_{xz_1} \partial_{z_1^t} \partial_{z_2^t} \Delta^{\varepsilon}_{z_1 z_2} \partial_{z_2^t} \Delta^{\varepsilon}_{z_1 y}\,. \tag{2.39}$$

The leading order contribution $\Delta^{(0)}_{xy} = \Delta^{\varepsilon}_{xy}$ corresponds to free propagation as if there were no scattering object. The subsequent contributions interact with the scattering object once and twice, respectively. These interactions are shown in Fig. 2.4 with points z_1 and z_2 and contribute to reflection and transmission. In the following, we first calculate the linear order $\Delta^{(1)}_{xy}$ and subsequently use it to determine the quadratic order $\Delta^{(2)}_{xy}$.

Linear Order The diagram representing the term $\Delta^{(1)}_{xy}$ linear in λ_S is depicted in Fig. 2.4 with a single interaction vertex at z_1 for reflection and transmission respectively. By substituting the Feynman propagators and taking $z = z_1$ we get

$$\Delta^{(1)}_{xy} = \lambda_S \int_{\mathcal{S}} \mathrm{d}\mu_z \int \frac{\mathrm{d}^4k}{(2\pi)^4} \frac{\mathrm{d}^4q}{(2\pi)^4} \frac{k_0 q_0\, e^{iq(x-z)} e^{ik(z-y)}}{(\eta^{\mu\nu}_{\varepsilon} q_\mu q_\nu - i\epsilon)(\eta^{\mu\nu}_{\varepsilon} k_\mu k_\nu - i\epsilon)}\,, \tag{2.40}$$

where we introduced the $i\epsilon$ prescription. As usual, the limit $\epsilon \to 0$ outside the momentum integrals is understood. The z^t and $\mathbf{z}^\parallel$ integration yield delta distributions, which in turn simplify the corresponding q_0 and $\mathbf{q}_\parallel$ integration,

$$\Delta^{(1)}_{xy} = \lambda_S \int_0^\infty \mathrm{d}z^\perp \int \frac{\mathrm{d}^4k}{(2\pi)^4} \frac{\mathrm{d}q_\perp}{2\pi} k_0^2\, \frac{e^{i\mathbf{k}_\parallel(\mathbf{x}^\parallel - \mathbf{y}^\parallel)} e^{-ik_0(x^t - y^t)} e^{-iz^\perp(q_\perp - k_\perp)} e^{iq_\perp x^\perp - ik_\perp y^\perp}}{(-\varepsilon k_0^2 + \mathbf{k}_\parallel^2 + q_\perp^2 - i\epsilon)(-\varepsilon k_0^2 + \mathbf{k}_\parallel^2 + k_\perp^2 - i\epsilon)}\,. \tag{2.41}$$

Eq. (2.41) contains a total of four poles in the complex k_0 plane as depicted in Fig. 2.5a). For simplicity, we first fix the causal order as $x^t > y^t$, indicated with c, and restore the other case later. With this restriction, only the two poles in the lower half-plane contribute

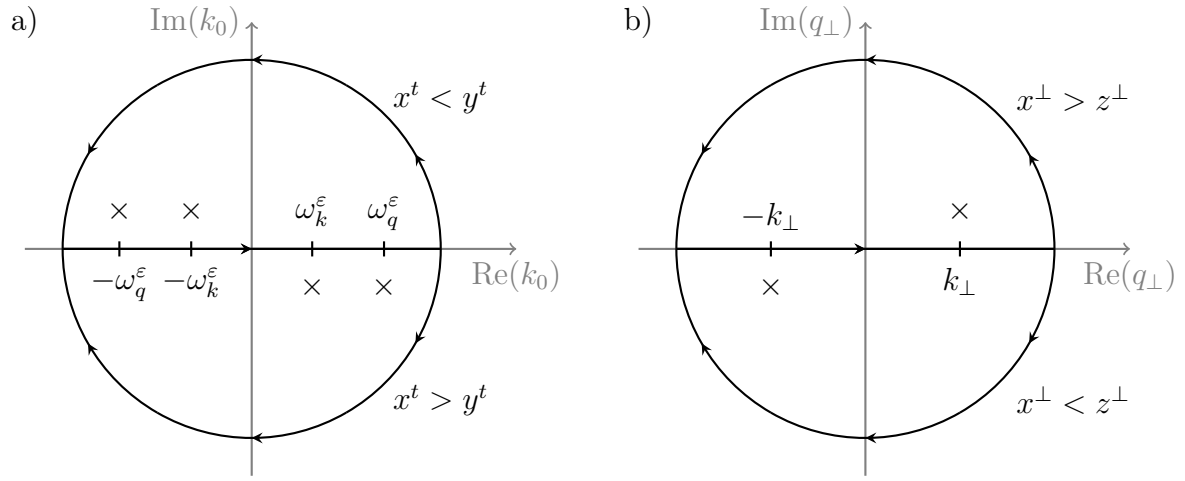

Figure 2.5.: Complex plane of the k_0 integral in Eq. (2.41) depending on the causal order of x^t and y^t depicted in a). Complex plane of the $q_\perp$ integral belonging to the first term in Eq. (2.43) shown in b) for the reflection contribution ($x^\perp < z^\perp$) and the transmission contribution ($x^\perp > z^\perp$).

as shown in Fig. 2.5a),

$$\Delta_{xy}^{(1)} = i\lambda_S \int_0^\infty \mathrm{d}z^\perp \int \frac{\mathrm{d}^3k}{(2\pi)^3}\frac{\mathrm{d}q_\perp}{2\pi} e^{i\mathbf{k}_\parallel(\mathbf{x}^\parallel-\mathbf{y}^\parallel)} e^{iq_\perp(x^\perp-z^\perp)} e^{ik_\perp(z^\perp-y^\perp)} \times \frac{\omega_k^\varepsilon e^{-i\omega_k^\varepsilon(x^t-y^t)} - \omega_q^\varepsilon e^{-i\omega_q^\varepsilon(x^t-y^t)}}{2\varepsilon(k_\perp-q_\perp)(k_\perp+q_\perp)}\,, \tag{2.42}$$

where again $(\omega_q^\varepsilon)^2 = (\mathbf{k}_\parallel^2 + q_\perp^2)/\varepsilon$. For the denominators, we apply the Sokhotski-Plemelj theorem, $\mathcal{P}\,[1/(k_\perp \pm q_\perp)] = 1/(k_\perp \pm q_\perp + i\epsilon) + i\pi\delta(k_\perp \pm q_\perp)$ with the Cauchy principal value $\mathcal{P}$. Because of the minus sign in the numerator in Eq. (2.42), the contributions of the delta distributions $\delta(k_\perp \pm q_\perp)$ cancel each other out. This leads to

$$\Delta_{xy}^{(1)} = i\lambda_S \int_0^\infty \mathrm{d}z^\perp \int \frac{\mathrm{d}^3k}{(2\pi)^3}\frac{\mathrm{d}q_\perp}{2\pi} e^{i\mathbf{k}_\parallel(\mathbf{x}^\parallel-\mathbf{y}^\parallel)} e^{iq_\perp(x^\perp-z^\perp)} e^{ik_\perp(z^\perp-y^\perp)} \times \frac{\omega_k^\varepsilon e^{-i\omega_k^\varepsilon(x^t-y^t)} - \omega_q^\varepsilon e^{-i\omega_q^\varepsilon(x^t-y^t)}}{2\varepsilon(k_\perp-q_\perp+i\epsilon)(k_\perp+q_\perp+i\epsilon)}\,. \tag{2.43}$$

The second term, proportional to ω_q^ε, carries the poles $k_\perp = q_\perp - i\epsilon$ and $k_\perp = -q_\perp - i\epsilon$ in the lower complex $k_\perp$ half-plane. This term vanishes identically since $z^\perp > 0 > y^\perp$. The first term, however, yields a non-vanishing contribution regardless of whether we close the $q_\perp$ integration contour in the lower (for $x^\perp < z^\perp$) or upper half-plane (for $x^\perp > z^\perp$) as demonstrated in Fig. 2.5b). Thus the propagator becomes

$$\Delta_{xy}^{(1)} = i\lambda_S \int_0^\infty \mathrm{d}z^\perp \int_k^\varepsilon \frac{(\omega_k^\varepsilon)^2}{2\,(k_\perp+i\epsilon)} \Big[\Theta_{x^\perp z^\perp} e^{ik_\perp(x^\perp-y^\perp)} - \Theta_{z^\perp x^\perp} e^{-ik_\perp(x^\perp+y^\perp)+2iz^\perp(k_\perp+i\epsilon)}\Big]\,. \tag{2.44}$$

Performing the $z^\perp$ integration over the support of the scattering object, i.e., the upper half-space, we obtain

$$\Delta^{(1)}_{xy} = -\int_k^\varepsilon \frac{\bar\omega}{4}\Big[\Theta_{x^\perp} e^{ik_\perp(x^\perp - y^\perp)}\left(1 - 2ix^\perp k_\perp\right) + \Theta_{-x^\perp} e^{-ik_\perp(x^\perp + y^\perp)}\Big]\,, \tag{2.45}$$

where we introduced a rescaled expansion parameter $\bar\omega = \lambda_S(\omega^\varepsilon_k)^2/k_\perp^2 = \lambda_S[1+\tan^2(\alpha)]/\varepsilon$ with the angle of incidence α. This propagator is valid for $y^\perp < 0$ and $x^t > y^t$ such that the Wightman distribution equals the propagator $G_{xy} := \Delta_{xy}|_{x^t > y^t}$. As before we group the contribution to the Wightman distribution into the three terms of direct propagation, reflection and transmission,

$$G_{xy} = (1 - \Theta_{x^\perp})\left(G^\varepsilon_{xy} + G^{\mathcal{R}}_{xy}\right) + \Theta_{x^\perp} G^{\mathcal{T}}_{xy}\,. \tag{2.46}$$

With this definition, the reflection propagator up to linear order in λ_S, depicted as the first diagram in Fig. 2.4a) reads

$$G^{\mathcal{R}}_{xy} = -\int_k^\varepsilon e^{ik_\perp(x^\perp + y^\perp)}\mathcal{R}(\bar\omega)\,, \tag{2.47}$$

with reflection coefficient

$$\mathcal{R}(\bar\omega) = \frac{1}{4}\bar\omega + \mathcal{O}\left(\bar\omega^2\right). \tag{2.48}$$

The corresponding transmission propagator, as represented by the first two diagrams in Fig. 2.4b), is given by

$$G^{\mathcal{T}}_{xy} = \int_k^\varepsilon e^{ik_\perp(x^\perp - y^\perp)}\left(1 + \frac{i}{2}\bar\omega k_\perp x^\perp\right)\mathcal{T}(\bar\omega) + \mathcal{O}\left(\bar\omega^2\right), \tag{2.49}$$

where the $x^\perp$ independent factors are combined in the transmission coefficient,

$$\mathcal{T}(\bar\omega) = 1 - \frac{1}{4}\bar\omega + \mathcal{O}\left(\bar\omega^2\right) = 1 - \mathcal{R}(\bar\omega)\,. \tag{2.50}$$

The contributions which depend on $x^\perp$ such as the one in (2.49) modify the exponential and thus yield terms of every order in $k_\perp x^\perp$. Next, we compute the reflection and transmission propagator to quadratic order in λ_S.

Quadratic Order Having examined the first order term $\Delta^{(1)}_{xy}$, we can now evaluate the second order term $\Delta^{(2)}_{xy}$ in (2.39). To simplify the computation we perform it as similar as possible to the previous calculation of the linear order term $\Delta^{(1)}_{xy}$. To achieve this,

we express the linear transmission propagator $\Delta_{xy}^{\mathcal{T}(1)} := \Delta_{xy}^{(1)}|_{x^\perp>0}$ as a four-momentum integral,

$$\Delta_{xy}^{\mathcal{T}(1)} = \int \frac{\mathrm{d}^4k}{(2\pi)^4} \frac{e^{ik(x-y)}}{\eta^\varepsilon(k,k) - i\epsilon} X(k_0, k_\perp, x^\perp) \,, \tag{2.51}$$

with

$$X(k_0, k_\perp, x^\perp) := -\lambda_S \frac{k_0^2}{2\,(k_\perp + i\epsilon)} \left(\frac{1}{2(k_\perp + i\epsilon)} - ix^\perp \right) . \tag{2.52}$$

For $x^t > y^t$ we obtain the expression (2.45) through the k_0 integration. In addition, there is a contribution for $x^t < y^t$, which we have to include for the calculation of the second order as argued in App. C. Since we have rewritten the transmission propagator as a four-moment integral, we can now morally re-run the calculation of the linear order with a modified propagator and thus analogously iteratively solve for higher orders. Since $z_1^\perp > 0$, we can rewrite the second-order contribution in (2.39) using the transmission propagator (2.51), so that

$$\Delta_{xy}^{(2)} = \lambda_S \int_{\mathcal{S}} \mathrm{d}\mu_z \, \partial_{z^t} \Delta_{xz}^{\varepsilon} \partial_{z^t} \Delta_{zy}^{\mathcal{T}(1)} \,. \tag{2.53}$$

Here, and in general for every propagator $\Delta_{xy}^{(n)}$ of order λ_S^n, we take the transmission propagator $\Delta_{zy}^{\mathcal{T}(n-1)}$ to describe the propagation from the lower half-space to the upper half-space and add one propagator $\Delta_{xz}^{\varepsilon}$ which then determines whether it is a contribution for the transmission propagator $\Delta_{xy}^{\mathcal{T}(n)}$ or the reflection propagator $\Delta_{xy}^{\mathcal{R}(n)}$ depending on the choice of $x^\perp$.

Eq. (2.53) is similar to that for $\Delta_{xy}^{(1)}$, which makes it convenient to again assume the causal order $x^t > y^t$ and perform the steps (2.41) and (2.42) analogously. This yields a higher order version of (2.43),

$$\begin{aligned} \Delta_{xy}^{(2)} = i\lambda_S \int_0^\infty dz^\perp \int \frac{\mathrm{d}^3k}{(2\pi)^3} \frac{\mathrm{d}q_\perp}{2\pi} e^{i\mathbf{k}_\parallel(\mathbf{x}^\parallel - \mathbf{y}^\parallel)} e^{iq_\perp(x^\perp - z^\perp)} e^{ik_\perp(z^\perp - y^\perp)} \\ \times \frac{\omega_k^\varepsilon e^{-i\omega_k^\varepsilon(x^0-y^0)} X(\omega_k^\varepsilon, k_\perp, z^\perp) - (\omega_k^\varepsilon \to \omega_q^\varepsilon)}{2\varepsilon(k_\perp - q_\perp + i\epsilon)(k_\perp + q_\perp + i\epsilon)} \,. \end{aligned} \tag{2.54}$$

The second term proportional to ω_q^ε has three poles in the lower complex $k_\perp$ half-plane. As depicted in Fig. 2.6a), these are irrelevant because the integration contour is closed in the upper half-plane, since $z^\perp > y^\perp$. In contrast, the first term, which is proportional to ω_k^ε, has the pole structure shown in Fig. 2.6b), which leads to the expression

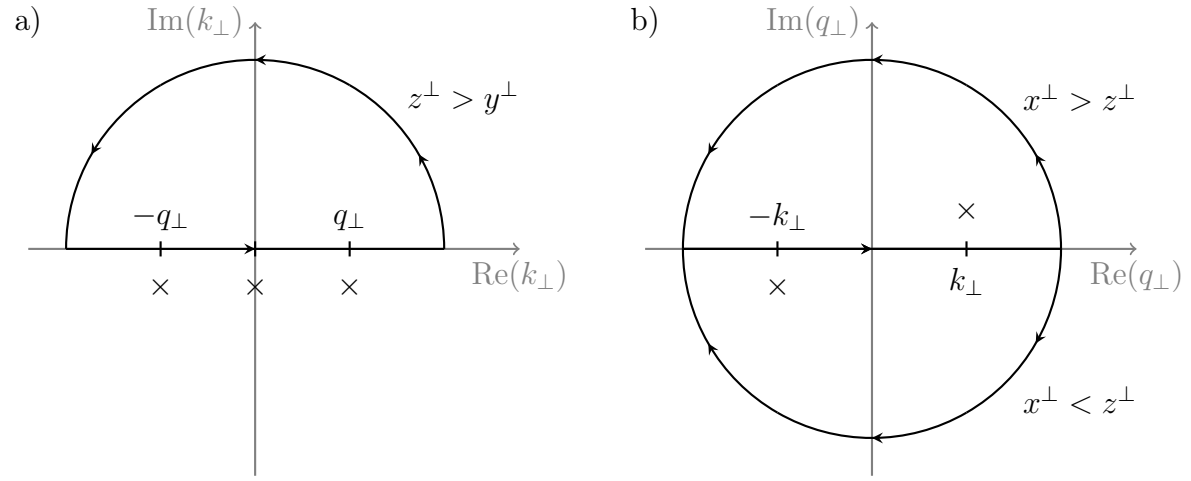

Figure 2.6.: Complex plane of the $k_\perp$ integral belonging to the second term in Eq. (2.54) expressed in a) and for the reflection contribution ($x^\perp < z^\perp$) and the transmission contribution ($x^\perp > z^\perp$) of the $q_\perp$ integral of the first term in Eq. (2.54) shown in b).

$$\Delta^{(2)}_{xy} = i\lambda_S \int_0^\infty \mathrm{d}z^\perp \int_k^\varepsilon \frac{(\omega_k^\varepsilon)^2 X(\omega_k^\varepsilon, k_\perp, z^\perp)}{2\,(k_\perp + i\epsilon)} \times \left[\Theta_{x^\perp z^\perp} e^{ik_\perp(x^\perp - y^\perp)} - \Theta_{z^\perp x^\perp} e^{-ik_\perp(x^\perp + y^\perp) + 2iz^\perp(k_\perp + i\epsilon)}\right]. \tag{2.55}{}^{bpc}_{\mathcal{HS}}$$

Performing the $z^\perp$ integration and splitting the terms proportional to $\Theta_{x^\perp}$ and $\Theta_{-x^\perp}$, we obtain

$$\Delta^{(2)}_{xy} = \int_k^\varepsilon \frac{\bar{\omega}^2}{8}\left[\Theta_{x^\perp} e^{ik_\perp(x^\perp - y^\perp)}\left(1 - 2ik_\perp x^\perp - \left(k_\perp x^\perp\right)^2\right) + \Theta_{-x^\perp} e^{-ik_\perp(x^\perp + y^\perp)}\right]. \tag{2.56}{}^{bpc}_{\mathcal{HS}}$$

As previously outlined, higher orders could now be calculated iteratively by using the transmission part from (2.56) as input for the subsequent order.

Thus, combining the leading order in (2.47) with (2.56) the reflection coefficient up to second order in λ_S as depicted in Fig. 2.4a) results in

$$\mathcal{R}(\bar{\omega}) = \frac{1}{4}\bar{\omega} - \frac{1}{8}\bar{\omega}^2 + \mathcal{O}\left(\bar{\omega}^3\right) . \tag{2.57}{}^{bp}_{\mathcal{HS}}$$

The transmission Wightman distribution, including all diagrams in Fig. 2.4b), is given by

$$G^{\mathcal{T}}_{xy} = \int_k^\varepsilon e^{ik_\perp(x^\perp - y^\perp)}\left(1 + \frac{i}{2}\left(\bar{\omega} - \frac{\bar{\omega}^2}{4}\right)k_\perp x^\perp - \frac{1}{8}\left(\bar{\omega}\, k_\perp x^\perp\right)^2\right)\mathcal{T}(\bar{\omega}) + \mathcal{O}\left(\bar{\omega}^3\right) , \tag{2.58}{}^{bp}_{\mathcal{HS}}$$

with transmission coefficient

$$\mathcal{T}(\bar{\omega}) = 1 - \frac{1}{4}\bar{\omega} + \frac{1}{8}\bar{\omega}^2 + \mathcal{O}\left(\bar{\omega}^3\right) = 1 - \mathcal{R}(\bar{\omega})\,. \tag{2.59}\,{}^{bp}_{\mathcal{H}\mathcal{S}}$$

We note that the propagation across the interface terminates within the scattering object. Therefore, the transmission propagator encodes the dispersion relation inherited from $\mathcal{S}$ such that $\Box_x^{\varepsilon S} G^{\mathcal{T}}_{xy} = 0$, in contrast to the reflection with $\Box_x^{\varepsilon} G^{\mathcal{R}}_{xy} = 0$. As for the example with the scattering object covering the entire spacetime, the interaction exponential in (2.37) provides the correct dispersion relation. This is reflected in terms entering with powers of $k_\perp x^\perp$ in (2.58), and by a partial resummation the transmission propagator becomes

$$G^{\mathcal{T}}_{xy} = \int_k^{\varepsilon} e^{iq_\perp x^\perp - ik_\perp y^\perp} \mathcal{T}(\bar{\omega})\,, \tag{2.60}\,{}^{bp}_{\mathcal{H}\mathcal{S}}$$

where we used $q_\perp$ as introduced in (2.29). Replacing $k_\perp$ by $q_\perp$, the dispersion relation of $\mathcal{S}$ is now indeed encoded in the upper half-plane. For a perturbative analysis where the $\bar{\omega}$ expansion is truncated, $\bar{\omega}$ must be small, i.e. $\lambda_S/\varepsilon \ll 1$ and $\tan^2(\alpha) \ll 1$. In this setting, only systems with $\mathcal{T} \approx 1$ and $\mathcal{R} \ll 1$ can be described consistently. For scenarios in which total internal reflection may occur, a closed-form expression of this series is needed that takes into account all orders of λ_S. Due to the simplicity of the interface, we can presume all higher order contributions as in the example of the scattering object covering the whole spacetime. Considering all terms of the series, the transmission coefficient reads,

$$\mathcal{T}(\bar{\omega}) = \sum_{n=0}^{\infty} \frac{\sqrt{\pi}}{\Gamma(2+n)\Gamma(\frac{1}{2}-n)} \bar{\omega}^n = \frac{2}{1+\sqrt{1+\bar{\omega}}} = 1 - \mathcal{R}(\bar{\omega})\,, \tag{2.61}\,{}^{b}_{\mathcal{H}\mathcal{S}}$$

with the gamma function Γ. These transmission and reflection coefficients agree with the result in (2.32) obtained by matching techniques with $\mathcal{A} = \sqrt{1+\bar{\omega}}$.

For the system of two half-spaces, both the perturbative and non-perturbative approaches can be used. For any other system, it is necessary to check which technique is more suitable. The perturbative approach is preferred when the dispersion relation for the scattering object or for the surrounding spacetime is so complicated that the propagator is unknown. Furthermore, if the scattering object has a complicated geometry or time dependence, the perturbative approach only requires solving a more sophisticated integral in the interaction exponential (2.37). For the non-perturbative approach, this would mean solving complicated transition conditions. On the other hand, if a system allows total reflection, the perturbative approach requires resummation that may not be feasible, such that in this case the non-perturbative approach is preferred. We will discuss

which approach to use in the subsequent systems in the context of field theory in curved spacetimes. As we will see, in this context we will face the difficulty that we require the propagator in a complicated background geometry such that we have to use the non-perturbative technique. In the next Chapter, we demonstrate how to solve this dilemma by exploiting the principle of equivalence.

3. Propagation During Black-Hole Formation

Solving the propagator's defining equation for a given spacetime can be arbitrarily difficult. If the propagator is only required in a local environment, the principle of equivalence can be used to obtain it straightforwardly for any spacetime [30]. According to the principle of equivalence, the gravitational mass equals the inertial mass. Therefore, an observer cannot distinguish between being accelerated and being subjected to a homogeneous gravitational field [43]. This means that in a small environment where the gravitational field is sufficiently homogeneous, the metric for an arbitrarily curved background is flat when expressed using coordinates in which a free-falling observer is at rest. For environments that are larger, such that the Minkowski metric is insufficient, the inhomogeneity of the gravitational field can be taken into account with correction terms. A particular coordinate manifestation of this procedure are the Riemann normal coordinates (RNC) and the Fermi normal coordinates (FNC), which we introduce in the next Section.

In Sec. 3.2, we begin by constructing and analyzing the geometry of thin matter shells with different trajectories, as described in our article [12] in collaboration with Florian Niedermann. Using a normal neighborhood, we derive the propagator of a scalar field in Sec. 3.3 perturbatively and non-perturbatively in a fixed shell background. We then examine these propagators to see whether a communication experiment across the shell fails once the shell radius is smaller than the gravitational radius in Sec. 3.3.3.

3.1. Normal Coordinates

In the following Sections, we will concentrate on RNC before delving into alternative normal coordinates in Section 3.1.5. To construct RNC around an anchor point in a given background metric g for an observer with coordinate velocity v^a, we proceed as follows: We compute locally the vierbein e^a_μ which satisfies the conditions $e^a_0 = v^a$ and $g_{ab}e^a_\alpha e^b_\beta = \eta_{\alpha\beta}$, i.e. transforming the metric into the Minkowski metric at the anchor point. Using this vierbein, the inverse RNC metric up to the fourth adiabatic order, i.e. including terms $\mathcal{O}(x^4)$ in the standard coordinates $x^\alpha = (x^0, x^1, x^2, x^3)$ reads [44, 45]

$$g^{\mu\nu}(x) = \eta^{\mu\nu} + \frac{1}{3}R_{\alpha}{}^{\mu\nu}{}_{\beta}x^{\alpha}x^{\beta} + \frac{1}{6}R_{\alpha}{}^{\mu\nu}{}_{\gamma,\beta}x^{\alpha}x^{\beta}x^{\gamma} + \left(\frac{1}{15}R^{\mu}_{\alpha\beta\lambda}R^{\nu}{}_{\gamma\delta}{}^{\lambda} + \frac{1}{20}R^{\mu}{}_{\alpha}{}^{\nu}{}_{\beta,\gamma\delta}\right)x^{\alpha}x^{\beta}x^{\gamma}x^{\delta} + \mathcal{O}\left(x^5\right), \tag{3.1}\,{}^{a}_{\mathcal{G}}$$

with the Riemann tensor $R^{\mu}_{\nu\alpha\beta} = \Gamma^{\mu}_{\nu\beta,\alpha} - \Gamma^{\mu}_{\nu\alpha,\beta} + \Gamma^{\lambda}_{\nu\beta}\Gamma^{\mu}_{\alpha\lambda} - \Gamma^{\lambda}_{\nu\alpha}\Gamma^{\mu}_{\beta\lambda}$ and its derivatives evaluated at the origin $x^{\alpha} = 0$. Taking only finite orders of the expansion into account as in (3.1) can usually only approximate a curved background in a neighborhood and thus we indicate this approximation with the symbol a. In the next Section, we derive the propagator of a scalar field in such a neighborhood using a novel approach based on the technique we presented in Sec. 2.2.

3.1.1. Propagation in RNC via the Perturbative Approach

To obtain the propagator1 in RNC we start with the action of a free massless scalar field minimally coupled to a gravitational background with the metric g,

$$S = -\frac{1}{2}\int \mathrm{d}^4x\ \sqrt{-g}\, g^{\mu\nu}\partial_{\mu}\phi\partial_{\nu}\phi\,, \tag{3.2}\,{}^{b}_{\mathcal{H}\,\mathcal{G}}$$

where we adopt the notation $\det(g) =: g$ for this Chapter. Placing the field into a RNC patch one can for a given adiabatic order find the propagator by iteratively solving the defining equation of the propagator [30]. This is a delicate procedure that relies on tedious calculations and special properties of RNC. Since this is a perturbative problem, we instead apply the perturbative approach from Sec. 2.2 to find the RNC propagator and compare our results with [30].

This perturbative approach requires to choose the kinetic part of the action according to which the fields should propagate freely. For the action (3.2), there are among others the following candidates for the kinetic Lagrangian: $\mathcal{L}_k \in \{-Z^{\mu\nu}\partial_{\mu}\phi\partial_{\nu}\phi/2, Z^{\mu\nu}\phi\partial_{\mu}\partial_{\nu}\phi/2\}$ with $Z^{\mu\nu} \in \{\sqrt{-g}\, g^{\mu\nu}, g^{\mu\nu}, \eta^{\mu\nu}\}$. The second class of kinetic terms are relevant if one partial integrates (3.2) leading to an interaction term which is proportional to $\Gamma^{\mu\nu}_{\mu}\partial_{\nu}\phi$. This can prove to be in particular useful if one wants to compute observables of for example bi-local operators by connecting both points of the operator with a Wilson line, i.e. a path ordered exponential of $\Gamma^{\mu\nu}_{\mu}$ [17].

Since the leading order term of the RNC propagator in [30] is the Minkowski propagator we conveniently choose the Minkowski action as the free part $\mathcal{L}_k = -\eta^{\mu\nu}\partial_{\mu}\phi\partial_{\nu}\phi/2$. Then, splitting (3.2) into this free part and the remaining part, which is now an interaction part, reads

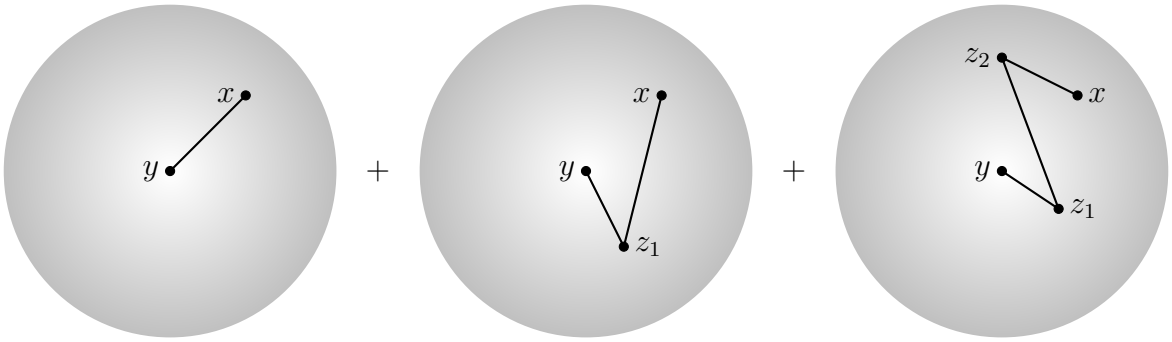

Figure 3.1.: Spatial projection into a plane of the first three contributions to the propagator Δ_{xy} in a RNC patch with the origin at y. The fields propagate with respect to a dispersion relation respected in the leading order Minkowski spacetime and thus interact with the difference added by higher order contributions at every spacetime point except the origin. Therefore, z_1 and z_2 are integrated over the whole RNC patch. The difference between the background and the Minkowski term, i.e. the strength of the interaction, is exemplary indicated by the shading of the gray color.

$$\begin{aligned} S &= -\frac{1}{2}\int \mathrm{d}^4x\ \sqrt{-g}\, g^{\mu\nu}\partial_\mu\phi\partial_\nu\phi = -\frac{1}{2}\int \mathrm{d}\mu\, \left(\eta^{\mu\nu} + \sqrt{-g}\, h^{\mu\nu} + (\sqrt{-g}-1)\eta^{\mu\nu}\right)\partial_\mu\phi\partial_\nu\phi \\ &= -\frac{1}{2}\int \mathrm{d}\mu\ \eta^{\mu\nu}\partial_\mu\phi\partial_\nu\phi - \frac{1}{2}\int \mathrm{d}\mu\ \tilde{h}^{\mu\nu}\partial_\mu\phi\partial_\nu\phi =: \int \mathrm{d}\mu\ \mathcal{L}_k + \int \mathrm{d}\mu\ \mathcal{L}_I\ , \end{aligned} \tag{3.3}\,{}^{b}_{\mathcal{H}\,\mathcal{G}}$$

where $g^{\mu\nu} = \eta^{\mu\nu} + h^{\mu\nu}$ and $\tilde{h}^{\mu\nu} := \sqrt{-g}\, h^{\mu\nu} + (\sqrt{-g}-1)\eta^{\mu\nu}$. With this regrouping we can, as before, obtain the Feynman propagator perturbatively by expanding

$$\Delta_{xy} = i\left\langle \mathrm{T}\,\phi_x\phi_y\,\exp\left\{i\int \mathrm{d}\mu\,\mathcal{L}_I\right\}\right\rangle_{\mathrm{con}}\ . \tag{3.4}\,{}^{b}_{\mathcal{H}\,\mathcal{G}}$$

Inserting the interaction Lagrangian (3.3) results for the first two contributions

$$\Delta_{xy} = -\int \mathrm{d}^4k\ \frac{e^{ikx}}{k^2}\left(e^{-iky} + \int \mathrm{d}\mu_z \int \mathrm{d}^4q\ \frac{e^{iz(q-k)-iqy}}{q^2}\tilde{h}^{\mu\nu}_z k_\mu q_\nu + \mathcal{O}(\tilde{h}^2)\right), \tag{3.5}\,{}^{b}_{\mathcal{H}\,\mathcal{G}}$$

where the leading term according to the construction is the Minkowski propagator.

As a first application of Eq. (3.5) we consider the RNC metric (3.1) up to the third adiabatic order and place one leg of the propagator into the origin $y = 0$ as depicted in Fig. 3.1. Using the inverse RNC metric (3.1), the measure required for $\tilde{h}^{\mu\nu}$ expanded in RNC reads

$$\sqrt{-g}-1=\frac{1}{6}R_{\alpha\beta}x^\alpha x^\beta-\frac{1}{12}R_{\alpha\beta,\gamma}x^\alpha x^\beta x^\gamma \\ -\left(\frac{1}{40}R_{\alpha\beta,\gamma\delta}-\frac{1}{36}R_{\alpha\beta}R_{\gamma\delta}+\frac{1}{180}R_{\alpha}{}^{\lambda}{}_{\beta}{}^{\kappa}R_{\gamma\lambda\delta\kappa}\right)x^\alpha x^\beta x^\gamma x^\delta+\mathcal{O}\left(x^5\right)\,, \tag{3.6}$$

with the Ricci tensor $R_{\alpha\beta}$. This way $\tilde{h}_z^{\mu\nu}$ is a polynomial in z which we can rewrite in terms of partial derivatives acting on the plane waves w.r.t. q, i.e. $z^\mu \to -i\partial_{q_\mu}$. Using integration by parts the derivatives act on q_ν/q^2 and the z integral yields a delta distribution $\delta^{(4)}(k-q)$. Performing the now trivial q integral and neglecting terms of quadratic order in the Ricci scalar R, Ricci tensor, and Riemann tensor, yields

$$\Delta_{x0}=-\int \mathrm{d}^4k\;\frac{e^{ikx}}{k^2}\left(1+\frac{R}{3k^2}-\frac{2R_{\alpha\beta}k^\alpha k^\beta}{3k^4}-iR_{,\mu}\frac{k^\mu}{k^4}+2iR_{\mu\nu,\alpha}\frac{k^\mu k^\nu k^\alpha}{k^6}+\mathcal{O}(R^2)\right), \tag{3.7}$$

in agreement with the RNC propagator in reference [30].

To determine the RNC propagator to the fourth adiabatic order is more involved. Since the reference [30] calculates the propagator for a massive scalar field we also implement a mass for better comparability. To see how the mass term can be included perturbatively in a Minkowski background see App. C. Since here the mass term in the action includes a RNC measure, we split it up into a Minkowski contribution which we put into the free Lagrangian $\mathcal{L}_K=-\eta^{\mu\nu}\partial_\mu\phi\partial_\nu\phi/2-m^2\phi^2/2$ and a curvature correction we include into the interaction Lagrangian $\mathcal{L}_I=-\tilde{h}^{\mu\nu}\partial_\mu\phi\partial_\nu\phi/2+\left(\sqrt{-g}-1\right)m^2\phi^2/2$.

For the fourth adiabatic order we cannot neglect contributions of order $\tilde{h}^2$ anymore and thus we take all parts in Fig. 3.1 into account. Expanding (3.4) to this order we obtain

$$\Delta_{xy}=-\int d^4k\;\frac{e^{ikx}}{k^2+m^2}\Bigg\{e^{-iky}-\int \mathrm{d}\mu_{z_1}\int \mathrm{d}^4q\;\frac{e^{iz_1(q-k)}}{q^2+m^2}\Bigg[e^{-iqy}\left(\tilde{h}_{z_1}^{\mu\nu}k_\mu q_\nu+\tilde{m}_{z_1}^2\right) \\ +\int \mathrm{d}\mu_{z_2}\int \mathrm{d}^4K\;\frac{e^{iz_2(K-q)-iKy}}{K^2+m^2}\left(\tilde{h}_{z_1}^{\mu\nu}\,k_\mu K_\nu\left(\tilde{h}_{z_2}^{\sigma\lambda}K_\sigma q_\lambda+\tilde{m}_{z_2}^2\right)+\tilde{m}_{z_1}^2\tilde{m}_{z_2}^2\right)+\mathcal{O}(\tilde{h}^3)\Bigg]\Bigg\}, \tag{3.8}$$

where $\tilde{m}_x^2:=(\sqrt{-g_x}-1)m^2$. The table below shows to what order n one must expand in $\tilde{h}$ and $\tilde{m}^2$ to capture all contributions up to the desired adiabatic order,

adiabatic order	0	1	2	3	4	5	6	7	$\cdots$
$\tilde{h}^n,\tilde{m}^{2n}$	0	0	1	1	2	2	3	3	$\cdots$

. (3.9)

Therefore, expression (3.8) is valid up to the 5th adiabatic order. Nevertheless, we restrict

ourselves to the fourth adiabatic order since it is the leading order contribution in vacuum spacetimes such as the Schwarzschild spacetime.

As a first sanity check we compute the contributions which include two derivatives of the Riemann tensor and compare them with the results in the literature. For this purpose, terms linear in $\tilde{h}$ and $\tilde{m}^2$ are sufficient and thus the first line in (3.8). Using the single terms of (3.1) and (3.6) which possess two derivatives of the Riemann tensor and inserting them into (3.8) we find

$$\int \mathrm{d}^4k\ \frac{e^{ikx}}{k^2+m^2}\Bigg(k_\mu\Big(\frac{1}{20}R^\mu{}_\alpha{}^\nu{}_{\beta,\gamma\delta}-\frac{1}{40}\eta^{\mu\nu}R_{\alpha\beta,\gamma\delta}\Big)\partial_{k_\alpha}\partial_{k_\beta}\partial_{k_\gamma}\partial_{k_\delta}\frac{k_\nu}{k^2+m^2} \\ -\frac{m^2}{40}R_{\alpha\beta,\gamma\delta}\partial_{k_\alpha}\partial_{k_\beta}\partial_{k_\gamma}\partial_{k_\delta}\frac{1}{k^2+m^2}\Bigg). \tag{3.10}^{bal}_{\mathcal{HG}}$$

We perform all derivatives the propagator becomes

$$-\int \mathrm{d}^4k\ \frac{2e^{ikx}}{5\left(k^2+m^2\right)^3}\left(R^{,\alpha}{}_{,\alpha}-\frac{2k^\alpha k^\beta R_{\alpha\beta}{}^{,\gamma}{}_{,\gamma}}{k^2+m^2}-\frac{6k^\alpha k^\beta R_{,\alpha\beta}}{k^2+m^2}+\frac{12k^\alpha k^\beta k^\gamma k^\delta R_{\alpha\beta,\gamma\delta}}{\left(k^2+m^2\right)^2}\right), \tag{3.11}^{bal}_{\mathcal{HG}}$$

which agrees with the expression in [30].

All correction terms in (3.7) and (3.11) depend on either the Ricci scalar or the Ricci tensor. To shorten the computation we restrict ourselves from now on to vacuum spacetimes and thus neglect all contributions which include the Ricci tensor or the Ricci scalar. The only remaining corrections to the Minkowski propagator up to the fourth adiabatic order are quadratic in the Riemann tensor. The propagator (3.8) for vacuum spacetimes then becomes

$$\begin{aligned}\Delta_{x0} =& -\int \mathrm{d}^4k\ \frac{e^{ikx}}{k^2+m^2}\Bigg(1+k_\mu\left(\frac{\mathcal{X}^{\mu\nu}_{\alpha\gamma\beta\kappa}}{180}-\frac{\mathcal{Y}^{\mu\nu}_{\alpha\gamma\beta\kappa}}{15}\right)\partial_{k_\alpha}\partial_{k_\beta}\partial_{k_\delta}\partial_{k_\kappa}\frac{k_\nu}{k^2+m^2} \\ &-\frac{k_\mu}{9}R^\mu{}_\alpha{}^\nu{}_\beta R^\sigma{}_\delta{}^\lambda{}_\kappa\partial_{k_\alpha}\partial_{k_\beta}\left(\frac{k_\nu k_\sigma}{k^2+m^2}\partial_{k_\delta}\partial_{k_\kappa}\frac{k_\lambda}{k^2+m^2}\right)-\frac{m^2}{180}\frac{\eta_{\mu\nu}}{4}\mathcal{X}^{\mu\nu}_{\alpha\gamma\beta\kappa}\partial_{k_\alpha}\partial_{k_\beta}\partial_{k_\gamma}\partial_{k_\delta}\frac{1}{k^2+m^2}\Bigg) \\ =:& -\int \mathrm{d}^4k\ e^{ikx}\left(\frac{1}{k^2+m^2}+\frac{\mathcal{I}}{180}-\frac{\mathcal{II}}{15}-\frac{\mathcal{III}}{9}-m^2\frac{\mathcal{IV}}{180}\right),\end{aligned} \tag{3.12}^{balv}_{\mathcal{HG}}$$

where $\mathcal{X}^{\mu\nu}_{\alpha\gamma\beta\kappa}=\eta^{\mu\nu}R_\alpha{}^\epsilon{}_\delta{}^\gamma R_{\beta\epsilon\kappa\gamma}$ and $\mathcal{Y}^{\mu\nu}_{\alpha\gamma\beta\kappa}=R^\mu{}_{\beta\delta}{}^\gamma R^\nu_{\alpha\kappa\gamma}$. Notice, the terms $\tilde{h}\tilde{m}^2$ and $\tilde{m}^4$ appearing in (3.8) do not contribute for vacuum spacetimes in fourth adiabatic order.

Performing the derivatives and using the first Bianchi identity $R_{\alpha\beta\gamma\delta}+R_{\alpha\gamma\delta\beta}+R_{\alpha\delta\beta\gamma}=0$ together with the identity $R^{\mu\alpha\beta\gamma}R_{\nu\beta\alpha\gamma}=R^{\mu\alpha\beta\gamma}R_{\nu\alpha\beta\gamma}/2$ we find for the individual terms

$\mathcal{I} = \mathcal{III} = 0$ and

$$-\frac{\mathcal{II}}{15} = \frac{12}{45}\mathcal{Y} - \frac{16}{15}\mathcal{Z} - \frac{k^2}{180}\mathcal{IV}, \qquad -\frac{\mathcal{IV}}{180} = \frac{1}{k^2+m^2}\left(\frac{3}{45}\mathcal{X} - \frac{12}{15}\mathcal{Y} + \frac{32}{15}\mathcal{Z}\right), \quad (3.13)\,{}^{bal\,v}_{\mathcal{HG}}$$

with definitions $\mathcal{X} := R^{\beta\epsilon\kappa\gamma}R_{\beta\epsilon\kappa\gamma}/(k^2+m^2)^3$, $\mathcal{Y} := k^\alpha k^\beta R_\alpha{}^{\epsilon\kappa\gamma}R_{\beta\epsilon\kappa\gamma}/(k^2+m^2)^4$ and $\mathcal{Z} := k^\alpha k^\beta k^\gamma k^\delta R_\alpha{}^\epsilon{}_\beta{}^\kappa R_{\gamma\epsilon\delta\kappa}/(k^2+m^2)^5$. Adding these results into the propagator (3.12) yields

$$\Delta_{x0} = -\int \mathrm{d}^4k\; e^{ikx}\left(\frac{1}{k^2+m^2} + \frac{1}{15}\mathcal{X} - \frac{8}{15}\mathcal{Y} + \frac{16}{15}\mathcal{Z}\right). \quad (3.14)\,{}^{bal\,v}_{\mathcal{HG}}$$

This propagator is consistent with the one in the article [30] and was derived in a fairly simple and straightforward manner. As a result, due to its technical simplicity, using this method to find the propagator in normal neighborhoods appears to be preferable to the established technique presented in [30]. Finally, because we will compute the convolution of the propagator with external sources in Chapter 4 to analyze vacuum persistence in normal neighborhoods, we calculate the following quantity,

$$\sqrt{-g_x}\Delta_{x0} = -\int \mathrm{d}^4k\; e^{ikx}\left(\frac{1}{k^2+m^2} + \frac{4}{15}\mathcal{Y} - \frac{16}{15}\mathcal{Z}\right). \quad (3.15)\,{}^{bal\,v}_{\mathcal{HG}}$$

This is the RNC propagator with one leg in the origin which resolves the leading order correction to the Minkowski propagation. We chose one leg to be in the origin to connect to the results in the literature.

Without choosing a leg of the propagator at the origin, i.e., without $y = 0$ in Eq. (3.5), rewriting the polynomials of z in terms of q derivatives would lead to additional terms depending on y. To avoid this, we first shift the q integral to $p = q - k$ such that (3.5) becomes

$$\Delta_{xy} = -\int \mathrm{d}^4k\,\frac{e^{ikx}}{k^2}\left(e^{-iky} + \int \mathrm{d}\mu_z \int \mathrm{d}^4p\;\frac{e^{izp-i(p+k)y}}{(p+k)^2}\tilde{h}_z^{\mu\nu}k_\mu(p_\nu+k_\nu) + \mathcal{O}(\tilde{h}^2)\right). \quad (3.16)\,{}^{ba}_{\mathcal{HG}}$$

The polynomials in z can now be rewritten in terms of p derivatives such that the propagator to the second adiabatic order reads

$$\begin{aligned}\Delta_{xy} &= -\int \mathrm{d}^4k\,\frac{e^{ikx}}{k^2}\left(e^{-iky} + \int \mathrm{d}^4p\;\delta(p)e^{-i(p+k)y}k_\mu\tilde{h}^{\mu\nu}(i\partial_p)\frac{(p_\nu+k_\nu)}{(p+k)^2}\right)\\ &= -\int \mathrm{d}^4k\,\frac{e^{ik(x-y)}}{k^2}\left(1 + \frac{R}{3k^2} - \frac{2R_{\alpha\beta}k^\alpha k^\beta}{3k^4} + \frac{R_{\alpha\beta}x^\alpha x^\beta}{6k^2} - \frac{R_\alpha{}^{\mu\nu}{}_\beta k_\mu k_\nu x^\alpha x^\beta}{3k^2}\right).\end{aligned} \quad (3.17)\,{}^{bal}_{\mathcal{HG}}$$

As a consistency check for $y \to 0$ we recover Δ_{x0} in (3.7) to the second adiabatic order. We can see that there is already a contribution to this adiabatic order for vacuum spacetimes.

As a result, for vacuum spacetimes up to the second adiabatic order and taking the measures of the convolution with external source into account we obtain

$$\sqrt{-g_x}\Delta_{xy}\sqrt{-g_y} = -\int \mathrm{d}^4k \;\; \frac{e^{ik(x-y)}}{k^2+m^2}\left(1 - \frac{R_\alpha{}^{\mu\nu}{}_\beta k_\mu k_\nu x^\alpha x^\beta}{3(k^2+m^2)}\right). \tag{3.18}$$

As can be seen in (3.6) for a vacuum spacetime up to second adiabatic order $\sqrt{-g_x} = 1$ and thus the measure contributions are not relevant here. In the following Section, we choose the geometry of a thin shell and compute the curvature tensors needed for a RNC construction in the shell's exterior, as well as the RNC propagators.

3.1.2. RNC Patch in a Schwarzschild Geometry

In order to investigate the formation of a black-hole quantum mechanically, we first need a suitable model for the formation. Charged and rotating black-holes exhibit unique effects, such as the Penrose process [46], which we investigate in App. B for the production of a dark matter jet. However, as we are only interested in the formation of any black-hole in this work, we choose a Schwarzschild black-hole. For this purpose, we use a classical, spherically symmetric gravitational collapse that eventually forms a black-hole [47]. Outside the collapsing object of mass M, Birkhoff's theorem dictates a Schwarzschild spacetime [48]. Therefore, in spherical Schwarzschild coordinates (t_S, r, θ, ϕ), the line element of this geometry is

$$\mathrm{d}s^2 = -f(r)\,\mathrm{d}t_S^2 + f^{-1}(r)\,\mathrm{d}r^2 + r^2\mathrm{d}\Omega_2\,, \tag{3.19}$$

with $f(r) = 1 - r_g/r$, the Schwarzschild radius $r_g = 2M$ and $\mathrm{d}\Omega_2 = \mathrm{d}\theta^2 + \sin^2(\theta)\,\mathrm{d}\phi^2$. For radii $r > r_g$ the spacetime is static relative to the observer field $u_S = f^{-1/2}\partial_{t_S}$. The geodesic equation for the trajectories of the Schwarzschild observer γ is $\ddot{\gamma} = r_g/2r^2\,\partial_r$. This acceleration must be maintained by the observer to remain at rest.

Because of the coordinate singularity in (3.19) at $r = r_g$, other observers are advantageous for our considerations, since we will consider objects that can cross the Schwarzschild horizon. In order to consider an observer which can describe horizon crossing we solve the geodesic equation for radial timelike geodesics. Further demanding the observer to follow an inward directed geodesic with radial position $R(\tau)$ we determine the 4 velocity

$$u(R) = \frac{\sqrt{\frac{r_g}{R}}\,u^r + e}{f^2(R)}\,\partial_{t_S} - \sqrt{e^2 - f(R)}\,\partial_r\,, \tag{3.20}$$

with the constant of motion e describing the total energy for a relativistic particle. Notice,

the coordinate velocity of this probe $\mathrm{d}R/\mathrm{d}t_S = u^r/u^{t_S}$ decreases to zero when the probe approaches the horizon and therefore horizon crossing cannot be described.

To change to an observer with 4 velocity (3.20) we compute the dual vector field $u^\star(R) = -\mathrm{grad}[t_P(t_S, r)]|_{r=R}$ with $t_P(t_S, r) = t_S + \int_0^r \mathrm{d}r' u_r^\star(r')$. Expressing the line element (3.19) of the Schwarzschild geometry with $\mathrm{d}t_S = e\mathrm{d}t_P - u_r^\star(r)\mathrm{d}r$ results in the generalized Painlevé-Gullstrand coordinates (t_P, r, θ, ϕ) using as time coordinate the eigentime of a radial infalling observer as in [49],

$$\mathrm{d}s_e^2 = -\left(1 - e^2\chi^2(r)\right)\,\mathrm{d}t_P^2 + 2\chi(r)\,\mathrm{d}r\,\mathrm{d}t_P + \frac{1}{e^2}\mathrm{d}r^2 + r^2\mathrm{d}\Omega_2\,, \tag{3.21}\,{}_{\mathcal{G}}$$

where $\chi(r) = \sqrt{e^2 - f(r)}/e^2$.

In these coordinates, the 4 velocity of a radially infalling probe with total energy e_P is given by

$$u_P(R) = \frac{\sqrt{e^2 - f(R)}u^r + ee_P}{f(R)}\,\partial_{t_P} - \sqrt{e_P^2 - f(R)}\,\partial_r\,. \tag{3.22}\,{}_{\mathcal{G}}^{b}$$

In contrast to the 4 velocity in Schwarzschild coordinates (3.20) there is now a possibility for the coordinate velocity to remain finite at $R = r_g$. Namely, if the observer and the probe share the same total energy $e = e_P$ the coordinate velocity evaluates to $\mathrm{d}R/\mathrm{d}t_P = -\sqrt{r_g/R}$ and horizon crossing can be described.

For simplicity we choose an observer which starts at rest and then freely falls from infinity. The total energy of a non-relativistic particle with speed $v \ll c$ at asymptotic infinity $f(R) \approx 1$ reads [49],

$$e_{\mathrm{N}}^{\mathrm{NR}}(R) = 1 + \frac{v^2}{2} - \frac{M}{R}\,, \tag{3.23}\,{}_{\mathcal{G}}^{b}$$

with the rest energy, kinetic energy and potential energy. Therefore, setting $v = 0$ and $R \to \infty$ results in the total energy $e = 1$. This choice of the observer leads to the standard Painlevé-Gullstrand coordinates and the line element (3.21) becomes

$$\mathrm{d}s^2 = -f\,\mathrm{d}t_P^2 + 2\sqrt{\frac{r_g}{r}}\,\mathrm{d}t_P\,\mathrm{d}r + \mathrm{d}r^2 + r^2\mathrm{d}\Omega_2\,, \tag{3.24}\,{}_{\mathcal{G}}$$

which, as required, is regular at $r = r_g$. The velocity of the free falling observer in these coordinates is given by

$$u(R) = \partial_{t_P} - \sqrt{\frac{r_g}{r}}\,\partial_r\,. \tag{3.25}\,{}_{\mathcal{G}}^{b}$$

To build a RNC patch, we require the vierbein at the anchor point $(t_0, r_0, \theta_0, \phi_0)$ around which we want to expand the background in terms of normal coordinates. For this purpose we take the freely falling observer in Painlevé-Gullstrand coordinates with velocity (3.25) and construct the vierbein by taking $e_0^a = u^a$ and using the identity $g_{ab}^P e_\mu^a e_\nu^b = \eta_{\mu\nu}$. This results in

$$e_0^a = u^a\,, \quad e_1^r = 1\,, \quad e_2^\theta = \frac{1}{r_0}\,, \quad e_3^\phi = \frac{1}{r_0 \sin\theta_0}\,. \tag{3.26}_{\mathcal{G}}$$

To determine the RNC metric (3.1) we require the Riemann tensor in RNC coordinates. Taking the vierbein (3.26) we can transform the Riemann tensor in PG coordinates R_{abcd} to the RNC with $R_{\mu\nu\alpha\beta} = R_{abcd} e_\mu^a e_\nu^b e_\alpha^c e_\beta^d$. The resulting components are

$$R_{0110} = R_{3232} = \frac{r_g}{r_0^3}\,, \quad R_{2020} = R_{3030} = R_{1221} = R_{1331} = \frac{r_g}{2r_0^3}\,. \tag{3.27}_{\mathcal{G}}^{a}$$

Substituting these components into the metric expansion (3.1), we obtain the RNC metric for a radially free-falling observer in a Schwarzschild geometry up to second order. Consideration of the next higher adiabatic order requires the derivatives of the Riemann tensor in RNC,

$$R_{\alpha\beta\gamma\delta,\mu} = e_\alpha^a e_\beta^b e_\gamma^c e_\delta^d e_\mu^m \left(R_{abcd,m} - \Gamma^n_{ma} R_{nbcd} - \Gamma^n_{mb} R_{ancd} - \Gamma^n_{mc} R_{abnd} - \Gamma^n_{md} R_{abcn}\right). \tag{3.28}_{\mathcal{G}}$$

Performing this calculation yields [36]

$$\begin{aligned} R_{0110,0} &= R_{2323,0} = 2R_{2020,0} = 2R_{1221,0} = 2R_{1021,2} = 2R_{3032,2} = 3\frac{r_g}{{r_0}^4}\sqrt{\frac{r_g}{r_0}}\,, \\ R_{1010,1} &= R_{2332,1} = 2R_{0220,1} = 2R_{1212,1} = 2R_{0120,2} = 2R_{2331,2} = 3\frac{r_g}{{r_0}^4}\,. \end{aligned} \tag{3.29}_{\mathcal{G}}$$

Components with an index interchange $2 \leftrightarrow 3$ remain unchanged due to the symmetry between the x^2 and x^3 direction. Note that the RNC metric components show no special behavior for $r_0 = r_g$. As explained before, taking finitely many terms of the RNC expansion into account raises the question about the domain of validity, i.e. the neighborhood around the anchor point in which the RNC are valid.

3.1.3. Domain of Validity of RNC Patches

This Section summarizes the work done with Bruno Högl [36], in which we determine the size and shape of normal neighborhoods at a given adiabatic order and accuracy which improves on earlier works [50–53]. For explicit expressions obtained in this Section we refer the reader to the *Mathematica* code we supplied for this project in [54]. Explicitly,

we take the RNC metric (3.1) and determine the RNC patch size for the leading order term. Computing the neglected higher order terms then allows us to estimate how far one can move away from the origin before the requirement on the smallness can no longer be achieved. We first demonstrate this procedure in a general framework and then apply it to determine the RNC patch size in a Schwarzschild geometry which we will require in Chapter 4.

Using a superscript to denote the adiabatic order, we require higher order terms of the RNC metric $g^{(n)}$ in (3.1) to be negligible, i.e.

$$\left|{g_{\alpha\beta}}^{(n+k)}(x) - {g_{\alpha\beta}}^{(n)}(x)\right| \leq \delta \left|{g_{\alpha\beta}}^{(n)}(x)\right|, \tag{3.30}\,{}^{a}_{\mathcal{G}}$$

with $\mathbb{N} \ni k \geq 2$ and the smallness parameter $\delta \in \,]\,0, 1]$ with $\delta \ll 1$ which reflects the maximally allowed metric mismatch for the application in question. The patch size obtained for $g^{(n)}$ is more accurate the more higher order terms are computed and used for the comparison with $g^{(n)}$. Ideally, with $k \to \infty$ all higher order terms are taken into account leading to perfect accuracy.

The metric itself is not an observable, but occurs, for example, fully contracted in the action of physical systems such as point particles or scalar fields as in (3.2). We then use this action to compute metric-sensitive observables. Taking this into account, we can deal with certain troublesome behaviors of the truncated metric expansion, e.g. that an off-diagonal component $g^{(n)}_{\alpha\beta}(x)$ becomes small compared to ${g_{\alpha\beta}}^{(n+1)}(x) - {g_{\alpha\beta}}^{(n)}(x)$ or that $g^{(n)}_{\alpha\beta}(x)$ even vanishes for certain x. In the action, such minimal contributions are irrelevant because of the contraction of the metric. We therefore compare the terms of adiabatic order $n + k$ with the maximum of all components at adiabatic order n and therefore exchange Eq. (3.30) with

$$\left|{g_{\alpha\beta}}^{(n+k)}(x) - {g_{\alpha\beta}}^{(n)}(x)\right| \leq \delta \max\nolimits^{\text{diag}}_{\alpha,\beta} \left\{\left|g^{(n)}_{\alpha\beta}(x)\right|\right\}, \tag{3.31}\,{}^{a}_{\mathcal{G}}$$

where we denote $\max^{\text{diag}}_{\alpha,\beta}\{g_{\alpha\beta}\}$ for $\max\{g_{\alpha\beta}, g_{\alpha\alpha}, g_{\beta\beta}\}$, where $g_{\alpha\alpha}$ and $g_{\beta\beta}$ are the diagonal components to an off-diagonal component $g_{\alpha\beta}$ ($\alpha \neq \beta$).

As a first application of (3.31) we find the size of the leading order Minkowski patch for a Schwarzschild geometry by taking $n = 0$ and demanding the first curvature correction to vanish, i.e. $k = 2$. Solving Eq. (3.31) for x then determines the maximal x which we denote with $x^{(0)}_{\backslash R}$ by expressing the adiabatic order of the truncated metric series in the superscript and the highest adiabatic terms used on the left-hand side of (3.31) in the subscript. Here, the adiabatic order of the truncated metric series is $n = 0$ and the highest adiabatic order of the truncated metric $k = 2$ which we denote with $\backslash R$ indicating

that the Riemann term in the RNC metric is truncated. For $n = 0$, the right-hand side of (3.31) is just δ since $\max_{\alpha,\beta}^{\text{diag}} \{|\eta_{\alpha\beta}|\} = 1$, $\forall\, \alpha, \beta$. To determine the full patch size, we first compute the extent along the RNC axes. This means, we set all x's except one x^μ to zero and consider (3.31) with $x^\nu = 0$, $\forall\, \nu \neq \mu$. Inserting the Riemann tensors (3.27) of the RNC patch in a Schwarzschild background into (3.31) yields the following set of conditions,

$$x_{\setminus R}^{\mu\,(0)} = \pm\sqrt{3} D \sqrt{\delta}, \quad \forall\, \mu\,, \tag{3.32}\,{}^{a}_{\mathcal{G}}$$

where we defined $D = r_g \left(r_0/r_g\right)^{3/2} = r_0 \sqrt{r_0/r_g}$.

Second, we analyze all possible x^μ-x^ν combinations in (3.31) while setting the other x's to zero. We start with the x^0-x^1 combination and thus set $x^2 = x^3 = 0$. The mismatch between the *eta* patch and the RNC metric of second adiabatic order is plotted in Fig. 3.2a) with a black shading denoting the maximally allowed error *delta* and the lightest gray shading denoting a vanishing error in the origin. The domain of validity is a square and therefore the conditions along the x^0 and x^1 axes are valid for all combinations of the two coordinates. This means, the condition in (3.32) correctly determines the boundary of the domain of validity. Next, the combination x^0-x^2 is depicted in Fig. 3.2b) which clearly deviates from a square shape. Therefore, the condition (3.32) does not account for the border of the domain of validity and it must be adjusted. The correct description of the shape in Fig. 3.2b) is involved but still resembling a square. Therefore we shrink the patch along the diagonals and let it remain a square. Applying this yields new conditions for x^0 and x^2 given by

$$x_{\setminus R}^{0\,(0)} = \pm\sqrt{2} D \sqrt{\delta}\,, \qquad x_{\setminus R}^{2\,(0)} = \pm\sqrt{2} D \sqrt{\delta}\,. \tag{3.33}\,{}^{a}_{\mathcal{G}}$$

The combination $x^0 - x^3$ yields an identical patch as in Fig. 3.2b), and therefore the x^3 condition is also replaced by

$$x_{\setminus R}^{3\,(0)} = \pm\sqrt{2} D \sqrt{\delta}\,. \tag{3.34}\,{}^{a}_{\mathcal{G}}$$

All other x^μ-x^ν combinations do not add new restrictions.

As a third step, we consider the x^μ-x^ν combinations with only one x set to zero. A patch of particular interest is shown in Fig. 3.2c) for the x^2-x^3 combination with $x^0 \neq 0$ and $x^1 = 0$. The domain of validity is a circle with radius $\sqrt{6D^2\delta - 2(x^0)^2}$, which is more restrictive than the conditions before and thus we add this condition to $x_{\setminus R}^{0\,(0)}$, $x_{\setminus R}^{2\,(0)}$, and $x_{\setminus R}^{3\,(0)}$. With this condition all other combinations are satisfied as well.

Fourth, the x^μ-x^ν combinations without setting any x's to zero, yield domain of va-

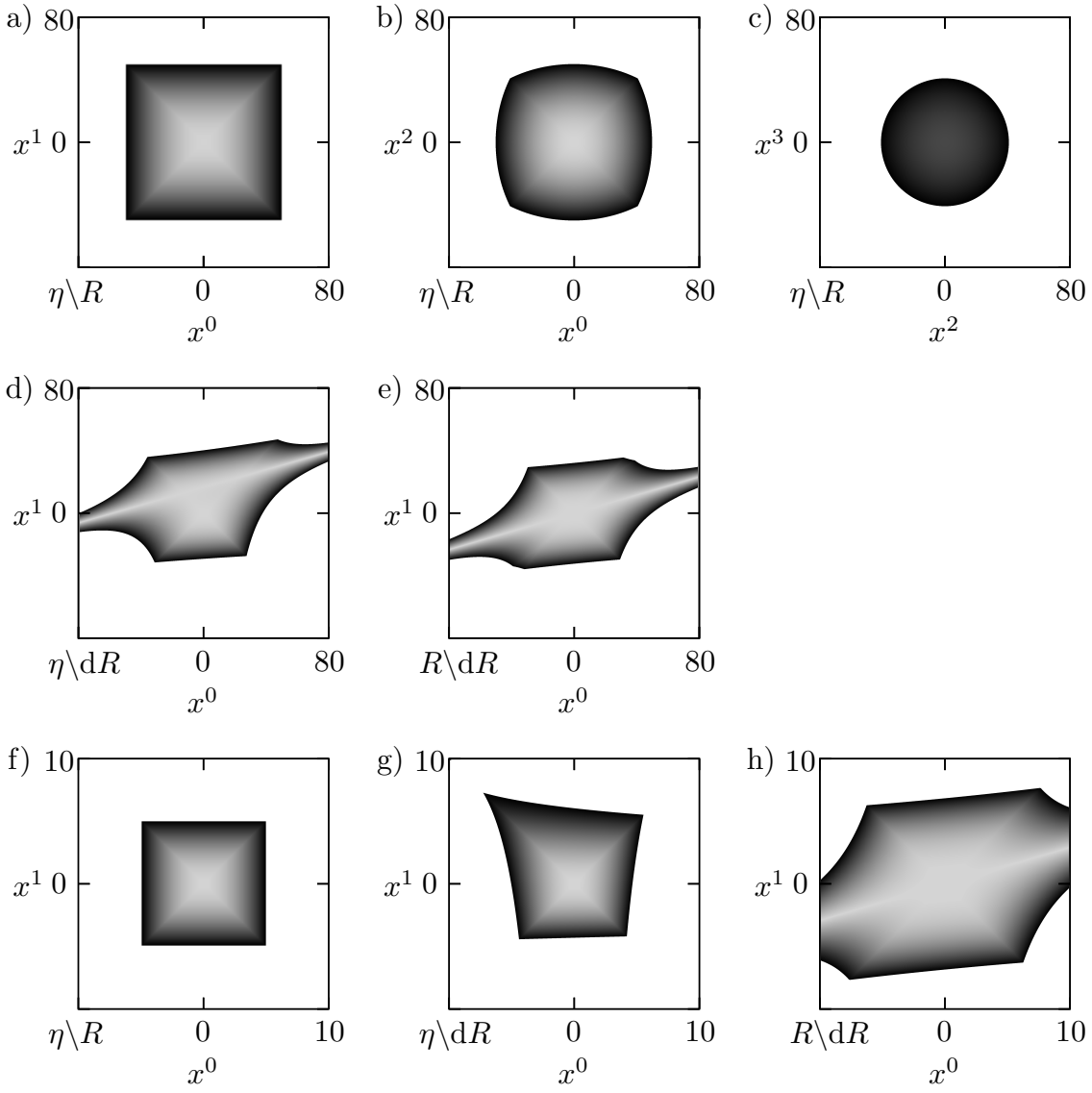

Figure 3.2.: In a) - c) and f) we show the Minkowski patches resulting from neglecting the second order Riemann term and thus denoted by $\eta\backslash R$. Minkowski patches obtained from neglecting the second and third order terms are denoted by $\eta\backslash \mathrm{d}R$ and are given in d) and g). Second-order RNC patches for which the third-order term is discarded are denoted by $R\backslash \mathrm{d}R$ and are given in e) and h). Darker shades of gray correspond to a larger error up to the black area indicating the maximal allowed error δ. White areas indicate an error greater than δ and are therefore outside the range of validity. The parameters for a) - e) are $M = 1$, $r_0 = 24$, $\delta = 0.1$ and for f) - h) $\delta = 10^{-3}$. All not displayed directions x^μ are taken to be zero except in c), where x^0 is set to its maximum value of 37.

lidities which do not restrict the previous conditions any further. Therefore, Eq. (3.31) results in the following conditions for the Minkowski patch:

$$\begin{aligned}
\left|x^{0\,(0)}_{\setminus R}\right| &\leq \min\left\{\sqrt{2}D\sqrt{\delta}, \sqrt{3D^2\delta - \frac{(x^2)^2+(x^3)^2}{2}}\right\},\\
\left|x^{1\,(0)}_{\setminus R}\right| &\leq \sqrt{3}D\sqrt{\delta}\,,\\
\left|x^{2\,(0)}_{\setminus R}\right| &\leq \min\left\{\sqrt{2}D\sqrt{\delta}, \sqrt{6D^2\delta - (x^3)^2 - 2(x^0)^2}\right\},\\
\left|x^{3\,(0)}_{\setminus R}\right| &\leq \min\left\{\sqrt{2}D\sqrt{\delta}, \sqrt{6D^2\delta - (x^2)^2 - 2(x^0)^2}\right\}.
\end{aligned} \tag{3.35}\,{}^{a}_{\mathcal{G}}$$

The last two conditions display the polar symmetry of the patch reflecting the spherical symmetry of the Schwarzschild geometry.

The conditions for the domain of validity in (3.35) are expressed in terms of RNC. We select certain geodesics along which we wish to calculate the patch size in order to translate it into PG coordinates. First, we consider the geodesic of a freely infalling probe with 4-velocity (3.25). By construction in this RNC patch the probe is at rest. With the conditions (3.35) the maximal valid eigentime reads $\tau^{(0)}_{\mathrm{PG}} := \max\left\{\left|x^{0\,(0)}_{\setminus R}\right|\right\} = \sqrt{2}D\sqrt{\delta}$. The reparametrization of the curve with the observer's eigentime is here simply given by $t_{\mathrm{obs}} = t_{\mathrm{PG}} = \tau$. Therefore, we integrate (3.25) yielding $r(\tau)$ and insert $\tau^{(0)}_{\mathrm{PG}}$ to determine the minimal radial value of the PG observer's geodesic for which the Minkowski patch is still valid,

$$r_{\min} = r\left(\tau^{(0)}_{\mathrm{PG}}\right) = r_0\left(1 - \frac{3}{\sqrt{2}}\sqrt{\delta}\right)^{\frac{2}{3}}. \tag{3.36}\,{}^{a}_{\mathcal{G}}$$

Placing the anchor point of the RNC r_0 sufficiently close to r_g and taking a sufficiently large δ, the RNC patch can cross the event horizon and extend into the black-hole. For example, taking $r_0 = 2.1M$ with $\delta = 0.01$ yields $r_{\min} \approx 1.79M$.This is due to the aforementioned regularity of RNC at the horizon. Arbitrary far away from the black-hole $r_0 \to \infty$ the patch size becomes arbitrarily large reflecting the asymptotic flatness of the Schwarzschild geometry.

It is important to note, that Eq. (3.36) may not be used in a region with quickly changing background curvature. This might cause problems take too few derivatives of the metric into account and/or choose the maximally allowed error δ too large. For example, for $\delta = 2/9$ Eq. (3.36) returns the minimal radius $r_{\min} = 0$ which of course is unreasonable. Therefore, we have to restrict to certain values of r_0 and δ if we want to use Eq. (3.36). If these values are too restricting for the application in question, we have to take higher orders of the metric expansion into consideration, either by using a $g^{(n)}$ patch instead of

the Minkowski patch or by calculating the validity of the Minkowski patch using (3.31) with $k > 2$. We investigate both possibilities and start with calculating the Minkowski patch size using (3.31) with $k = 3$. Performing the same procedure as before, instead of (3.35) we then obtain the following improved conditions for the Minkowski patch,

$$\begin{aligned}
\left|x^{0\,(0)}_{\backslash \mathrm{d}R}\right| &\leq \sqrt{2}D\sqrt{\delta} - \frac{5}{2}D\delta \,, \\
\left|x^{1\,(0)}_{\backslash \mathrm{d}R}\right| &\leq \sqrt{3}D\sqrt{\delta} - \frac{9}{4}\sqrt{\frac{r_0}{r_g}}D\delta \,, \\
\left|x^{2\,(0)}_{\backslash \mathrm{d}R}\right| &\leq \min\left\{\sqrt{2}D\sqrt{\delta} - \frac{5}{2}D\delta, \frac{\sqrt{12D^3\delta - (x^3)^2\,(9x^0+2D) - 2(x^0)^2\,(3x^0+2D)}}{\sqrt{9x^0+2D}}\right\}.
\end{aligned} \tag{3.37}\,{}^{a}_{\mathcal{G}}$$

We label these conditions with $\backslash \mathrm{d}R$, because now we take into account the RNC metric (3.1) up to the third adiabatic order which depend on the derivatives of the Riemann tensor. Notice, since the exact conditions are very lengthy we Taylor expanded them in δ, except for the directional dependence term. The x^3 condition can be obtained by symmetry from the x^2 condition by interchanging x^2 with x^3. Finally, we also have a condition for the directional dependence of x^0 which follows from solving the x^2 or x^3 condition for x^0. Notice, δ has to be taken sufficient small such that the RHS of the conditions (3.37) are strictly positive.

As before, we altered the patches obtained in the iteration technique in the simplest, yet most sensible, way to generate the suitable functional dependencies in (3.37). Consider, for example, the domain of validity shown in Fig. 3.2d), in particular the diagonal "arms" of the patch that extend to infinity. This plot corresponds to a non-compact, open domain of validity, which is unreasonable and therefore we remove these "arms". We will go into more detail about why they should be removed when we discuss Fig. 3.3.

Translating the domain of validity (3.37) to PG coordinates as we did to find (3.36), the minimal radial value of validity is

$$r_{\min} = r_0\left(1 - \frac{3}{\sqrt{2}}\sqrt{\delta} + \frac{15}{4}\delta\right)^{\frac{2}{3}}. \tag{3.38}\,{}^{a}_{\mathcal{G}}$$

For the example we chose before $r_0 = 2.1M$ and $\delta = 0.01$ the minimal radius is $r_{\min} \approx 1.85M$ which is larger than the value obtained with (3.36). Considering higher orders of the metric series improves the domain of validity in terms of the accuracy in describing the background, but does not necessarily enlarge it. For example, the patch in Fig. 3.2d), which includes higher orders of the metric series, is smaller than that depicted in Fig. 3.2a).

As already mentioned, we now derive the domain of validity of a RNC patch which includes the first curvature corrections, i.e. taking the metric $g^{(n)}(x)$ with $n = 2$. The domain of validity of such a $g^{(2)}$ is then obtained

$$\left|x^{0\,(2)}_{\backslash \mathrm{d}R}\right| = \left|x^{1\,(2)}_{\backslash \mathrm{d}R}\right| \leq \left(\frac{2}{\sqrt{r_0/r_g}+1}\right)^{\frac{1}{3}} D\delta^{\frac{1}{3}} + \frac{8}{9}\frac{D}{\sqrt{r_0/r_g}+1}\delta\,,$$
$$\left|x^{2\,(2)}_{\backslash \mathrm{d}R}\right| \leq \min\left\{\left(\frac{4}{3\sqrt{r_0/r_g}}\right)^{\frac{1}{3}} D\delta^{\frac{1}{3}} - \frac{8}{27}\frac{D}{\sqrt{r_0/r_g}}\delta, r_0\frac{6D^2+(x^1)^2-2(x^3)^2}{6x^1x^3}\delta\right\}. \tag{3.39}^{a}_{\mathcal{G}}$$

As before, we Taylor expanded the conditions in δ. The x^0 and x^1 conditions are equal except for an additional directional x^1 dependence which we again find by solving the x^2 condition for x^1. We again insert $x^{0\,(2)}$ into the PG observer's geodesic for $r_0 = 2.1M$, $\delta = 0.01$ and find $r_{\min} \approx 1.61M$. The patch now reaches further into the black-hole which was achieved by including curvature corrections.

Notice, this enlargement crucially depends on δ. For example, the $g^{(2)}$ patch size in the x^0-x^1 plane depicted in Fig. 3.2e) is smaller than the Minkowski patch sizes in Fig. 3.2a) and Fig. 3.2d). This is because an error of $\delta = 0.1$ is too large for a reference point placed at $r_0 = 24M$. If we reduce the error to be $\delta = 10^{-3}$, we find instead the three patches depicted in Fig. 3.2f), Fig. 3.2g) and Fig. 3.2h). Now Fig. 3.2f) and Fig. 3.2g) almost agree, with the latter being slightly larger, as expected. This can also be seen through the agreement of the conditions in (3.35) and (3.37) in the x^0-x^1 plane in the limit $\delta \to 0$, as the higher order terms in (3.37) become strictly irrelevant. Furthermore, the $g^{(2)}$ patch in Fig. 3.2h) is now substantially larger than both Minkowski patches. Therefore, we conclude that for this setup the error $\delta = 10^{-3}$ is a good choice while $\delta = 0.1$ is not.

This growth of the range of validity continues for higher order metric expansions. To this end, we consider the metric $g^{(n)}$ for $n = 3$ and $n = 4$. However, since the conditions for the $g^{(3)}$ and $g^{(4)}$ patch are extensive, we demonstrate the increase in patch size graphically. In Fig. 3.3 we plotted the $g^{(4)}$ patch in the x^0-x^1 plane for $\delta = 10^{-3}$. In addition, we show the edge regions of the Minkowski patch from Fig. 3.2f) and the $g^{(2)}$ patch from Fig. 3.2h) as well as the $g^{(3)}$ patch. Overall, we observe a continuous growth of the patch sizes with increasing adiabatic order n. We can see that the arms which extend to infinity in the $g^{(2)}$ patch disappear for the $g^{(3)}$ patch and reappear for $g^{(4)}$. These arms are formed along a line describing combinations of x^0 and x^1 for which the first and third derivatives of the Riemann tensor vanish, which implies that the coefficients of $g^{(3)} - g^{(2)}$ and $g^{(5)} - g^{(4)}$ vanish. We can safely ignore such pathological arms, since considering higher orders in the calculation of patch sizes, namely by using (3.31) with $k \geq n+1$, cancels these arms.

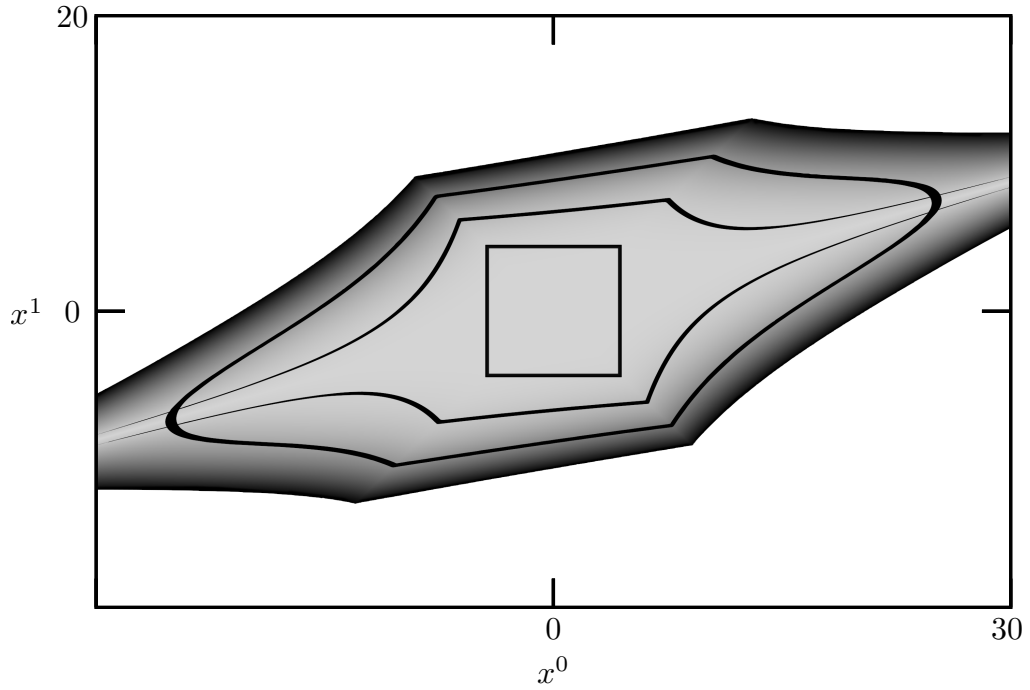

Figure 3.3.: The smallest and the second smallest patch are those of Figs. 3.2f) and 3.2h), while the next larger patch corresponds to $g^{(3)}$ for $M = 1$ and $r_0 = 24$. These boundaries correspond to an error of $\delta \in [\,0.9 \times 10^{-3}, 10^{-3}\,]$ and thus the thickness of the boundary lines for the patches with $n = 0, 2, 3$ shows how fast the error grows for the respective patches: the thicker the boundary, the slower the error grows. The fourth order patch with maximal error $\delta = 10^{-3}$ is shown completely. The change in size and shape of the patches with increasing order is complicated, but a qualitative increase can be seen.

This becomes clear when we consider the $g^{(3)}$ patch. It is computed using only $k = 4$, but since the coefficient of $g^{(4)} - g^{(3)}$ also depends on terms depending only on the Riemann tensor and not its derivative, this coefficient is finite along this line, and thus the arms do not appear. Analogously, higher order terms of even n do not depend only on derivatives of the Riemann tensor and their consideration in the calculation of, e.g., the $g^{(4)}$ patch would lead to the truncation of the arms.

With the domain of validity of RNC patches being large enough to cross an event horizon, one immediate question arises. Does causality, restricting every geodesic starting inside a black-hole remains inside, also hold for RNC patches covering a part of the interior and a part of the exterior? We answer this question in the next Section.

3.1.4. Causality at the Event Horizon in RNC Patches

In the previous Section, we saw that RNC patches can cross the horizon of a black-hole. Therefore, we want to investigate the causal structure for such patches, i.e. whether the horizon can be crossed by a probe only from the outside to the inside. The event

horizon for an eternal black-hole is also an apparent horizon [55]. The latter, in contrast to the event horizon, allows a description in finite spacetime regions and is therefore the preferred object for analyzing the causal structure locally [55]. For spherically symmetric spacetimes, apparent horizons are characterized as the null hypersurface through which radially outward light rays change the sign of their coordinate velocity. For a Schwarzschild spacetime in PG coordinates, this velocity is given by $(1, 1-\sqrt{r_g/r}, 0, 0)$ and thus the sign change occurs at $r = r_g$. We can also specify this radial position of the apparent horizon as the radius reached by the PG observer after the proper time $\tau_{\mathrm{PG}}(r_0) = 2/3(D - r_g)$, measured from the reference point at $r = r_0$.

We first study causality at the horizon for the leading order Minkowski patch of a RNC expansion. We anchor this patch at a reference point outside the horizon, but close enough to it that a small neighborhood of the reference point covers a portion of the horizon. To describe the horizon in RNC coordinates, we transform the velocity $(1, 0, 0, 0)$ into PG coordinates using the vierbein (3.26), giving $\lambda^0 = 1$ and $\lambda^1 = \sqrt{r_g/r_0}$. In addition, we shift the resulting line so that it intersects the x^0 axis at $x^0 = \tau_{\mathrm{PG}}$ thereby describing the horizon by the straight line $\Omega(x^0) = (x^0, \sqrt{r_g/r_0}(x^0 - \tau_{\mathrm{PG}}), 0, 0)$. As will be legitimated in the next paragraph, the reference point must be arbitrarily close to the horizon for this construction to be valid. Thus, for $r_0 \to r_g$, we get $\mathrm{d}\Omega^\alpha/\mathrm{d}x^0 \to (1, 1, 0, 0)$.

In this construction, the horizon is given by the upper dashed line in the spacetime diagram in Fig. 3.4, which is drawn here with 45°, but is to be understood a little bit steeper, since we have $\mathrm{d}\Omega^1/\mathrm{d}x^0 = \sqrt{r_g/r_0} < 1$ for $r_0 > r_g$. The light geodesics directed radially outward from the reference point $(0, 0)$ follow the lower dashed line with 45°. For negative x^0, there is a crossing point of the horizon with the outgoing light rays, which is pathological because the geodesics cross the horizon from the inside to the outside. This indicates the collapse of the validity to perform the parallel shift of the horizon. Thus, for large x^0, the horizon is no longer represented by the parallel-shifted line that describes it well for small x^0. Since in the limit $r_0 \to r_g$ the horizon satisfies $\mathrm{d}\Omega^1/\mathrm{d}x^0 \to 1$, the intersection then shifts to $x^0 \to -\infty$. So, for an anchor point of the RNC sufficiently close to the horizon, the collapse of the parallel shift can be taken far outside the domain of validity of the normal coordinates such that we can use the parallel shift.

For a RNC expansion anchored at the apparent horizon $r_0 = r_g$, the horizon is given by the lower dashed line in Fig. 3.4. Outward directed light rays emitted at the origin remain at the horizon. Any time-like geodesic touches the horizon only at the anchor point and is always inside the black-hole thereafter.

Finally, choosing the reference point inside the black-hole $r_0 < r_g$, the horizon intersects the x^0 axes at negative x^0 and infinitely less steeply than 45°, since now $\mathrm{d}\Omega^1/\mathrm{d}x^0 > 1$. Thus, as expected, all light rays starting at the reference point remain in the black-hole.

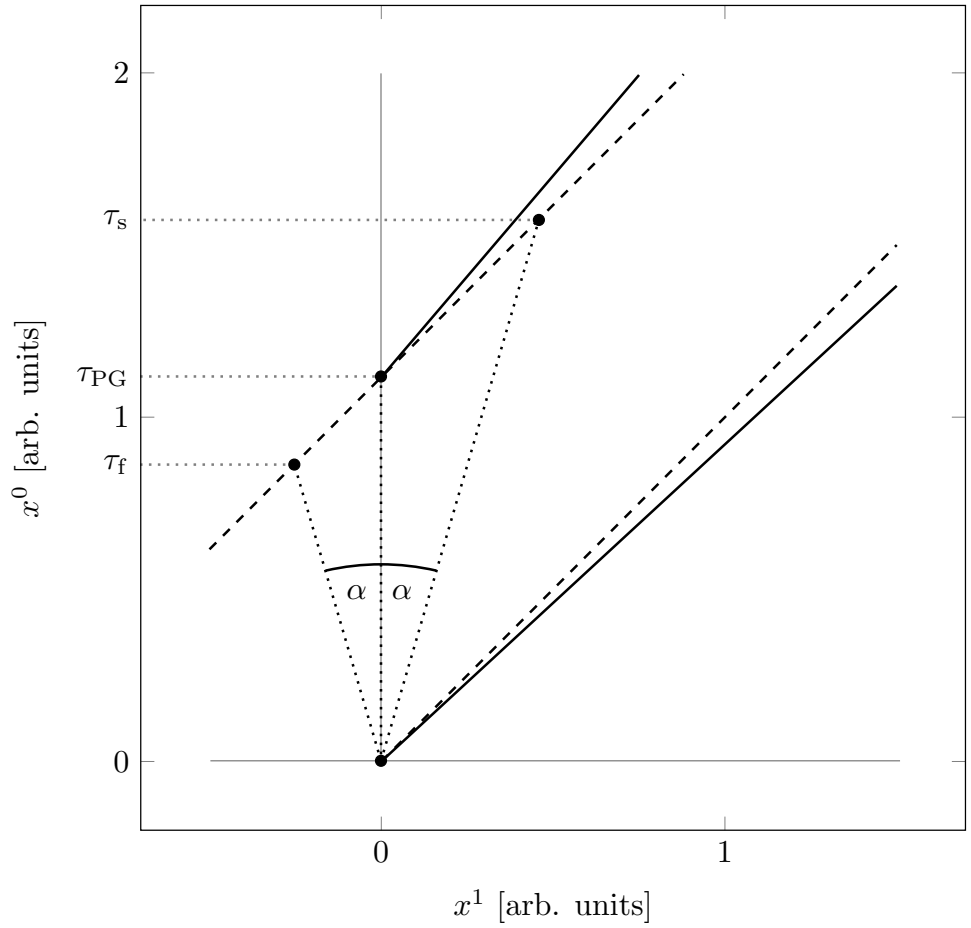

Figure 3.4.: Shown are geodesics for radially outward directed light rays in a RNC patch of a Schwarzschild geometry. The dashed lines represent the outgoing null geodesics in for the leading order RNC contribution, i.e. the Minkowski patch with $x^0 = x^1 + \text{const}$. The dotted lines correspond to three timelike observers following radially infalling geodesics with different initial velocities. The solid lines are outward null geodesics taking the first curvature correction in the RNC into account.

Note, however, that the outward directed light rays follow the line $(x^0, x^0, 0, 0)$, and thus appear to the RNC observer as outgoing. For negative x^0 we again see a collapse of the parallel shift of the horizon, which can be avoided by constructing the RNC sufficiently close to the horizon.

In addition, we want to test whether the causal ordering of events in PG coordinates remains the same in the RNC. For that purpose, we consider two additional timelike observers on radial geodesics starting at the reference point r_0 outside the black-hole. In PG coordinates, one observer starts with an inward radial velocity $v^r = V_f \in]-\infty, -\sqrt{r_g/r_0}\,[$ faster than that of the free-falling PG observer and the second with the slower one $v^r = V_s \in]-\sqrt{r_g/r_0}, 0\,]$ as depicted in Fig. 3.4. Using the vierbein (3.26), we trans-

form v^r to obtain the velocity in RNC,

$$\lambda^0(V) = \frac{\sqrt{\frac{r_g}{r_0}}V + \sqrt{V^2 + f(r_0)}}{f(r_0)}\,, \quad \lambda^1(V) = \frac{V + \sqrt{\frac{r_g}{r_0}}\sqrt{V^2 + f(r_0)}}{f(r_0)}\,. \tag{3.40}\,{}^{b\,a}_{\mathcal{G}}$$

These fulfill $\lambda^0(V) > 1$, $\forall\, V, r$ as well as $\lambda^1(V_\mathrm{f}) < 0$ and $\lambda^1(V_\mathrm{s}) > 0$, $\forall\, r$. We now check whether the angles $\alpha(V_\mathrm{s})$ and $\alpha(V_\mathrm{f})$, which are between the world line of the PG observer $(x^0, 0, 0, 0)$ and the other observers $(x^0\lambda^0(V), x^0\lambda^1(V), 0, 0)$ is always smaller than $\pi/4$, i.e. if they are causally connected. These angles are determined to be $\alpha(V_\mathrm{s}) = \pi/2 - \tan^{-1}(\lambda^0(V_\mathrm{s})/\lambda^1(V_\mathrm{s}))$ and $\alpha(V_\mathrm{f}) = \pi/2 + \tan^{-1}(\lambda^0(V_\mathrm{f})/\lambda^1(V_\mathrm{f}))$. To satisfy the above causal condition $\lambda^0(V_\mathrm{s})/\lambda^1(V_\mathrm{s}) > 1$ and $\lambda^0(V_\mathrm{f})/\lambda^1(V_\mathrm{f}) < -1$ must hold, which is the case for all possible V_s and V_f, respectively. Moreover, we verify that the faster observer reaches the horizon earlier than the PG observer and that the slower observer takes longer. The PG observer crosses the horizon after the proper time τ_PG. As before, suppose the horizon is described by an angle 45° and require for the correct causal ordering demands $\tau_\mathrm{f} = \tau_\mathrm{PG} + \lambda^1(V_\mathrm{f})\tau_\mathrm{PG} < \lambda^0(V_\mathrm{f})\tau_\mathrm{PG}$ for the faster observer and $\tau_\mathrm{s} := \tau_\mathrm{PG} + \lambda^1(V_\mathrm{s})\tau_\mathrm{PG} > \lambda^0(V_\mathrm{s})\tau_\mathrm{PG}$ for the slower one. These conditions are also fulfilled for all possible V_f and V_s. The same analysis can be done for a RNC patch constructed inside the black-hole yielding the same causal results.

So far we have calculated the geodesics in the global PG coordinates and transformed them to RNC. There is no causality violation in the PG coordinates, which we have successfully translated into the RNC. It remains to be investigated whether a causality violation occurs in RNC when the geodesic equations are solved directly in RNC using a truncated metric.

As before, we consider a small neighborhood of the reference point crossing the apparent horizon and take into account the first curvature correction. Setting $x^1 = 0$ for radially outward directed light rays, we obtain for the coordinate velocity

$$v^1(x^0)\big|_{x^1=0} = \left.\frac{\mathrm{d}x^1}{\mathrm{d}x^0}\right|_{x^1=0} = \left(1 - \frac{(x^0)^2}{3r_g^2}\right)^{-\frac{1}{2}}. \tag{3.41}\,{}^{a}_{\mathcal{G}}$$

Within the domain of validity (3.39), the argument on the right-hand side is strictly positive, since for $(x^0)^2 > 3r_g^2$ an error of $\delta > 1$ would be needed causing a breakdown of the perturbation series.

The coordinate velocity (3.41) indicates that the geodesics start steeper the later they start from $x^1 = 0$. Therefore, the lines corresponding to outward light rays inside the black-hole with $x^0 > \tau_\mathrm{PG}$ are steeper than the line corresponding to the horizon with τ_PG, and therefore do not cross it and remain inside the black-hole. The expressions for the

complete coordinate velocity and the corresponding geodesics are very lengthy. Therefore, to question causality for $x^1 \neq 0$, we plot two example geodesics in Fig. 3.4 with solid lines instead of analyzing their analytic expressions. We can see that a line starting at $x^1 = 0$ becomes steeper the later it starts. This has the consequence that lines starting later and thus steeper at $x^1 = 0$ only become steeper in comparison to the horizon. Therefore, light rays directed outward can indeed not leave the black-hole no matter how r_0 is chosen.

If we choose the expansion point outside the black-hole with $r_0 > r_g$, then the upper solid line in Fig. 3.4 describes the horizon and the lower solid line represents light rays emitted at the reference point. The latter departs radially outward from the horizon and thus moves away from the black-hole, which is not the case for an Minkowski patch of the RNC, as can be seen from the dashed lines, which have a constant distance.

In summary, this Section shows that no matter where one constructs a RNC patch, even near an event horizon, causality within the patch is respected. This reinforces the statement that normal coordinates taking only a finite adiabatic order into account are always valid when used in a sufficiently small neighborhood, even though it might cross an apparent horizon.

3.1.5. Temporally Expanded Fermi Normal Coordinates

In Sec. 3.1.3 we demonstrated that RNC coordinates are valid only for a finite amount of time. If an application in question requires the temporal validity of the metric to be larger than the one of the RNC, other normal coordinates are favored. For instance, Fermi normal coordinates (FNC) as developed in [50] are another set of normal coordinates with a longer temporal validity. Instead of a point as in the RNC case, their construction relies on a whole geodesic $\gamma(\tau)$.

Starting from an arbitrary reference point $p = \gamma(0)$ on the geodesic $\gamma(\tau)$, the FNC of a point q are constructed as illustrated in Fig. 3.5. The geodesic γ is followed until $\gamma(x^0)$, where a RNC expansion is performed in the orthogonal directions. For these orthogonal RNC we take the geodesic $\omega_{x^0}(\zeta)$ with $\omega_{x^0}(0) = \gamma(x^0)$ and $\mathrm{d}\omega_{x^0}/\mathrm{d}\zeta|_0 = v \perp \mathrm{d}\gamma/\mathrm{d}\tau|_{x^0}$ that reaches the point q at $\zeta = \zeta^0$. For clarity, since the RNC expansion describes the spatial part of the FNC, we label the associated coordinates with indices $\bar{\alpha}$. The point q is then described with the coordinates $(x^0, x^{\bar{1}}, x^{\bar{2}}, x^{\bar{3}})$ with $x^{\bar{\alpha}} = \zeta\lambda^{\bar{\alpha}}$. The $\lambda^{\bar{\alpha}}$ are obtained as before by expanding v in terms of the vierbein at $\gamma(x^0)$, $v^a = \lambda^{\bar{\alpha}} e^a_{\bar{\alpha}}(x^0)$ with $\eta_{\bar{\alpha}\bar{\beta}}\lambda^{\bar{\alpha}}\lambda^{\bar{\beta}} = 1$. The vierbein along the geodesic γ is constructed with $e^a_0(\tau) = \mathrm{d}\gamma^a(\tau)/\mathrm{d}\tau$ and the remaining components $e^a_{\bar{\alpha}}$ fixed by requiring orthonormality. Therefore, the interval of the geodesic γ determines $(x^0, 0, 0, 0)$ and the orthogonal geodesics yield $\zeta(0, \lambda^{\bar{1}}, \lambda^{\bar{2}}, \lambda^{\bar{3}})$ at every point $\gamma(x^0)$.

Since FNC is based on the RNC construction, the metric expansions are given by close

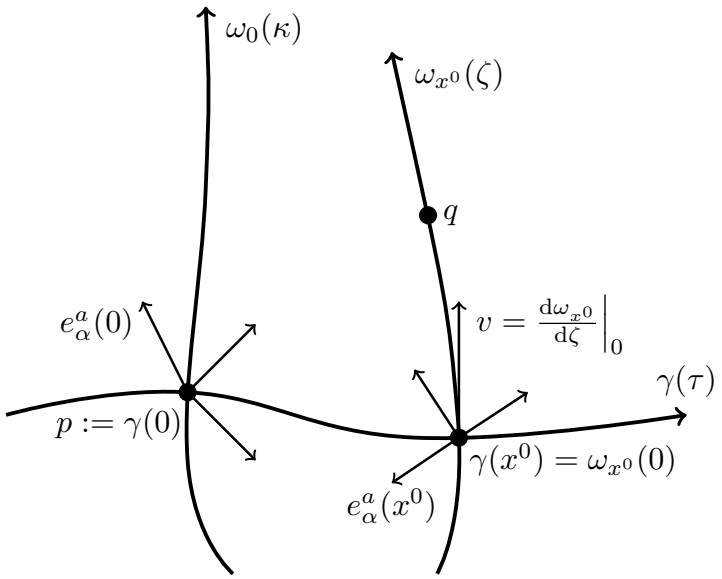

Figure 3.5.: Depicted is the FNC construction along the geodesic $\gamma(\tau)$ with orthogonal RNC expansions at the points p and $\gamma(x^0)$ with vierbeins $e^a_\alpha(0)$ and $e^a_\alpha(x^0)$. The latter is used to find the FNC coordinates of the point q.

analogy to (3.1) by [50]

$$g_{\alpha\beta}(x) = \eta_{\alpha\beta} - G(\alpha,\beta)R_{\alpha\bar{\mu}\beta\bar{\nu}}(x^0)x^{\bar{\mu}}x^{\bar{\nu}} + \cdots\,, \tag{3.42}\,{}^{a}_{\mathcal{G}}$$

with symmetric G defined as $G(0,0) = 1$, $G(0,\bar{\alpha}) = 2/3$, and $G(\bar{\alpha},\bar{\beta}) = 1/3$. Since each point $\gamma(x^0)$ of the central geodesic serves as a reference point for an orthogonal RNC expansion, the Riemann tensor must be evaluated at each $\gamma(x^0)$. Thus, unlike only requiring an anchor point for RNC, FNC require geometric information along an interval of γ.

Since in the spatial directions the FNC corresponds to a RNC expansion, we can apply our previous procedure to obtain the domain of validity for the spatial directions. The temporal validity is given by the interval of the considered geodesic and thus the spacetime validity domain describes a "tubular shape" around the geodesic γ. Depending on the local curvature, the diameter of the tube may vary for different x^0. Thus, if we restrict ourselves to the spatial part $g_{\bar{\alpha}\bar{\beta}}$ of the metric (3.42), we find analogous conditions for the domain of validity as for the RNC patch. The crucial difference is that the Riemann tensor now depends on x^0 with $R_{\bar{\alpha}\bar{\beta}\bar{\gamma}\bar{\delta}}(x^0)$ and not only on the anchor point $R_{\alpha\beta\gamma\delta}\big|_p$. Integration over x^0 then leads to a tubular domain of validity for FNC.

Therefore, whenever an application in question requires a large temporal validity, FNC should be used if the temporal validity of a RNC is not sufficient. The aspect to deal with then is that the time dependence of the metric (3.42) may not be polynomial due

to the time dependence of the Riemann tensor. This may obscure the reason for wanting to use normal coordinates in the first place. However, in what follows we construct coordinates that attempt to combine the advantages of FNC and RNC by extending the time dependence of the Riemann tensor in FNC to obtain greater temporal validity than in RNC, with only a polynomial dependence in the metric.

For that matter, we first expand the geodesic γ in $\tau = x^0$ around a point p and then construct the FNC. The vierbein and Riemann components at $\gamma(x^0)$, previously obtained by parallel transport along γ in (3.42), are now found by parallel transport along the Taylor expanded γ and thus they are also expanded in x^0. Using (3.42), we then obtain in temporally expanded FNC,

$$\begin{aligned} x^a(x) &= p^a + e_0^a x^0 + \dot{e}_a^0 (x^0)^2 + x^{\bar{\alpha}}(e_{\bar{\alpha}}^a + \dot{e}_{\bar{\alpha}}^a x^0) + \cdots , \\ g_{\alpha\beta}(x) &= \eta_{\alpha\beta} - G(\alpha,\beta)(R_{\alpha\bar{\mu}\beta\bar{\nu}} + \dot{R}_{\alpha\bar{\mu}\beta\bar{\nu}} x^0) x^{\bar{\mu}} x^{\bar{\nu}} + \cdots , \end{aligned} \tag{3.43}_{\mathcal{G}}^{a}$$

where a dot represents a differentiation w.r.t. τ. We call this procedure an "FNC expansion around a point" and abbreviate it with FNCP.

The domain of validity of this FNCP around p can be determined analogously to the usual FNC. Since cutting the expansion in x^0 introduces an additional mismatch into the full series, this procedure yields another error. Thus, the range of validity of FNCP is a time-limited part of the full tubular range of the FNC. Fixing the total error, which is composed of the temporal expansion and the RNC expansion in the orthogonal direction, results in a tubular region that shrinks in the orthogonal direction for later times and finally to a point at the maximum possible time. Since this also occurs for negative times, the validity of the patch can be described by a point in space that grows in time to a finite spherical region and eventually shrinks back to a point.

If there is no temporal information about the Riemann tensor or the geodesic known, we treat x^0 extensions in the same way as orthogonal $x^{\bar{\alpha}}$ extensions. In this case, FNCP are comparable to RNC in the sense that both represent a way of assigning normal coordinates to a spacetime patch using only geometric information at a single reference point. As might be expected, we then find that the validity of this FNCP is identical to that of a corresponding RNC patch around the same reference point [36].

In summary, normal neighborhoods offer a straightforward way to obtain the propagator. This propagator is valid in various different spacetime regions depending on the specific choice of normal coordinates. With this knowledge we now examine a thin shell background in the next Section.

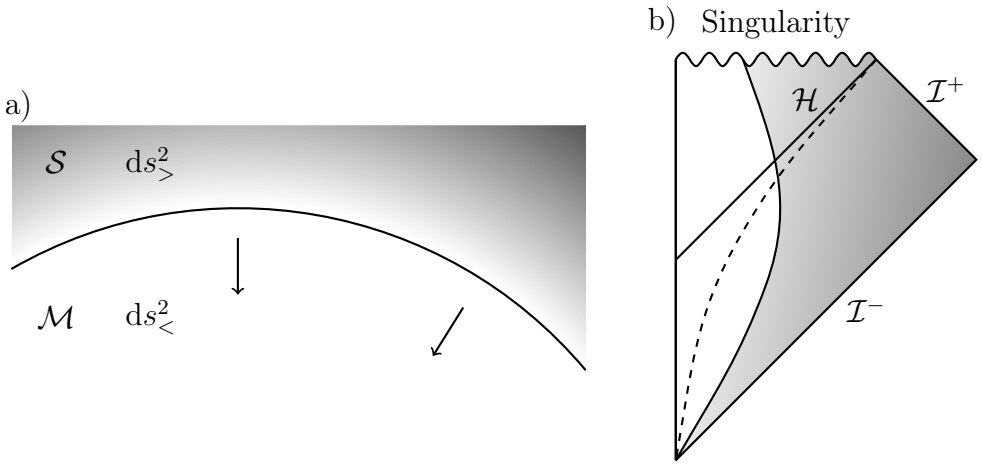

Figure 3.6.: Schematic diagram in a) and the Penrose diagram in b) for the collapsing shell with the Minkowski spacetime inside the shell displayed as a white area. Outside the shell, the Schwarzschild geometry $\mathcal{S}$ is shown in gray with the event horizon $\mathcal{H}$ at $r = r_g$ and the singularity as a wavy line. The dashed line indicates a constant radius with $R > r_g$. The gray shading represents the difference between the background and the Minkowski spacetime, with a smooth transition across the shell enforced by the junction conditions.

3.2. Thin Shell Geometry

In order to study black-hole formation we consider a collapsing thin shell displayed in Fig. 3.6a). As discussed for optical interfaces in Sec. 2.1.2, an infinitely thin shell resembles a good approximation to a more realistic extended and potentially fuzzy shell as long as the wavelength of the considered field configuration is large compared to the thickness of the shell. According to Birkhoff's theorem, a thin shell with mass M and radius $R(\tau)$ has a Minkowski spacetime inside and a Schwarzschild geometry outside, as shown in Fig. 3.6. Thus the line element is given by

$$\begin{aligned} \mathrm{d}s^2_< &= -(\mathrm{d}x^t)^2 + \mathrm{d}r^2 + r^2\mathrm{d}\Omega_2 && r < R\,, \\ \mathrm{d}s^2_> &= -f(r)\,\mathrm{d}t_S^2 + f^{-1}(r)\,\mathrm{d}r^2 + r^2\mathrm{d}\Omega_2 && r > R\,, \end{aligned} \tag{3.44}_{\mathcal{G}}$$

where as before $f(r) = 1 - r_g/r$ and $r_g = 2M$. The Minkowski time coordinate x^t inside the shell is different from t_P and t_S in (3.19) and (3.24) outside the shell.

With the coordinates on the shell $\tilde{x}^{\tilde{\mu}} = (\tau, \theta, \phi)$ the pullback yields the induced metric on the shell,

$$\tilde{g}_{\tilde{\mu}\tilde{\nu}} = \frac{\partial F^\alpha_\circ}{\partial \tilde{x}^{\tilde{\mu}}} \frac{\partial F^\beta_\circ}{\partial \tilde{x}^{\tilde{\nu}}}\, g^\circ_{\alpha\beta} = \mathrm{diag}\left(-1, R^2(\tau), R^2(\tau)\sin^2(\theta)\right), \tag{3.45}_{\mathcal{G}}$$

where $\circ \in \{>, <\}$ indicates whether the metric is induced from outside or inside with

$F^\mu_> = (t_S(\tau), R(\tau), \theta, \phi)$ and $F^\mu_< = (x^t(\tau), R(\tau), \theta, \phi)$, respectively. The first junction condition equates the two expressions and thus ensures the continuity of the line element [56]. This relates the time coordinate inside to the time coordinate in the exterior,

$$\frac{\mathrm{d}t_S}{\mathrm{d}x^t} = \frac{\sqrt{f(R) + \dot{R}^2}}{f(R)\sqrt{1 + \dot{R}^2}}\,, \tag{3.46}_{\mathcal{G}}$$

where $\dot{R} = \mathrm{d}R/\mathrm{d}\tau$.

According to the second junction condition deduced from the Einstein field equations [56], a jump J in the extrinsic curvature K across the shell can only occur if an energy-momentum tensor $S^{\tilde{\mu}}_{\tilde{\nu}}$ is induced at the boundary,

$$\mathrm{J}\left(\tilde{K}^{\tilde{\mu}}_{\tilde{\nu}}\right) - \delta^{\tilde{\mu}}_{\tilde{\nu}}\,\mathrm{J}\left(\tilde{K}\right) = -8\pi S^{\tilde{\mu}}_{\tilde{\nu}}\,. \tag{3.47}_{\mathcal{G}}$$

Unlike most other gravitational collapse models, the shell has a distributional character, and thus there is a jump of K across the shell. The extrinsic curvature is

$$K_{\mu\nu} = \frac{1}{2}\mathcal{L}_n h_{\mu\nu} = h^\alpha_\mu h^\beta_\nu \nabla_\alpha n_\beta\,, \tag{3.48}_{\mathcal{G}}$$

with the tensor $h_{\mu\nu} = g_{\mu\nu} - n_\mu n_\nu$ and the normal vector of the shell $n_\mu \propto \partial_\mu(r - R)$ which obeys $g^{\mu\nu} n_\mu n_\nu = 1$. Solving these equations for the normal vectors yields

$$n^>_\mu(R) = \left(-\dot{R}, \frac{\sqrt{f(R) + \dot{R}^2}}{f(R)}, 0, 0\right), \quad n^<_\mu(R) = \left(-\dot{R}, \sqrt{1 + \dot{R}^2}, 0, 0\right). \tag{3.49}_{\mathcal{G}}$$

As required, the normal vector is orthogonal to the 4-velocity of the shell $u^\mu_> n^>_\mu = 0$ since $u^\mu_> = (\dot{t}_S, \dot{R}, 0, 0)$ and $n^>_\mu = (-\dot{R}, \dot{t}_S, 0, 0)$.

The right-hand side of Eq. (3.47) requires the energy-momentum tensor S of the shell. For S we assume the shell to be made out of a perfect fluid with energy density ρ and pressure p, i.e. $S^{\tilde{\mu}}_{\tilde{\nu}} = \mathrm{diag}(-\rho, p, p)$. The mass of the shell together with the shell trajectory $R(t)$ then uniquely determines the left-hand side of (3.47). Therefore, solving (3.47) for the energy density and pressure yields

$$\rho = \frac{\sqrt{1 + \dot{R}^2} - \sqrt{f(R) + \dot{R}^2}}{4\pi R}\,, \quad p = -\frac{R}{2\dot{R}}\dot{\rho} - \rho\,. \tag{3.50}_{\mathcal{G}}$$

With these equations at hand, we can now consider a particular trajectory $R(\tau)$ and check whether it can be realized in terms of physical matter that fulfills the strong and

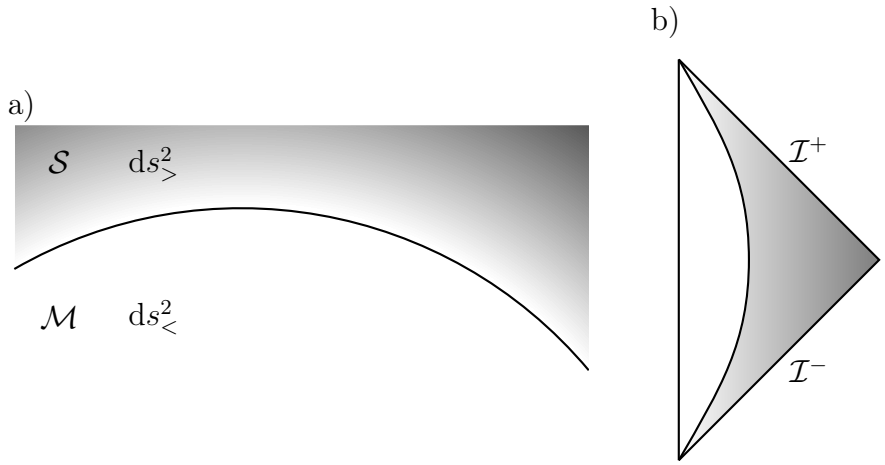

Figure 3.7.: Schematic sketch of a fixed shell with radius $R > r_g$ in a) and the Penrose diagram in b) with the Minkowski spacetime inside (white area) and Schwarzschild geometry $\mathcal{S}$ outside (gray area).

dominant energy condition. First, we study the simplest model of a shell at rest with $\dot{R} = 0$. This spacetime has no horizon for $R > r_g$ as can be seen in its Penrose diagram in Fig. 3.7. Eq. (3.50) in this case reduces to

$$\rho_{\text{fix}} = \frac{1 - \sqrt{f(R)}}{4\pi R}\,, \quad p_{\text{fix}} = \frac{2R\left(1 - \sqrt{f(R)}\right) - r_g}{16\pi\sqrt{f(R)}R^2}\,. \tag{3.51}_{\mathcal{G}}$$

These solutions show that a fixed shell geometry is fully consistent for $R > 25r_g/24$. However, for $R \leq 25r_g/24$ Eq. (3.51) is unphysical, since for these radii the dominant energy condition $\rho \geq |p|$ is violated. This condition guarantees a subluminal flow within the perfect fluid, and thus a shell for $R \leq 25r_g/24$ cannot be stabilized with ordinary matter. For $R \to r_g$ the pressure p_{fix} even diverges, which would require an arbitrarily large force to hold the shell in place.

The second shell we want to consider is one which follows the trajectory of the free-falling Painlevé-Gullstrand observer with velocity (3.25). As can be seen in Eq. (3.22) the coordinate velocity of this shell remains finite at $R = r_g$. Inserting $\dot{R} = -\sqrt{r_g/R}$ in (3.50) results in

$$\rho_{\text{fall}} = \frac{\sqrt{f_+(R)} - 1}{4\pi R}\,, \quad p_{\text{fall}} = \frac{1}{8\pi R}\left(1 + \frac{r_g - 2Rf_+(R)}{2R\sqrt{f_+(R)}}\right), \tag{3.52}_{\mathcal{G}}$$

with $f_+(R) = 1 + r_g/R$. Unlike the fixed shell model, both quantities are regular and finite before and during the horizon crossing at $R = r_g$. Moreover, all energy conditions are satisfied throughout the whole collapse. Since the pressure is always negative $p_{\text{fall}} < 0$,

the shell undergoes a faster collapse compared to a dust shell with $p_{\text{dust}} = 0$. The pressure of the fixed shell, on the other hand, is positive in order to stabilize the shell. For the time being, we will restrict ourselves to the fixed shell and investigate in the following Section the propagation of a scalar field in this geometry.

3.3. Propagation in a Fixed Shell Background

With the fixed shell geometry prepared in the previous Section, we now consider a massless scalar field on this fixed shell background. The action of this field then reads

$$S = -\frac{1}{2}\int_{<} \mathrm{d}^4x\sqrt{-\det(\eta)}\ \eta^{\mu\nu}\partial_\mu\phi\partial_\nu\phi - \frac{1}{2}\int_{>} \mathrm{d}^4x\sqrt{-\det(g_>)}\ g_>^{\mu\nu}\partial_\mu\phi\partial_\nu\phi\,, \qquad (3.53)\,{}^{b}_{\mathcal{H}\,\mathcal{G}}$$

where the subscripts $>$ and $<$ denote the exterior $r \geq R$ or interior $r < R$. To determine the propagator of the scalar field in this theory, we will proceed analogously to the optical case as in Chapter 2. In the following Section, we will begin by using the perturbative approach to describe the curved background as a spacetime dependent interaction term.

3.3.1. Perturbative

As seen before, in the perturbative approach we choose a metric with respect to which we know the propagator and describe the difference to the actual background as an interaction. The choice of the metric has crucial effects on calculations and should therefore be considered carefully. For the fixed shell we choose the Minkowski spacetime inside the shell such that the free propagator of the fields is simply the Minkowski propagator and the exterior spacetime is incorporated with an interaction. Thus the free part of the action is that of a massless scalar field on a Minkowski background, which extends over the entire spacetime:

$$S_0 = -\frac{1}{2}\int_{\mathcal{M}} \mathrm{d}\mu\ \eta^{\mu\nu}\partial_\mu\phi\partial_\nu\phi\,, \qquad (3.54)\,{}^{b}_{\mathcal{H}\,\mathcal{G}}$$

with measure $\mathrm{d}\mu = \mathrm{d}r\,\mathrm{d}\phi\,\mathrm{d}\theta\,r^2\sin(\theta)$. For the interaction part of the action we express the Schwarzschild line element (3.19) in terms of the time inside the shell $x^t(t_S)$ using (3.46) for $\dot{R} = 0$. The exterior line element in these coordinates then reads

$$\mathrm{d}s_>^2 = (g_>)_{\mu\nu}\mathrm{d}x^\mu\mathrm{d}x^\nu = -\frac{f(r)}{f(R)}\,\mathrm{d}t^2 + f^{-1}(r)\,\mathrm{d}r^2 + r^2\mathrm{d}\Omega_2\,. \qquad (3.55)\,{}_{\mathcal{G}}$$

Like before, we treat the difference between the action in the exterior and the Minkowski action in (3.54) as an interaction term with support in the exterior only. The full action

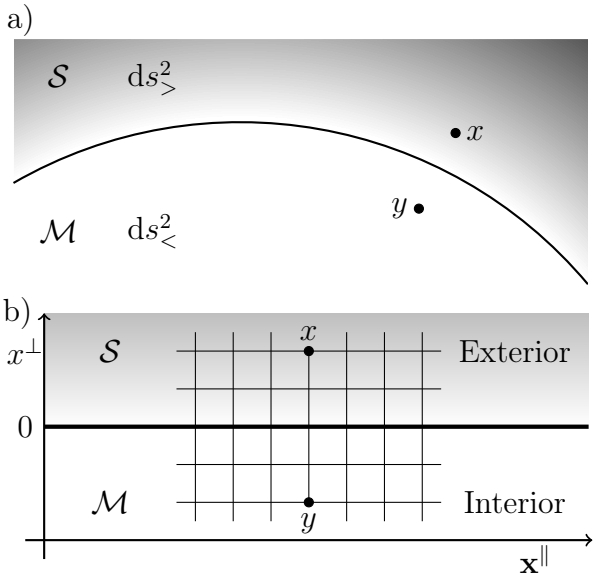

Figure 3.8.: Suspended shell with a Schwarzschild geometry in the exterior and a Minkowski background in the interior is shown in a). Zoomed-in situation with the shell as a interface at $x^\perp = 0$ is displayed in b).

becomes

$$S = \int_{\mathcal{M}} \mathrm{d}\mu \left[-\frac{1}{2}\eta^{\mu\nu}\partial_\mu\phi\partial_\nu\phi + \mathcal{L}_I \right], \tag{3.56}\,{}^{b}_{\mathcal{H}\,\mathcal{G}}$$

where the interaction Lagrangian reads

$$\mathcal{L}_I = -\frac{1}{2}\Theta_{rR}\left[\sqrt{\frac{\det(g_>)}{\det(\eta)}}g^{\mu\nu}_> - \eta^{\mu\nu}\right]\partial_\mu\phi\partial_\nu\phi =: -\frac{1}{2}\Theta_{rR}\, g^{\mu\nu}_I\partial_\mu\phi\partial_\nu\phi\,, \tag{3.57}\,{}^{b}_{\mathcal{H}\,\mathcal{G}}$$

with the auxiliary interaction metric g_I. It should be noted that, as in the optical scenario, g_I is not an ordinary metric, since it does not satisfy Einstein's field equations and does not even transform like a second rank tensor. Analogous to how we performed it for the optical system, we rewrote the action of a free scalar field living on the background of a resting shell (3.53) into the form (3.56).

For the perturbative expansion, we introduce $\lambda = r_g/R \ll 1$ as our smallness parameter. By this condition, we can only study shell radii for which $R \gg r_g$ holds. Later we will work non-perturbatively in λ whereby we can then consider $R \approx r_g$. In addition, we assume that the propagator is evaluated near the shell inside a cubic box with edge length $\ell_0 \ll R$. This makes it advantageous to use the Cartesian coordinates anchored to the shell as depicted in Fig. 3.8,

$$(\mathbf{x}^\parallel, x^\perp) = (r\cos(\phi)\theta, r\sin(\phi)\theta, r - R)\,, \tag{3.58}\,{}^{l}_{\mathcal{H}\,\mathcal{G}}$$

where $(|\mathbf{x}^{\parallel}|, |x^{\perp}|) < (\ell_0/2, \ell_0/2)$, and $\theta < \ell_0/(2R) \ll 1$. Thus, we introduce a second smallness parameter $\bar{x}^{\perp} = x^{\perp}/R$ with $\lambda \ll \bar{x}^{\perp} \ll 1$. Expanding the auxiliary metric in (3.57) up to order $\lambda\bar{x}^{\perp}$, we find

$$g_I(x) \simeq \frac{\lambda}{2}\mathrm{diag}\Big[-\Big(1-2\bar{x}^{\perp}+\frac{3\lambda}{4}+2(\bar{x}^{\perp})^2-3\lambda\bar{x}^{\perp}\Big), \\ -1-2\bar{x}^{\perp}-\frac{\lambda}{4}-2(\bar{x}^{\perp})^2+\lambda\bar{x}^{\perp}, 1+\frac{3\lambda}{4}, 1+\frac{3\lambda}{4}\Big], \tag{3.59}^{lp}_{\mathcal{H}\mathcal{G}}$$

which is valid up to corrections of order λ^2.

With this auxiliary interaction metric the perturbative contribution to the Feynman propagator can then be calculated by expanding the closed-form expression

$$\Delta_{xy} = i\left\langle \mathrm{T}\phi_x\phi_y\, \mathrm{e}^{-\frac{i}{2}\int_> \mathrm{d}\mu_z (g_I^{\mu\nu})_z \partial_{z^\mu}\phi_z \partial_{z^\nu}\phi_z}\right\rangle_{\mathrm{con}}. \tag{3.60}^{blp}_{\mathcal{H}\mathcal{G}}$$

The support of the intermediate integration $\int \mathrm{d}\mu_z$ has to be modified such that the restriction $|(z^{\perp}, \mathbf{z}^{\parallel})| \ll R$ holds. This modification does not influence the result as long as $|x^t - y^t| \ll \ell_0$ and $|(x^{\perp}-y^{\perp}, \mathbf{x}^{\parallel}-\mathbf{y}^{\parallel})| \ll \ell_0$ since then causality implies that $\int \mathrm{d}\mu_y \Delta_{xy} J_y$ is not probing the space outside the box of size ℓ_0. This also restricts the allowed external sources J to be localized inside the box with sufficiently short temporal support.

As in the optical scenario we restrict $y^{\perp} < 0$ and fix the causal order with $x^t > y^t$. Since we chose the interior Minkowski spacetime according to which the field propagate freely in (3.56), we can perform several computational steps analogous to the ones in the optical case. For instance, evaluating (3.60) by following the computation in the complex plane as in (2.40) to (2.44) we find for the reflection propagator,

$$G^{\mathcal{R}}_{xy} = i\int_0^{\infty}\mathrm{d}z^{\perp}\int_k \frac{(g_I^{\mu\nu})_{z^{\perp}} k_\mu k_\nu}{2\,(k_{\perp}+i\epsilon)} e^{-ik_{\perp}(x^{\perp}+y^{\perp})+2iz^{\perp}(k_{\perp}+i\epsilon)}. \tag{3.61}^{b}_{\mathcal{H}\mathcal{G}}$$

In comparison to the optical calculation, the spatial dependence of the interaction metric alters the calculation at this point. The $z^{\perp}$ integration is now also affected by the interaction metric and the derivative in (2.53) now also acts on the transmission coefficient. Since we expanded the interaction metric these changes can be implemented with ease and the reflection propagator becomes

$$G^{\mathcal{R}}_{xy} = \int_k e^{ik_{\perp}(x^{\perp}+y^{\perp})}\frac{\lambda}{8}\left(\frac{\tan^2(\alpha)}{Rk_{\perp}}\Big(i+\frac{1}{Rk_{\perp}}+i\lambda\Big)-\lambda+\frac{3i\lambda}{2Rk_{\perp}}\right), \tag{3.62}^{blp}_{\mathcal{H}\mathcal{G}}$$

where we neglected terms of order $\lambda^3, \lambda/(Rk_{\perp})^3$ and $\lambda^2/(Rk_{\perp})^2$.

Since this propagator can only be trusted for sufficiently large shell radii R we now go

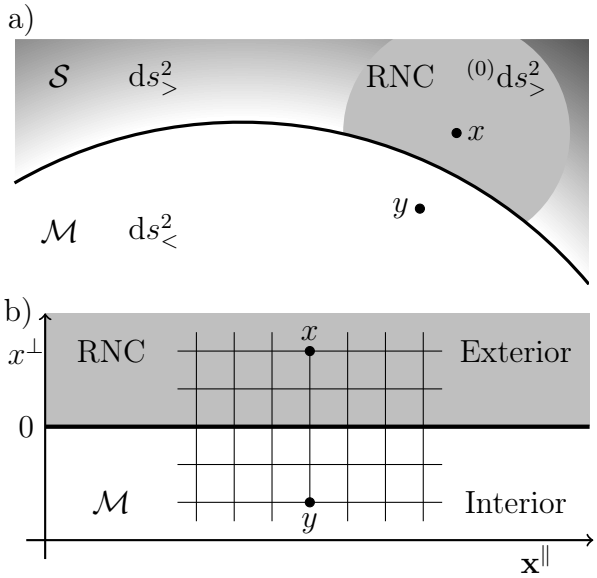

Figure 3.9.: Suspended shell with the leading order patch of a RNC construction anchored at x in the shell's exterior is depicted in a). Zoomed-in situation including a part of the shell at $x^\perp = 0$ and a part both inside and outside is shown in b). Notice the abrupt change in shading symbolizing that the metrics are not matched with junction conditions at the shell surface. This setup is analogous to the optical system in Fig. 2.2.

over to a RNC construction which will allow to remove this constraint. We anchor the RNC patch outside the shell as shown in Fig. 3.9a). At leading order, the RNC metric in RNC coordinates as in Eq. (3.1) is the Minkowski metric. We take a small neighborhood that includes part of the interior and part of the RNC patch. This way, we can treat them as two half-spaces, as shown in Fig. 3.9b). Denoting the leading adiabatic order of the RNC line element with the superscript (0), the line element in this neighborhood can then be written in the coordinates (3.58) as

$$\begin{aligned} \mathrm{d}s^2_< &= -(\mathrm{d}x^t)^2 + (\mathrm{d}x^\perp)^2 + (\mathrm{d}\mathbf{x}^\parallel)^2\,, \\ {}^{(0)}\mathrm{d}s^2_> &= -\frac{f(r_\star)}{f(R)}(\mathrm{d}x^t)^2 + f^{-1}(r_\star)(\mathrm{d}x^\perp)^2 + (\mathrm{d}\mathbf{x}^\parallel)^2\,. \end{aligned} \tag{3.63}^{alp}_{\mathcal{HG}}$$

We can understand this line element as two RNC patches that we simply glued together without applying junction conditions. This way, we describe the underlying smooth manifold with two metrics which are not continuous over the shell at $x^\perp = 0$. An intuitive analogy is provided by a continuously differentiable function approximated by a piecewise constant but noncontinuous function. In our case, we approximate the smooth manifold in a neighborhood with two pieces. As in the analogy, the amount of RNC patches and the distances between the anchor points determine the precision of the approximation. Thus, if we need a more accurate description of the external geometry, we can consider

more RNC patches glued together and/or higher orders of the RNC expansion in (3.1).

This discontinuity in the metric requires a boundary term when we determine the propagator with

$$\Delta_{xy} = i \left\langle \mathrm{T}\phi_x\phi_y \, \mathrm{e}^{-\frac{i}{2}\int_> \mathrm{d}\mu_z (g_I^{\mu\nu})_z \partial_{z^\mu}\phi_z \partial_{z^\nu}\phi_z - \frac{i}{2}\int \mathrm{d}\tilde{\mu}_z \left(\phi_z \, n_<^\mu \partial_{z^\mu}\phi_z - \phi_z \, n_>^\mu \partial_{z^\mu}\phi_z\right)} \right\rangle_{\mathrm{con}} , \tag{3.64}\,{}^{b}_{\mathcal{H}\,\mathcal{G}}$$

where $\mathrm{d}\tilde{\mu}_z$ denotes the (Minkowski) shell surface element together with the outward-pointing shell normal vectors (3.49) for the fixed shell,

$$n_>^\mu(R) = \left(0, \sqrt{g_>^{\perp\perp}}, 0, 0\right) , \quad n_<^\mu(R) = (0,1,0,0) \ . \tag{3.65}\,{}_{\mathcal{G}}$$

Performing the double expansion of the exponential to linear order in λ and g_I, the Feynman propagator reads

$$\begin{aligned} \Delta_{xy} = \Delta_{xy}^\eta - \int \mathrm{d}\mu_z \, (g_I^{\mu\nu})_z \partial_{z^\mu}\Delta_{xz}^\eta \partial_{z^\nu}\Delta_{zy}^\eta \\ - \frac{1}{2}\int \mathrm{d}\tilde{\mu}_z \left[\sqrt{\frac{(g_>^{\perp\perp})_z}{f(R)}} - 1\right] \left[\Delta_{xz}^\eta \partial_{z^\perp}\Delta_{zy}^\eta + \Delta_{zy}^\eta \partial_{z^\perp}\Delta_{xz}^\eta\right] . \end{aligned} \tag{3.66}\,{}^{b\,a\,l\,p}_{\mathcal{H}\,\mathcal{G}}$$

If we were to insert the exterior metric of the shell without RNC expansion as in (3.55), the boundary contribution in the second line would vanish since the metric satisfies the junction conditions and $(g_>^{\perp\perp})_z = f(R)$. However, using the RNC expansion, the line element is (3.63) and thus $(g_>^{\perp\perp})_z = f(r_\star)$, resulting in a boundary term for $r_\star \neq R$.

As the similarity of Fig. 3.9b) to the optical scenario already suggests, due to the constant line element in the exterior the computations in the complex plane can be performed as in the Eqs. (2.40) to (2.45). For the reflection propagator we then obtain

$$G_{xy}^{\mathcal{R}} = -\int_k e^{ik_\perp(x^\perp + y^\perp)} \frac{\lambda \bar{x}_\star}{4} \left[1 + \tan^2(\alpha)\right] . \tag{3.67}\,{}^{a\,l\,p}_{\mathcal{H}\,\mathcal{G}}$$

Here, the smallness parameters are $\lambda = r_g/R \ll 1$ and $\bar{x}_\star = x_\star/R \ll 1$ with $x_\star = r_\star - R$ and the angle of incidence is $\tan^2(\alpha) = \mathbf{k}_\parallel^2/k_\perp^2$. To this result we make the following observations: The reflectance increases as the shell radius approaches r_g. Moreover, the reflection disappears in the limit $r_\star \to R$ showing the smoothness of the underlying background. As in the optical analog case, $\mathcal{R}$ increases with the angle of incidence. The restrictions to the coordinates $x^\perp/R \ll 1$ (and $|\mathbf{x}^\parallel|/R \ll 1$) translates in momentum space to $(Rk_\perp) \gg 1$ (and $(Rk_\parallel) \gg 1$). Thus, this result is valid for sufficiently large frequencies with $\omega_k R > \omega_k r_g \gg 1$ making it complementary to the gray body calculation in the literature [21], which operates in the low-frequency range with $\omega_k r_g \ll 1$.

3.3.2. Nonperturbative Approach

For the non-perturbative approach, we consider the system shown in Fig. 3.9b) and thus the RNC construction with line element (3.63). However, unlike in the previous Section, we now do not assume λ to be small. Then, for the propagators inside $G^<$ and outside $G^>$ the shell, we make the following ansatz,

$$\begin{aligned} G^<_{xy} &= \int_k \left[e^{ik_\perp (x^\perp - y^\perp)} - e^{-ik_\perp (x^\perp + y^\perp)} \mathcal{R}(\mathbf{k}) \right] , \\ G^>_{xy} &= \int_k e^{i(q_\perp x^\perp / \sqrt{f(r_\star)} - k_\perp y^\perp)} \, \mathcal{T}(\mathbf{k}) \, , \end{aligned} \tag{3.68}^{bal}_{\mathcal{HG}}$$

where we have included the factor $1/\sqrt{f(r_\star)}$ in the exponential for later convenience. As in the optical case, the momentum $q_\perp$ is determined by the requirement $\Box_x G^>_{xy} = 0$, and reads

$$q_\perp(\mathbf{k}) = \mathrm{sgn}(k_\perp) \sqrt{\left(\frac{f(R)}{f(r_\star)} - 1 \right) \mathbf{k}_\parallel^2 + \frac{f(R)}{f(r_\star)} k_\perp^2} \, . \tag{3.69}^{bal}_{\mathcal{HG}}$$

As in the optical analogous case with (2.30), the reflection and transmission coefficients $\mathcal{R}$ and $\mathcal{T}$ are determined by the condition that the propagator is continuous and smooth across the interface. Here, this condition reads

$$\lim_{x^\perp \nearrow R} G^<_{xy} = \lim_{x^\perp \searrow R} G^>_{xy} \, , \qquad \lim_{x^\perp \nearrow R} n^\mu_< \nabla^x_\mu G^<_{xy} = \lim_{x^\perp \searrow R} n^\mu_> \nabla^x_\mu G^>_{xy} \, , \tag{3.70}^{b}_{\mathcal{HG}}$$

with the interior and exterior normal vectors (3.65). Substituting the ansatzes for the propagators in (3.68), we obtain equivalently to the optical case

$$\mathcal{R}(\mathbf{k}) = \frac{q_\perp - k_\perp}{k_\perp + q_\perp} \, , \qquad \mathcal{T}(\mathbf{k}) = \frac{2k_\perp}{k_\perp + q_\perp} \, . \tag{3.71}^{bal}_{\mathcal{HG}}$$

As for the optical analogy in Sec. 2.1.2, these coefficients obey charge conservation and recover Eq. (2.34) with $q_\perp$ as defined in (3.69). For an arbitrarily large shell with $R \to \infty$ keeping $r_\star > R$, the system trivializes with $q_\perp \to k_\perp$, $\mathcal{R} \to 0$ and $\mathcal{T} \to 1$. This is the expected result, since the curvature difference between the inner and outer geometries vanishes in this limiting case. In the following Section, we will examine these coefficients in greater depth.

In order to validate this result we expand the reflection coefficient up to second order

in the smallness parameters $\lambda = r_g/R \ll 1$ and $\bar{x}_\star = x_\star/R \ll 1$ with $x_\star = r_\star - R$,

$$\mathcal{R}(\mathbf{k}) = \frac{\lambda \bar{x}_\star}{4}\left[1+\tan^2(\alpha)\right]\left(1-\bar{x}_\star+\lambda\right), \tag{3.72}\,{}^{bal}_{\mathcal{HG}}$$

which is valid up to order $\lambda^3, \lambda\bar{x}_\star^3$ and $\lambda^2\bar{x}_\star^2$. The leading order terms agree with the perturbative result (3.67) solidifying both approaches in curved spacetimes.

The anchor point of the normal neighborhood $x_\star$ in (3.72) must be carefully chosen. If we choose it too close to the shell surface, we will underestimate the reflectance because the curvature in the outer region will not be sufficiently probed. On the other hand, if we choose $x_\star$ too large, we overestimate the reflectance. To find a good choice for $x_\star$, we match the result in (3.72) with the reflection coefficient of the perturbative calculation without RNC construction in (3.62) and solve for the expansion point $x_\star$. In order to shorten the expressions, we perform this matching in a close to normal incidence scenario with $\tan(\alpha) \ll 1$ indicated by the equation superscript s. Solving for the expansion point with this restriction, then yields

$$\bar{x}_\star = \frac{1}{4}(2-\lambda)\lambda + \frac{1}{2}(\lambda-1)\lambda\tan^2(\alpha) + \mathcal{O}\left(\lambda^3, \tan^4(\alpha)\right). \tag{3.73}\,{}^{balps}_{\mathcal{HG}}$$

Inserting this expansion point into the non-perturbative propagators in (3.68) is the best description of the propagation in this background that we provide in this work. In contrast to the perturbative propagators (3.62) and (3.67), the non-perturbative propagator has the advantage that it also captures the case where the shell is close to horizon formation at $R \approx r_g$. Therefore, we use this construction to study the quantum field theoretic properties of the fixed shell background close to horizon formation in the next Sections.

3.3.3. Communication Across the Fixed Shell Surface

With the propagator determined, we can now investigate what happens when we conduct a communication experiment across the surface of the fixed shell with various radii $R \approx r_g$. The continuity condition in (2.34) computed with (3.71) implies that once the reflectance $|\mathcal{R}|^2$ becomes one, the transmittance $\mathrm{Re}(q_\perp)|\mathcal{T}|^2/k_\perp$ vanishes and thus no communication from inside to outside is possible. Therefore, we use the reflectance as a diagnostic tool for a communication experiment close to horizon formation.

Total reflection $|\mathcal{R}|^2 \to 1$ and therefore vanishing transmission $\mathrm{Re}(q_\perp)|\mathcal{T}|^2/k_\perp \to 0$ occurs for $q_\perp \to 0$. Setting $q_\perp = 0$ in (3.69) and solving for λ results in a critical value which marks the point across no communication is possible. This value to leading order

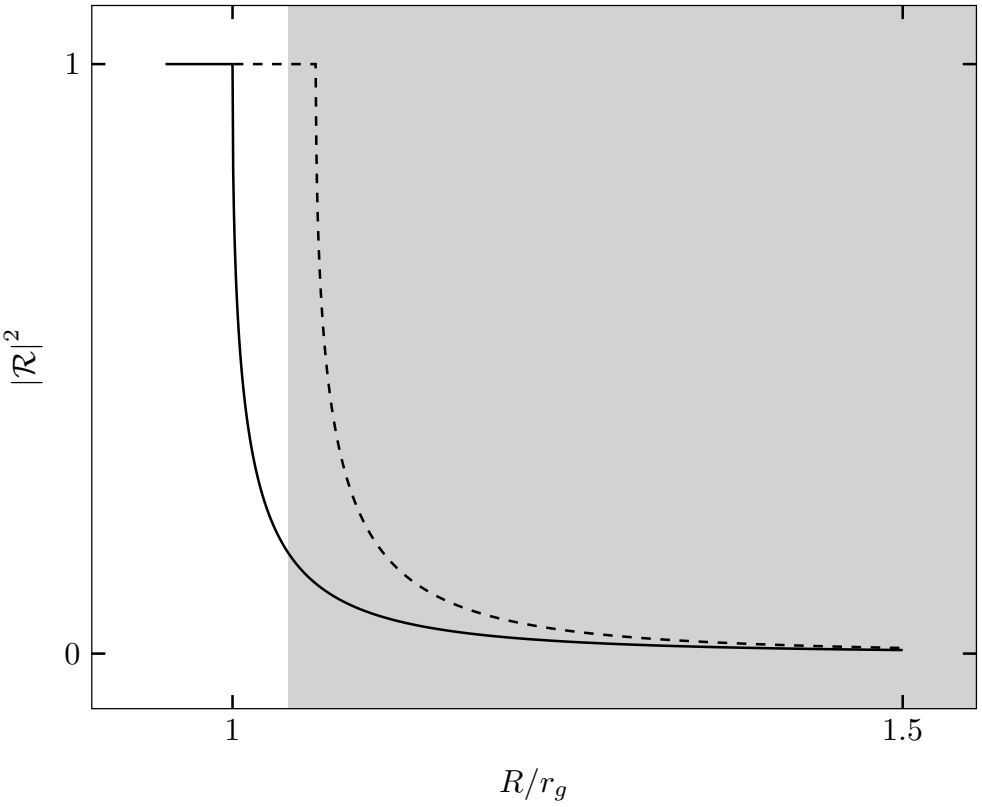

Figure 3.10.: Reflectance from the inside of the shell according to Eq. (3.71) for the suspended shell model with radius R and RNC expansion in the exterior region, anchored at (3.73). The solid line is for a mode at normal incidence, i.e. $\alpha = 0$, for which the reflectance reaches unity at $R/r_g = 1$. The dashed line is for the case $\alpha = \pi/6$, for which total reflection occurs at a larger radius $R/r_g > 1$. In the latter case, this occurs in a range where the fixed shell is made out of matter fulfilling all energy conditions with $R/r_g > 25/24$, indicated by the shaded area.

reads

$$\lambda_c = 1 - \bar{x}_\star \tan^2(\alpha) + \mathcal{O}(\bar{x}_\star^2)\,. \tag{3.74}$$

For the case of normal incidence with $\alpha = 0$, we find $\lambda_c = 1$ and thus that the communication from the inside to the outside breaks down as soon as the shell radius equals r_g and thus coincides with the radius of horizon crossing. The solid line in Fig. 3.10 shows the reflectivity for radii close to r_g and demonstrates that the reflectivity smoothly approaches one. This smoothness suggests no drastic change for observables of a quantum field during the formation of a black-hole, as could be expected from the equivalence principle. For $\alpha \neq 0$ a similar picture results as can be seen by the dashed line in Fig. 3.10 for $\alpha = \pi/6$. The critical point for this angle is in the region where the shell can be fully stabilized physically, i.e. $\lambda_c < 24/25$. As expected, if the incidence on the fixed shell is not in the

radial direction, a particle is less efficient in evading the shell.

Comparing the suspended shell with that of the optical model in Sec. 2, we find that total internal reflection occurs as soon as $\lambda < \lambda_c$. The momentum $q_\perp$ in (3.69) then becomes imaginary, which in turn leads to an exponential damping of the modes outside the shell. In the outlook we will elaborate on this phenomenon and its possible connection to Hawking radiation.

The consideration for $R \leq 25r_g/24$ is of more formal interest since, as discussed in Sec. 3.2, for these radii a fixed shell is unphysical. Thus, the same investigation for a freely collapsing shell as in (3.52), where horizon formation is taking place, is desirable but left for future work. Nonetheless, our simple communication experiment illustrates that the boundary propagator approach is fully compatible with conventional expectations arising from the study of the causal structure of a shell spacetime. We go on in the next Chapter by addressing the second question posed in the introduction

4. Quantum Consistency of Black-Hole Formation

To study quantum effects in a fixed shell background we first introduce the required tools. For that matter, let us consider a quantum system in the state $|\,\Psi\,\rangle$. We assume this system to be isolated and thus including all degrees of freedom relevant to our discussion. In the canonical approach, the system can then be described by the Hamilton operator H and the constraint

$$H|\,\Psi\,\rangle = 0\,. \tag{4.1}_{\mathcal{Q}}$$

This ansatz is reparametrization invariant and is therefore preferred in relativistic contexts where the special role of time - usually enforced in non-relativistic setups - is inappropriate. A prime example for this approach is quantum gravity, where Eq. (4.1) is called Wheeler-DeWitt equation and $|\,\Psi\,\rangle$ describes the entire universe [57]. In our case, this is an elegant way to fully implement the idea of a closed quantum system which includes the measurement process.

4.1. Quantum Field Theory in Curved Spacetimes as an Open Quantum System

In order to perform an experiment, we take some known detector which measures a system. Ideally, this detector has no effect on the system; that is, we choose to make a measurement that is solely dependent on the detector's resolution and not on how the detector influences the system. With this detector, we are able to prepare the state of the detector $|\,\Psi_D\,\rangle$ and of the system $|\,\Psi_S\,\rangle$ separately, and thus the state of the whole setup as a product state $|\,\Psi\,\rangle \propto |\,\Psi_D, \Psi_S\,\rangle$. This implies that there is a part of the Hamilton operator H_D which describes solely the detector and a part H_S which describes solely the system. Additionally there is a part H_{DS} which describes interactions between these two sectors as depicted in Fig. 4.1. Altogether, the Hamilton operator can be written as $H = H_D + H_S + H_{DS}$.

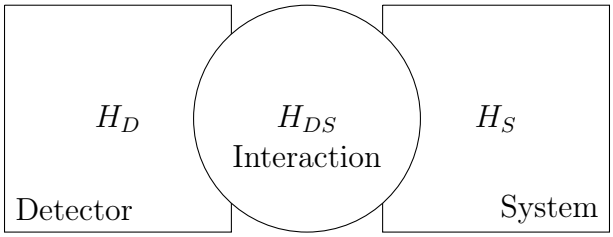

Figure 4.1.: Schematic decomposition of the Hamilton operator in parts which solely describes the system H_S, the detector H_D and the interaction between both sectors H_{DS}. The Hamilton operators describing a subsystem on its own, such as H_D and H_S, are represented by a square, while the Hamilton operator H_{DS} acting on both subsystems, is symbolized by a circle.

Following [37] we take as a detector, a non-relativistic quantum system like an Hydrogen atom and choose an observer such that the detector is at rest in an inertial frame. The degree of freedom we want to describe is a point particle with position $\mathbf{x}$ and momentum $\mathbf{p}$ in phase space $\{\mathbf{x}, \mathbf{p}\}$. The position and momentum operators satisfy the commutation relations $[\mathbf{x}_a, \mathbf{p}_b] = i\delta_{ab}$ and $[\mathbf{x}_a, \mathbf{x}_b] = [\mathbf{p}_a, \mathbf{p}_b] = 0$. Taking the proper time of the observer t, the wave function of the particle $\psi_t(\mathbf{x}) := \langle \mathbf{x} | \Psi_D \rangle_t$ then satisfies the Schrödinger equation

$$i\partial_t \psi_t(\mathbf{x}) = (H_D + H_{DS})\psi_t(\mathbf{x})\,. \tag{4.2}_{\mathcal{Q}}$$

For the system we consider a scalar field Φ with phase space $\{\Phi, \Pi\}$. We here denote the scalar field Φ to distinguish it from the scalar field operator ϕ in the Heisenberg picture, which we employed in the last Chapters. The field operators fulfill the equal time commutation relations $[\Phi_{\mathbf{x}}, \Pi_{\mathbf{y}}] = -i\delta^{(3)}_{\mathbf{xy}}$ and $[\Phi_{\mathbf{x}}, \Phi_{\mathbf{y}}] = [\Pi_{\mathbf{x}}, \Pi_{\mathbf{y}}] = 0$. Analogously to the wave functions in the non-relativistic case we define a wave functional $\Psi_t[\Phi] := \langle\, \Phi \,|\, \Psi_S \,\rangle_t$ using the eigenstates of the operator Φ. With the Schrödinger equation of the detector (4.2) we can then write the Hamilton constraint (4.1) as

$$\left[i\partial_t \psi_t(\mathbf{x})\right] \Psi_t[\Phi] + \psi_t(\mathbf{x})\,(H_S + H_{DS})\,\Psi_t[\Phi] = 0\,, \tag{4.3}_{\mathcal{Q}\mathcal{H}\mathcal{S}}$$

where we used $H_S\psi_t(\mathbf{x}) = H_D\Psi_t[\Phi] = 0$. Integration by parts leads us to the Schrödinger equation for the system

$$i\partial_t \Psi_t[\Phi] = (H_S + H_{DS})\Psi_t[\Phi]\,. \tag{4.4}_{\mathcal{Q}\mathcal{H}\mathcal{S}}$$

Next, we consider a setup in which some of the degrees of freedom of the system are not resolved, but traced out. Thus, we split up the system into one part we call probe P and

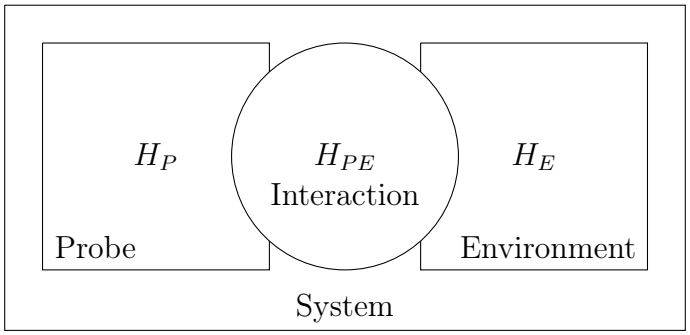

Figure 4.2.: The Hamilton operator of the system H_S is decomposed into parts describing the probe H_P, the environment H_E and the interaction between them H_{PE}.

another part we call environment E and couple them as depicted in Fig. 4.2. We assume the probe and the environment can be prepared separately such that a system state can initially be written as a product state $|\,\Psi_S\,\rangle \propto |\,\Psi_P, \Psi_E\,\rangle$ and the Hamilton operator reads $H_S = H_P + H_E + H_{PE}$. The degrees of freedom in the environment are not coupled to the detector and are thus not resolved directly. Since the probe and the environment interact with each other, tracing out the degrees of freedom in the environment results in a mixed state for the probe such that it becomes an open quantum system [58]. In these scenarios, instead of using the initial state $|\,\Psi_S\,\rangle$ of the system, one has to take the initial density matrix $\rho^S = |\,\Psi_S\,\rangle\langle\,\Psi_S\,|$. The density matrix of the probe ρ^P can then be obtained by tracing out the environment $\rho^P = \mathrm{Tr}_E(\rho^S)$. The dynamical equation for the system's density matrix is determined by the Schrödinger equation (4.4) and reads

$$i\partial_t \rho^S = \left[H_S + H_{DS}, \rho^S\right]. \tag{4.5}$$ $_{\mathcal{QHS}}$

Since the whole system on its own evolves unitary, the solution of this equation can then be expressed with the unitary time-evolution operator $\mathcal{U}_{t_f t_i}$ with $\rho^S_{t_f} = \mathcal{U}_{t_f t_i} \rho^S_{t_i} \mathcal{U}^\dagger_{t_f t_i}$ and $\rho^S_{t_i} := \rho^S$. We can determine the density matrix of the probe at the final time with $\rho^P_{t_f} = \mathrm{Tr}_E[\rho^S_{t_f}]$. Therefore, we can define the probe's time-evolution operator $\mathcal{E}_{t_f t_i}$ as follows

$$\rho^P_{t_f} = \mathrm{Tr}_E[\rho^S_{t_f}] =: \mathcal{E}_{t_f t_i} \rho^P_{t_i}. \tag{4.6}$$ $_{\mathcal{QHS}}$

Here, the time-evolution operator of the probe $\mathcal{E}_{t_f t_i}$ is determined using the time evolution of the whole system including the environment. Typically the exact dynamics of the environment is unknown and techniques are developed to find $\mathcal{E}_{t_f t_i}$ of an open quantum system without requiring this knowledge [59]. Most importantly, even though we might not know the exact evolution of the environment, the operator $\mathcal{E}_{t_f t_i}$ preserves the trace [60].

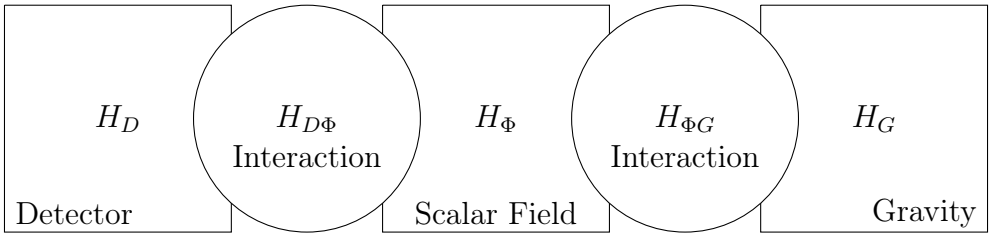

Figure 4.3.: Hamilton operator schematically depicted with a part describing the detector H_D, the scalar field H_Φ and gravity H_G. The detector is chosen sufficiently small and operated for a short time such that gravity only directly couples to the scalar field.

This property follows directly from (4.6) since

$$\mathrm{Tr}_P[\rho^P_{t_f}] = \mathrm{Tr}_P[\mathcal{E}_{t_f t_i}\rho^P_{t_i}] = \mathrm{Tr}_P\big\{\mathrm{Tr}_E[\rho^S_{t_f}]\big\} = \mathrm{Tr}_S[\rho^S_{t_i}] = 1\,, \tag{4.7}$$ $_{\mathcal{QHS}}$

where in the second last step we used the unitary time evolution of the whole system, i.e., $\mathrm{Tr}_S[\rho^S_{t_f}] = \mathrm{Tr}_S[\mathcal{U}_{t_f t_i}\rho^S_{t_i}\mathcal{U}^\dagger_{t_f t_i}] = \mathrm{Tr}_S[\mathcal{U}^\dagger_{t_f t_i}\mathcal{U}_{t_f t_i}\rho^S_{t_i}] = \mathrm{Tr}_S[\rho^S_{t_i}]$. Therefore, we have to make sure that the density matrix of the probe has trace one or equivalently that the states of the probe are normalized. This property of open quantum systems is of major importance in the next Sections in which we discuss the time evolution of a ground state in a system with external potentials, backgrounds and sources.

4.1.1. Dynamical Spacetimes

As we have seen in the previous Section, treating a subsystem of a unitarily evolving quantum system as an open quantum system leads to normalized states at all times. Thus subsystems of a unitarily evolving quantum system inherit the property of unitarity. From the point of view that the whole universe evolves unitarily and that quantum field theory in curved spacetime can be considered as a theory of an open quantum system, naturally unitarity must also hold. Violations of unitarity in quantum field theory in curved spacetimes can therefore lead to a more fundamental theory, such as quantum gravity. If for example the most fundamental theory of everything consists of a quantum gravity theory together with the standard model, then quantum field theory in curved spacetime might emerge by for example performing an effective field theory approach and decoherence. Since these procedures involve integrating out degrees of freedom quantum field theory in curved spacetime describes only a subsystem and thus an open quantum system.

In collaboration with Ka Hei Choi, we generalized the study of understanding quantum field theory in curved spacetimes as open quantum systems to dynamical gravitational backgrounds [38]. Specifically, we used the Schrödinger picture of quantum field theory

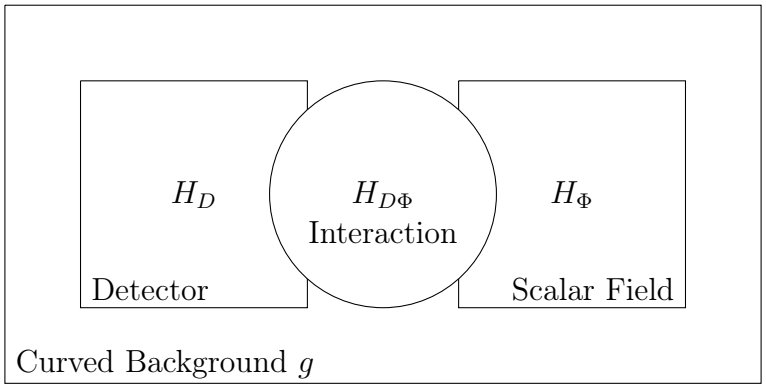

Figure 4.4.: Setup of a detector with Hamilton operator H_D interacting through $H_{D\Phi}$ with a scalar field with Hamilton operator H_Φ set in a curved background with metric g.

to examine the non-unitarity encoded in the VPA for dynamical spacetimes. This Section provides an overview of the main ideas that are intertwined with this project.

For this purpose, we consider a massive scalar field Φ that is coupled to a detector in a system with masses that curve the spacetime. The Hamilton operator of the entire system, which satisfies the Hamilton constraint (4.1), is composed of a gravitational part H_G, the scalar field part H_Φ and for the detector H_D, as shown in Fig. 4.3. As is common for quantum field theory in curved spacetime, we neglect back reaction effects, i.e., we do not take into account how the scalar field Φ perturbs the spacetime itself. As a result, we actually consider quantum fields on a curved background with metric g, as in the framework illustrated in Fig. 4.4.

For technical simplicity and consequent best comprehensibility, we choose a conformally flat Friedmann-Lemaître-Robertson-Walker (FLRW) spacetime in $(d+1)$ dimensions. The line element of these spacetimes in conformal coordinates $(\eta, \mathbf{x})$ is given by,

$$\mathrm{d}s^2 = a_\eta^2 \Big[-\mathrm{d}\eta^2 + \sum_{i=1}^{d} (\mathrm{d}\mathbf{x}^i)^2 \Big] \qquad (4.8)\,{}^{}_{\mathcal{G}}$$

with the scale factor a_η.

As in Sec. 4.1, we introduce the conformal time η via the non-relativistic detector, with which we perform an ADM splitting of the spacetime. In this way, employing the Schrödinger picture of quantum field theory the functional $\Psi_\eta[\Phi]$ encodes the time dependent description of the quantum system and solves the Schrödinger equation (4.4), which now reads [61],

$$i\partial_\eta \Psi_\eta[\Phi] = H_\eta[\Phi]\Psi_\eta[\Phi]\,. \qquad (4.9)\,{}^{b}_{\mathcal{Q}\,\mathcal{H}\,\mathcal{G}}$$

For simplicity, we discard the interaction with the detector such that the Hamilton operator only describes the scalar field Φ with mass m in the curved background,

$$H_\eta[\Phi] := \frac{1}{2}\int_{\Sigma_\eta} \mathrm{d}^d\mathbf{x}\sqrt{g_\eta}\left(\frac{1}{q_\eta}\frac{\delta^2}{\delta\Phi_\mathbf{x}^2} + q_\eta^{ab}\partial_a\Phi_\mathbf{x}\partial_b\Phi_\mathbf{x} + m^2\Phi_\mathbf{x}^2\right), \tag{4.10}\,{}^b_{\mathcal{Q}\,\mathcal{H}\,\mathcal{G}}$$

where q denotes the determinant of the spatial metric on the hypersurface Σ_η. With the help of the annihilation operator C_η and the creation operator $C_\eta^\dagger$ one can write the Hamilton operator as $(C_\eta C_\eta^\dagger + C_\eta^\dagger C_\eta)/2$ [62]. With this definition the ground state wave functional solving $C_\eta\Psi_\eta^0[\Phi] = 0$ and the Schrödinger equation (4.9) is then a Gaussian in Φ and reads [61, 62],

$$\Psi_\eta^0[\Phi] = N_\eta \exp\left\{-\frac{1}{2}\int_{\Sigma_\eta}\mathrm{d}^d\mathbf{x}\,\mathrm{d}^d\mathbf{y}\sqrt{q_\eta}\sqrt{q_\eta}\,\Phi_\mathbf{x}\mathcal{K}^\eta_{\mathbf{xy}}\Phi_\mathbf{y}\right\}, \tag{4.11}\,{}^b_{\mathcal{Q}\,\mathcal{H}\,\mathcal{G}}$$

with the kernel $\mathcal{K}$ and Φ independent prefactor N. In order to relate to the more familiar canonical quantization using the Heisenberg picture of quantum field theory we expand the field operator ϕ of a free scalar field in the Heisenberg picture in terms of the mode functions and the annihilation operator $c_\mathbf{k}$ and creation operator $c_\mathbf{k}^\dagger$ [63–65],

$$\phi_x = \int\frac{\mathrm{d}^d\mathbf{k}}{(2\pi)^d}\left(e^{i\,\mathbf{k}\cdot\mathbf{x}}u_\eta^*(\mathbf{k})c_\mathbf{k} + e^{-i\,\mathbf{k}\cdot\mathbf{x}}u_\eta(\mathbf{k})c_\mathbf{k}^\dagger\right). \tag{4.12}\,{}^b_{\mathcal{Q}\,\mathcal{H}\,\mathcal{G}}$$

Both mode functions solve the Klein-Gordon equation, and picking a complex structure determines the positive and negative frequency modes, so that the vacuum state is defined by $c_\mathbf{k}|0\rangle = 0$. In order to link this decision to the Schrödinger picture, we Fourier transform the kernel $\mathcal{K}^\eta(\mathbf{k}) = \mathrm{FT}\left(\mathcal{K}^\eta_{\mathbf{xy}}\right)$ and derive it from $u_\eta^*(\mathbf{k})$ using [61],

$$\mathcal{K}^\eta(\mathbf{k}) = -\frac{i}{\sqrt{-g}}\frac{\partial_\eta u_\eta^*(\mathbf{k})}{u_\eta^*(\mathbf{k})}. \tag{4.13}\,{}^b_{\mathcal{H}\,\mathcal{G}}$$

The kernel is constructed such that the ground state functional solves the Schrödinger equation (4.9), while the mode functions fulfill the Klein-Gordon equation. In this way, Eq. (4.13) links the two dynamical equations for each respective picture. We connect the two pictures at the level of the kernel and mode functions since, due to the non-applicability of the Stone-von Neumann theorem [66], a connection for quantum field theoretic setups in dynamical spacetimes has yet to be worked out at the level of states and operators [67].

As is common practice in the Heisenberg picture, we relate the modes at $\eta \to \pm\infty$ by a Bogoliubov transformation $u_\eta(\mathbf{k}) = \alpha_\mathbf{k}\,v_\eta(\mathbf{k}) + \beta_\mathbf{k}\,v_\eta^*(\mathbf{k})$ with the Bogoliubov coefficients

α_k and β_k and normalize them with $u_\eta(\mathbf{k})\dot{u}^*_\eta(\mathbf{k}) - u^*_\eta(\mathbf{k})\dot{u}_\eta(\mathbf{k}) = ia_\eta^{1-d}$ [63,68]. Denoting the coordinate volume of the hypersurface Σ with v_Σ, the norm of the ground state functional (4.11) using (4.13) at final time is [38]

$$\|\Psi^0_{\eta_f}\|^2 = \left[\prod_{\mathbf{k}} A_{\eta_f}(\mathbf{k})\right] \exp\left\{ - v_\Sigma \int \frac{\mathrm{d}^d\mathbf{k}}{(2\pi)^d} \ln A_{\eta_f}(\mathbf{k})\right\}, \tag{4.14}$$ $\begin{smallmatrix} b\,t \\ \mathcal{Q}\,\mathcal{H}\,\mathcal{G} \end{smallmatrix}$

with

$$A_{\eta_f}(\mathbf{k}) := \left| \frac{\omega_{\eta_i}(\mathbf{k})}{\omega_{\eta_f}(\mathbf{k})} \left(\frac{a_{\eta_i}}{a_{\eta_f}}\right)^{d-1} \left(1 + 2|\beta_k|^2\right)\right|^{\frac{1}{2}}, \tag{4.15}$$ $\begin{smallmatrix} b \\ \mathcal{Q}\,\mathcal{H}\,\mathcal{G} \end{smallmatrix}$

where the dispersion relation for the scalar field with mass m reads $\omega^2_\eta(\mathbf{k}) = \mathbf{k}^2 + m^2 a^2_\eta$. Notice, to obtain Eq. (4.14) we used a functional which was initially normalized and averaged over time to discard an oscillatory contribution explicitly given in [38] which is nevertheless irrelevant for our discussion here.

The norm of $\Psi^0_{\eta_f}$ in (4.14) deviates from one if $A_{\eta_f}(\mathbf{k}) \neq 1$. This is the case if either $\beta_\mathbf{k} \neq 0$ or $\omega_{\eta_i}(\mathbf{k}) \neq \omega_{\eta_f}(\mathbf{k})$. The Bogoliubov coefficient $\beta_\mathbf{k}$ is measuring the mixing between the positive and negative frequency modes and is connected to the number density $|\beta_\mathbf{k}|^2$ of the particles produced by the background [68]. To better understand the the second scenario of non-unitarity, i.e. if $\omega_{\eta_i}(\mathbf{k}) \neq \omega_{\eta_f}(\mathbf{k})$, we choose for simplicity the well studied example of a FLRW spacetime in $(1+1)$ dimensions with scale factor [68][1]

$$a^2_\eta = A + B\tanh(\rho\eta), \tag{4.16}$$ $\mathcal{G}$

where $A, \rho \in \mathbb{R}^+$, $B \in \mathbb{R}$ and $A > |B|$. In this example, the spacetime is static for $\eta \to \pm\infty$ and has an expanding phase (if $B > 0$) or contracting phase (if $B < 0$) which lasts $1/\rho$. The number density for this spacetime is given by [68]

$$|\beta_\mathbf{k}|^2 = \frac{\sinh^2\left[\frac{\pi}{2\rho}\{\omega_{\eta_f}(\mathbf{k}) - \omega_{\eta_i}(\mathbf{k})\}\right]}{\sinh\left[\frac{\pi}{\rho}\omega_{\eta_i}(\mathbf{k})\right]\sinh\left[\frac{\pi}{\rho}\omega_{\eta_f}(\mathbf{k})\right]}. \tag{4.17}$$ $\begin{smallmatrix} b \\ \mathcal{H}\,\mathcal{G} \end{smallmatrix}$

If the background changes practically instantaneously for the field modes in question, i.e. $\rho \gg \omega_\eta$, the quantity A_{η_f} in (4.15) becomes $A^2_{\eta_f} \to (1 + \omega^2_{\eta_i}/\omega^2_{\eta_f})/2$. For an expanding universe with $B \gg 0$, fields are blue shifted with $\omega_{\eta_i} \ll \omega_{\eta_f}$ and $A^2_{\eta_f} \to 1/2$. In this case, the logarithm in (4.14) changes the sign of the exponent which causes the norm of the final state to diverge due to the infinite volume v_Σ and thus resembling an infrared divergence.

[1] This model can also be conveniently used in optical systems to describe smooth interfaces between two media as discussed in Sec. 2.1.2.

If the universe contracts instead with $B \ll 0$ introducing a red shift with $\omega_{\eta_i} \gg \omega_{\eta_f}$ the logarithm in (4.14) diverges and thus the norm of the final state approaches zero similar to the case close to a black-hole singularity as discussed in [61]. Notice, to obtain this behavior the prefactor N_η in (4.11) was crucial since it delivered the exponential in (4.14)[2]. Before we discuss how to investigate the interpretation of these results we first investigate other choices for the extend of the transition region $1/\rho$.

Namely, if on the other hand the universe evolves adiabatically, its scale factor fulfills $\partial_\eta a_\eta / a_\eta \ll \omega_\eta$. For (4.16) this means $B/(A\rho) \ll \omega_\eta$. In this case there are no particles produced, i.e. $|\beta_{\mathbf{k}}|^2 \to 0$ [68], and the quantity A_{η_f} in (4.15) becomes $A_{\eta_f}^2 \to \omega_{\eta_i}/\omega_{\eta_f}$. The special case $\omega_{\eta_i} = \omega_{\eta_f}$ is obtained for $B = 0$ and resembles a static universe with $\partial_\eta a_\eta = 0$, i.e. a Minkowski spacetime with the norm of the ground state (4.14) remaining one for all times.

In general, for adiabatically evolving spacetimes one can determine the mode function using a WKB ansatz, which in $(d+1)$ spacetime dimensions reads [68],

$$u_\eta(\mathbf{k}) = \frac{1}{\sqrt{2W_\eta(\mathbf{k})\, a_\eta^{d-1}}} \exp\left\{ -i \int_{\eta_i}^{\eta} \mathrm{d}\eta'\, W_{\eta'}(\mathbf{k}) \right\} , \tag{4.18}$$

where $W_\eta(k)$ satisfies the nonlinear equation,

$$W_\eta^2(\mathbf{k}) = \omega_\eta^2(\mathbf{k}) - \frac{1}{2}\left(\frac{\partial_\eta^2 W_\eta(\mathbf{k})}{W_\eta(\mathbf{k})} - \frac{3}{2}\frac{\left[\partial_\eta W_\eta(\mathbf{k})\right]^2}{W_\eta^2(\mathbf{k})} \right) . \tag{4.19}$$

This equation is then solved iteratively up to the desired adiabatic order. For our current discussion it is sufficient to take the zeroth adiabatic order into account and take $W_{\mathbf{k}}(\eta) \approx \omega_{\mathbf{k}}(\eta)$. Since the leading order contribution to the renormalized energy-momentum tensor is given by the fourth adiabatic order, taking the zeroth adiabatic order neglects any particle production and thus $|\beta_{\mathbf{k}}|^2 = 0$ [68]. Furthermore, in the context of computing the propagator in a normal neighborhood in Sec. 3.1, we also performed an adiabatic expansion and restricting to the zeroth order corresponds to taking only the leading order Minkowski contribution in Eq. (3.1) into account. Therefore, the mode function (4.18) simplifies to a plane wave as for a Minkowski spacetime.

The norm of the ground state functional for the leading adiabatic order is then given

[2]Since this property will become important when we will compute vacuum persistence amplitudes, frameworks not taking the normalization factor into account such as in [69] do not cover the full picture.

by (4.14) with

$$A_{\eta_f}(\mathbf{k}) = \left| \frac{\omega_{\eta_i}(\mathbf{k})}{\omega_{\eta_f}(\mathbf{k})} \left(\frac{a_{\eta_i}}{a_{\eta_f}} \right)^{d-1} \right|^{\frac{1}{2}} . \tag{4.20}$$

One immediate observation of this result is that it only depends on the initial conformal time η_i and final conformal time η_f. For $d = 1$ we obtain the same result as before with the explicit example of a $(1 + 1)$ dimensional "tanh universe" with scale factor (4.16). This means, as long as the universe evolves adiabatically, the norm of the ground state functional does not depend on its explicit form of the evolution as required.

If the universe expands, i.e. $a_{\eta_i} < a_{\eta_f}$, no matter by how much, $A_{\eta_f}(\mathbf{k}) < 1$ and thus the norm of the ground state (4.14) diverges due to the infrared divergence as discussed before. For a contracting universe with $a_{\eta_i} > a_{\eta_f}$ we obtain $A_{\eta_f}(\mathbf{k}) > 1$ which causes the norm of the ground state to approach zero. For a universe with scale factor which is the same for the initial and final conformal time $a_{\eta_i} = a_{\eta_f}$, we have $A_{\eta_f}(\mathbf{k}) = 1$ such that the norm of the ground state equals one at the final time. This is the case no matter how the universe evolved between η_i and η_f as long as it evolved adiabatically. This means, the increase of the norm due to an expanding universe can exactly be compensated through a contraction by the same amount. With this quantitative behavior of the ground state functional for adiabatic evolving spacetimes we study renormalization in the next Section.

4.1.2. Renormalization

In order to analyze the change of the norm we first notice that the notion of an instantaneous vacuum state remains intact to the leading adiabatic order. This means the annihilation operator fulfills $C_\eta \Psi^0_\eta[\Phi] = 0$ for all η if and only if the leading adiabatic order is taken into account [38]. This is in accordance with choosing the vacuum state by demanding the adiabatically renormalized energy-momentum tensor to vanish [70]. Therefore to leading adiabatic order, even though its norm can change, an initial instantaneous vacuum state remains an instantaneous vacuum state for all times. In the context of renormalizing the energy-momentum tensor in the Heisenberg picture of quantum field theory in curved spacetimes, up to the third adiabatic order all contributions are discarded due to ultraviolet divergences [68, 71]. This way the fourth adiabatic order and thus particle production is taken into account, while zeroth adiabatic order effects such as the change of the energy density of the ground state are discarded [38].

In curved space-times, point-splitting is a well-known method of renormalization employed in the Heisenberg picture of quantum field theory [72]. One can base the entire analysis on renormalizing the vacuum polarization $\langle \phi^2_x \rangle = \lim_{y \to x} \langle \phi_y \phi_x \rangle$, and derive more

complicated observables like the energy momentum tensor from it. For this purpose, Hadamard states are often used as vacuum states due to their short-distance regularity, covariance and adiabaticity guaranteed for all orders. Performing the expectation value in a Hadamard state, we split it into the following two parts [73–75]

$$\langle \phi_x \phi_y \rangle = \mathfrak{H}_{xy} + \mathfrak{W}_{xy}, \tag{4.21}$$

where $\mathfrak{H}$ is the Hadamard parametrix which includes the short-distance singularities and describes the geometric, state-independent contribution. On the other hand, $\mathfrak{W}$ depends on the state and is regular. The ultraviolet-regular vacuum polarization is then obtained by subtracting the Hadamard parametrix, i.e. $\langle \phi_x^2 \rangle_{\text{ren}} = \lim_{y \to x} [\langle \phi_x \phi_y \rangle - \mathfrak{H}_{xy}]$. In this way, effects such as those at the leading adiabatic order analyzed in Sec. 4.1.1, are discarded. This procedure in the Heisenberg picture cannot be directly translated to the Schrödinger picture due to their a priori in-equivalence in dynamical spacetimes [66]. Therefore, we perform a different approach to discard unphysical effects [38].

To renormalize computations in quantum field theory in curved spacetimes in the Schrödinger picture we adopt the viewpoint of open quantum systems, i.e. we normalize the states whenever it is required [58]. This viewpoint relies on the requirement that at every instant of time a probabilistic interpretation of quantum field theory has to be established. In our case, the probability density is given by $\delta P_t[\Phi] = |\Psi_t[\Phi]|^2$ for a field configuration Φ [61,62,76]. Initially at t_i, we prepare the states with an intact probabilistic interpretation such that the probability density fulfills $\int D\Phi \, \delta P_{t_i}[\Phi] = 1$. At a later time $t_f > t_i$, however, this is not guaranteed and the expanding or contracting universe discussed in Sec. 4.1.1 is an example for which it does not hold since the norm of the ground state (4.14) changes over time. This is the standard renormalization procedure in open quantum systems whenever for example external potentials are used [58].

As explained previously, if the underlying fundamental description of nature is unitary, the subsystems must likewise be unitary. Violations of this underlying principle can be traced back to pathologies in our description, such as introducing tachyonic degrees of freedom [77,78], or to our ignorance of taking essential degrees of freedom only effectively into account. In our case of the scalar field in a FLRW background this is introduced by the semi-classical approximation, i.e. treating the background classical and rigid. In Sec. 4.3, we will go into detail how one can analyze models for pathologies. If pathologies are not the reason, one retains the probabilistic interpretation and thus cures the mistake by not taking all relevant degrees of freedom into account by normalizing the states in

question. In our semi-classical approximation, this amounts to

$$\delta P_t[\Phi] = \frac{|\Psi_t[\Phi]|^2}{\|\Psi_t\|^2} \qquad (4.22)\,{}^{b}_{\mathcal{Q}\,\mathcal{H}\,\mathcal{G}}$$

such that $\int D\Phi\, \delta P_t[\Phi] = 1$. In this way the probabilistic interpretation of quantum field theory is restored such that transition probabilities are between zero and one as required. In curved backgrounds with singularities it might be that the normalization cannot be performed. For instance, as we have seen in Sec. 4.1.1 if we let a universe naively shrink to a point or equivalently approach the singularity in the interior of a black-hole as discussed in [61], the norm of the ground state vanishes and thus (4.22) is ill-defined. This, however, corresponds to the first category of unitarity violation, namely the occurrence of a pathology, here manifested by a singularity. In this case a probabilistic interpretation cannot be restored and an alternative model should be considered. In [38], we go into detail about how vacuum persistence can be used to systematically infer whether a system undergoes non-unitary evolution due to some pathology.

With these tools which allow to identify physical effects, i.e. those who are present after renormalization, we first investigate vacuum effects on an atom in a Minkowski background in the next Section and generalize to curved spacetimes afterwards to study black-hole formation.

4.2. Probing the QED Vacuum with Atoms

4.2.1. Atom Light Interaction

In this Section, we use the more familiar application of atom physics to demonstrate the concepts of open quantum systems. This research was conducted in [37] with Marc Schneider, and it is now summarized here. We investigate the impact of the atom's Coulomb potential on the QED vacuum and the back reaction on the atom. As a result, we determine the effects of the QED vacuum on the atom and this way obtain the Lamb shift as well as an extra dynamical effect.

The dynamical Casimir effect is a well-known dynamical QED effect on the atom. This phenomenon demonstrates how the QED vacuum behaves on an accelerating atom in contrast to one at rest as with the Lamb shift. In [79], the effects of the QED vacuum on an oscillating atom are investigated as shown schematically in Fig. 4.5a). The dynamics caused by the oscillation, opposed to the time-independent Lamb shift, can excite the atom and hence destabilize the ground state. By emitting photons during the relaxation of the atom, the QED vacuum may be indirectly examined.

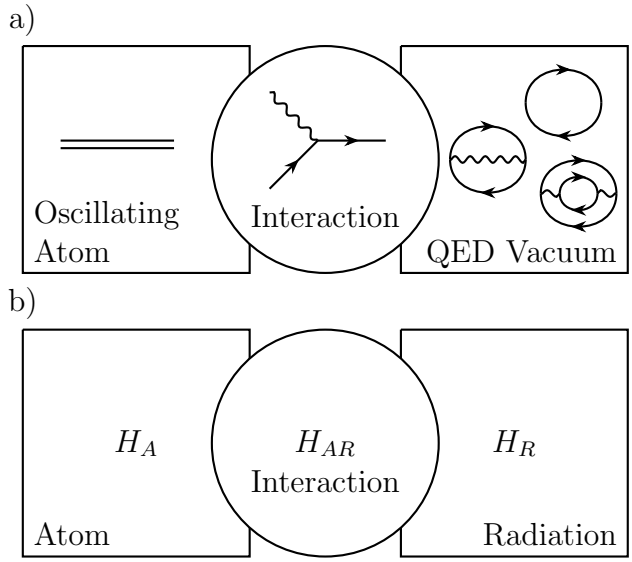

Figure 4.5.: An oscillating atom with an electron that interacts with QED vacuum bubbles leading to the dynamic Casimir effect is shown in a). Schematic depiction in b) of an interaction Hamilton operator H_{AR} that connects the atom's free Hamilton operators H_A to the QED sector with Hamilton operator H_R.

Our case of interest deals with the atom at rest and investigate the dynamical effects of the QED vacuum in the Coulomb potential of the nucleus. In this investigation, we employ the bound-state electron of a hydrogen atom as a detector and examine the QED vacuum that is modified by the presence of the nucleus. As before, we assume that the atom's state $|\,\Psi_A\,\rangle$ and the system's state $|\,\Psi_R\,\rangle$ were initially decoupled, allowing us to express them as a product state $|\,\Psi\,\rangle \propto |\,\Psi_A, \Psi_R\,\rangle$. The Hamilton operator is subsequently decomposed into the different parts as depicted in Fig. 4.5b). Altogether, the Hamilton operator is expressed as $H_{\text{tot}} = H_A + H_R + H_{AR}$.

The wave function $\psi_t(\mathbf{x}) := \langle \mathbf{x}|\Psi_A\rangle_t$ of the bounded electron then solves the Schrödinger equation of the detector (4.2), which explicitly reads

$$i\partial_t \psi_t(\mathbf{x}) = (H_A + H_{AR})\psi_t(\mathbf{x})\,. \tag{4.23}$$

For reference, we first consider the atom without the interaction with the QED vacuum encoded in H_{AR}. In this case, the detector boils down to the quantum mechanical problem of an atom, which may be characterized semi-classically by the nucleus's Coulomb potential. As a result, the Hamilton operator of this detector H_A consists of the electron's kinetic energy plus its potential energy in the coulomb potential and reads in SI units

$$H_A = -\frac{1}{2m_e}\Delta - \frac{e^2}{4\pi\varepsilon_0 r}\,, \tag{4.24}$$

with electron mass m_e, electric charge e and vacuum permittivity ε_0.

The hydrogen wave functions are the eigenstates of the Hamilton operator H_A and are given for the ground state and the first excited state by,

$$\psi_{100}(\mathbf{x}) = \frac{1}{\sqrt{\pi a_0^3}} \exp\left\{-\frac{r}{a_0}\right\}, \qquad \psi_{200}(\mathbf{x}) = \frac{1}{2\sqrt{2\pi a_0^3}} \left(2 - \frac{r}{a_0}\right) \exp\left\{-\frac{r}{2a_0}\right\} . \quad (4.25)$$ $^{be}_{\mathcal{Q}}$

For $H_{AR} = 0$, the states fulfilling the Schrödinger equation (4.26) are then given by $\psi_t^{nlm}(\mathbf{x}) = \exp\{-iE_n t\}\, \psi_{nlm}(\mathbf{x})$ with the eigenvalues E_1 and E_2.

Equipped with the non-relativistic detector of an atom, we now consider the system to be electromagnetic fields. Therefore, the conjugated variables are the vector potential A and the electric field E in the phase space $\{A, E\}$ for which the commutation relations read $\left[A^i_{\mathbf{x}}, E^j_{\mathbf{y}}\right] = -i\delta^{ij}\delta^{(3)}_{\mathbf{xy}}$ and $\left[A^i_{\mathbf{x}}, A^j_{\mathbf{y}}\right] = \left[E^i_{\mathbf{x}}, E^j_{\mathbf{y}}\right] = 0$, using the temporal gauge $A_0 = 0$ [62]. Defining the wave functional $\langle\, \mathbf{A} \,|\, \Psi_R \,\rangle_t = \Psi_t[\mathbf{A}]$ using the eigenstates of the operator $\mathbf{A}$ and performing the same steps as in Sec.4.1 we find analogous to (4.4) the Schrödinger equation for the electromagnetic fields

$$i\partial_t \Psi_t[\mathbf{A}] = (H_R + H_{AR})\Psi_t[\mathbf{A}]\,. \quad (4.26)$$ $^{be}_{\mathcal{Q}\mathcal{H}\mathcal{S}}$

First, let us consider a free electromagnetic field, for which the Hamilton operator reads [62]

$$H_R = \frac{1}{2}\int \mathrm{d}^3\mathbf{x} \left(-\frac{\delta}{\delta \mathbf{A}_{\mathbf{x}}} \cdot \frac{\delta}{\delta \mathbf{A}_{\mathbf{x}}} + \mathbf{B}_{\mathbf{x}} \cdot \mathbf{B}_{\mathbf{x}}\right) , \quad (4.27)$$ $_{\mathcal{Q}\mathcal{H}\mathcal{S}}$

where $\mathbf{B} := \nabla \times \mathbf{A}$ and $\mathbf{E} = i\delta/\delta\mathbf{A}$ has been used. Analogous to the scalar field case introducing the annihilation and creation operator $\mathbf{C}$ and $\mathbf{C}^\dagger$ the Hamilton density operator can be written as $(\mathbf{C}_{\mathbf{x}}\mathbf{C}^\dagger_{\mathbf{x}} + \mathbf{C}^\dagger_{\mathbf{x}}\mathbf{C}_{\mathbf{x}})/2$. The functional of the ground state fulfilling $\mathbf{C}_{\mathbf{x}}\Psi^0_t[\mathbf{A}] = 0$ and solving the free part of the Schrödinger equation (4.4) then becomes

$$\Psi^0_t[\mathbf{A}] = N_t \exp\left\{-\frac{1}{2}\int \mathrm{d}^3\mathbf{x}\, \mathrm{d}^3\mathbf{y}\, \mathbf{B}_{\mathbf{x}} \mathcal{K}_{\mathbf{xy}} \mathbf{B}_{\mathbf{y}}\right\} , \quad (4.28)$$ $_{\mathcal{Q}\mathcal{H}\mathcal{S}}$

where as before $\mathcal{K}$ is the kernel. The $\mathbf{A}$ independent prefactor N_t includes the normalization constant of the state together with the phase $\exp(-i\omega_0 t)$. The energy of the ground state ω_0, diverges in quantum field theory. Normal ordering the Hamilton density operator, it is set to zero such that only differences to the ground state energy are relevant. A first excited state resembling a photon with polarization $\boldsymbol{\varepsilon}$ and wave vector $\mathbf{k}$ can then

be found by applying the field operator onto the ground state,

$$\Psi_t^1[\mathbf{A}] \propto \int \mathrm{d}^3\mathbf{x}\, e^{-i\mathbf{x}\cdot\mathbf{k}}\, \boldsymbol{\varepsilon}\cdot\mathbf{C}_\mathbf{x}^\dagger\, \Psi_t^0[\mathbf{A}]\,. \tag{4.29}$$ $_{\mathcal{QHS}}$

So far we have constructed the wave function and functional of the atom and QED vacuum in their free theories, i.e. neglecting any interaction between the atom and the QED vacuum. As initially assumed their interaction does not modify any of them tremendously such that we can prepare the whole system in a product state. This, however, conveniently allows us to prepare the detector and the QED vacuum as free states and include interactions between them perturbatively. Therefore, we can expand the part of the evolution operator due to the interaction whereas keeping the free parts untouched. This different treatment of these evolution operators automatically introduces the interaction picture of quantum physics.

A state in the interaction picture is characterized by factoring out the time-evolution operator with respect to the free Hamilton operators $\mathcal{H}$ and H. I.e., a Schrödinger state written in terms of an interaction state reads $|\,\Psi_{A|Q}\,\rangle_t^{\mathcal{S}} = U_{A|Q}(t)|\,\Psi_{A|Q}\,\rangle_t^{\mathcal{I}}$, where $\mathcal{S}$ and $\mathcal{I}$ indicate the Schrödinger and interaction picture. Transition amplitudes in this picture are then given by

$$\mathcal{A} = {}_t^{\mathcal{I}}\langle\,\Psi\,|\mathrm{T}\exp\left\{-i\int_{t_0}^{t}\mathrm{d}t' H_{AR}(t')\right\}|\,\Psi\,\rangle_{t_0}^{\mathcal{I}}\,, \tag{4.30}$$ $^{be}_{\mathcal{QHS}}$

where as before T denotes the time ordering of the argument within the exponential.

We can now determine the transition amplitudes of a Hydrogen atom placed in an electromagnetic wave system. First, we consider the process of the atom to begin in its ground state at $t_0 \to -\infty$ together with one photon and end up in an excited atom state and the QED vacuum at $t \to \infty$. The amplitude (4.30) for this process is as follows,

$$\mathcal{A} = {}_\infty^{\mathcal{I}}\langle\,200,0\,|\mathrm{T}\exp\left\{-i\int\mathrm{d}t' H_{AR}(t')\right\}|\,100,1\,\rangle_{-\infty}^{\mathcal{I}}\,. \tag{4.31}$$ $^{ber}_{\mathcal{QHS}}$

Expanding the time evolution operator, the leading contribution to this amplitude is given by the order linear in H_{AR}. In temporal gauge the interaction Hamilton operator reads $H_{AR} = -ie\psi^\dagger\boldsymbol{\gamma}\cdot\mathbf{A}\psi$ with gamma matrices γ^μ and $\psi^\dagger = \bar{\psi}\gamma^0$. Inserting the complete sets $\int\mathcal{D}\mathbf{A}\,|\,\mathbf{A}\,\rangle\langle\,\mathbf{A}\,|$ and $\int\mathrm{d}^3\mathbf{y}|\,\mathbf{y}\,\rangle\langle\,\mathbf{y}\,|$ into Eq. (4.31) results in the transition amplitude

$\mathcal{A} = -\int \mathrm{d}^3\mathbf{x}\, \mathbf{D}_\mathbf{x} \cdot \mathbf{S}_\mathbf{x}$, where

$$\begin{aligned} \mathbf{D}_\mathbf{x} &= e \int \mathrm{d}^3\mathbf{y}\, \bar{\psi}^{2L0}_\mathbf{y} \bar{\psi}_\mathbf{x} \gamma^0 \boldsymbol{\gamma} \psi_\mathbf{x} \psi^{100}_\mathbf{y} \delta(E_1 - E_2 + \omega_\mathbf{k})\,, \\ \mathbf{S}_\mathbf{x} &= \int \mathcal{D}\mathbf{A} \int \mathrm{d}^3\mathbf{k}\, \bar{\Psi}^0[\mathbf{A}] e^{i\mathbf{x}\cdot\mathbf{k}} \mathbf{A}_\mathbf{k} \Psi^1[\mathbf{A}] \end{aligned} \qquad (4.32)\ {}^{berp}_{\mathcal{QHS}}$$

Employing Eq. (4.29) the integral in $\mathbf{A}$ becomes the second moment of a Gaussian integral which can be computed exactly. Furthermore, in the dipole approximation, i.e. the wavelength of the photon is large compared to the extend of the atom, we approximate $\exp(i\,\mathbf{x}\cdot\mathbf{k}) \approx 1$ and thus the entire $\mathbf{x}$ dependence is encoded in $\mathbf{D}_\mathbf{x}$. Evaluating $\mathbf{D}_\mathbf{x}$ further we find the usual proportionality $\mathbf{D}_\mathbf{x} \propto \bar{\psi}^{2L0}_\mathbf{x} \mathbf{x} \psi^{100}_\mathbf{x}$. Inspecting the Hydrogen wave functions (4.25), we see that $\int \mathrm{d}^3\mathbf{x}\, \mathbf{D}_\mathbf{x}$ vanishes for $L = 0$ and is finite for $L = 1$. This is one example of the selection rules which prohibit the optical transition from Ψ^{100} to Ψ^{200} or vice versa. Taking these approximations into account and restricting the atom to two levels the interaction Hamilton operator reduces to the Jaynes-Cummings Hamilton operator.

Within the Hamilton operator of the Hydrogen atom (4.24) we have used the Coulomb potential. This was an effective approach and there is work [80] suggesting that instead of taking the Coulomb potential, one can replace it with the exchange of photons at tree level between the electron and the nucleus. Allowing for loop contributions, the Coulomb potential undergoes quantum corrections, which we determine in the next Section.

4.2.2. Vacuum Induced Spontaneous Excitation

To account for quantum field fluctuations, we consider the QED vacuum as the system. To this end, we introduce fermionic fields describing electrons and positrons with a four-spinor ψ_a. The phase space is spanned by ψ and $\psi^\dagger$, for which the equal time anti-commutation relations are $\{\psi_\mathbf{x}, \psi^\dagger_\mathbf{x}\} = -i\delta^{(3)}_\mathbf{xy}$.

As explained in Sec. 4.1.1 one can base the entire analysis on the renormalized vacuum polarization $\langle \bar{\psi}_x \psi_x \rangle = \lim_{y\to x} \langle \bar{\psi}_y \psi_x \rangle$, and deduce more complicated expectation values such as the one of the current from it. In the case at hand, these observables allow for the retrieval of information about the vacuum state as follows: The conserved current j^μ_x causes an electric field modification that may be measured via back reaction on the vacuum detected with an atomic bound state. This means, vacuum fluctuations cause a local perturbation of the classical Coulomb potential, which affects the bound-state electron. Since the state of the undisturbed atom is known, we can derive information about the vacuum itself by analyzing the difference from the state of the disturbed atom. The conserved fermionic current in QED is $j^\mu = -e\bar{\psi}\gamma^\mu\psi$. Therefore, we may create a cur-

rent operator $\mathcal{O}_j^\mu = -e\gamma^\mu$ acting on $\langle\bar{\psi}\psi\rangle_x$ which connects the current and the vacuum polarization.

The effects of the vacuum on an atom have previously been carefully studied. For instance, Uehling investigated static fields to find the time-independent average contribution that accounted for the later experimentally observed Lamb shift [81]. In their studies, Dirac and Heisenberg [82, 83] formalized the techniques used by employing the density matrix, which is built as the difference between positive and negative frequency modes. Ultraviolet divergences coming from evaluating two fields at the same time were simply discarded. Known today as renormalization, we employ the process of subtracting the Hadamard parametrix as presented in Sec. 4.1.1 to derive the effective potential, which describes time-dependent and time-independent contributions from the QED vacuum. To this end, we briefly summarize the work of Zahn *et. al.* [84–87] here.

Instead of performing the renormalization for a quantum field in a dynamical background like in Sec.4.1.1, we now do it for a quantum field in a Coulomb potential. In terms of operation, we are exchanging a gravitational background for an electromagnetic potential, both of which are unresolved and hence external. The features of quantum fields in external potentials frequently overlap with those of curved spacetimes, as indicated by the striking resemblance of the Schwinger effect and Hawking radiation [88, 89].

The propagator, like before, is the main focus of our investigation into vacuum effects. However, previously, we were only interested in the vacuum effects of scalar fields, and hence only in their propagator, whereas here we are studying the QED vacuum, and so the propagator of the fermion field ψ is required. Fortunately, the Klein-Gordon operator can be decomposed into a contraction of the Dirac operator and its adjoint, allowing for the derivation of the fermionic propagator Δ^ψ from its scalar counterpart Δ [90],

$$\Delta^\psi_{xy} := i\langle \mathrm{T}\psi_x\bar{\psi}_y\rangle = (i\gamma^\mu D_\mu + m)\,\Delta_{xy}\,, \tag{4.33}_{\mathcal{QHS}}$$

where $D_\mu = \partial_\mu - ieA_\mu$. Propagators in the external Coulomb potential are studied for a scalar field and a spinor field, respectively, in [91] and [92]. The mode functions in the Coulomb potential are derived, for example, in [93–97].

As discussed in Sec. 4.1.2, the bare expression of the vacuum polarization has ultraviolet divergences which are discarded by subtracting the Hadamard parametrix such that one ends up with the renormalized vacuum polarization $\langle\bar{\psi}_x\psi_x\rangle_{\mathrm{ren}}$. This quantity incorporates how the QED vacuum creates electron positron pairs with which the renormalized expectation value of the current density can be obtained and reads [87]

$$\langle j^\mu_x\rangle_{\mathrm{ren}} = \frac{e}{8\pi^2}\mathfrak{W}_{xx}\gamma^\mu\,, \tag{4.34}_{\mathcal{QHS}}$$

where $\mathfrak{W}_{xx}$ can be derived iteratively employing the Hadamard coefficients $W^{(n)}$. Following this modern approach, [85] showed that the result matches with the original result found by Uehling [81] for static fields and Serber [98] for dynamical fields.

Using the notation of [98], the renormalized expectation value of the current density caused by an external current J is (for $m \equiv 1$)

$$\langle j_x^\mu \rangle_{\text{ren}} = \int \mathrm{d}^4 y \int_0^{\frac{\pi}{2}} \mathrm{d}\varpi \cos^3(\varpi) \Lambda(x-y;\varpi) \Box\Box J_y^\mu \,, \tag{4.35}$$

with the integration kernel given by [85, 98]

$$\Lambda(x;\varpi) = \frac{\alpha}{32\pi^5} \int \frac{\mathrm{d}^4 k}{k^4} e^{-ikx} \ln\left[1 - \frac{k^2}{2}\cos(\varpi)\right] . \tag{4.36}$$

Λ has two contributions, one static denoted by Λ_1,

$$\Lambda_1(\mathfrak{r};\varpi) = -\frac{\alpha}{16\pi^2 \mathfrak{r}} \cos^2(\varpi) \int_1^\infty \frac{\mathrm{d}K}{K^3} e^{-2K\mathfrak{r}\sec(\varpi)} \,, \tag{4.37}$$

and one dynamic denoted by Λ_2 which reads [85, 98]

$$\Lambda_2(\tau;\varpi) = \frac{\alpha}{8\pi^2 \tau} \cos(\varpi) \int_1^\infty \frac{\mathrm{d}K}{K^2} \mathrm{J}_1(2K\tau\sec(\varpi)) \,, \tag{4.38}$$

where $\mathfrak{t} = |t-t'|/\nu_{\text{Compton}}$, $\tau = \sqrt{|\mathfrak{r}^2 - \mathfrak{t}^2|}$, $\mathfrak{r} = |r-r'|/\lambda_{\text{Compton}}$, $k_0 = K\sinh(\varphi)$ and $k = K\cosh(\varphi)$ as in [98].

The time-independent contribution yields the Uehling potential $U(\mathfrak{r})$ which in a more common form reads [63, 81, 98, 99]

$$\int \mathrm{d}^3\mathbf{y} \frac{\pi}{e^2\alpha} U(\mathfrak{r}) \Delta J_{\mathbf{y}}^\mu \,. \tag{4.39}$$

The Uehling potential is a quantum correction of the classical Coulomb potential with $\lim_{\hbar\to 0} U(\mathfrak{r}) = 0$. Combining the Coulomb potential in (4.24) with the Uehling potential changes the resulting hydrogen eigenfunctions and eigenvalues. Because this is a small correction, we use perturbation theory to examine how the eigenvalues of the hydrogen states (4.25) change in the presence of the Uehling potential,

$$\Delta E_{nl} = \int \mathrm{d}^3\mathbf{x}\, U(\mathfrak{r}) \left|\psi_{nl0}(\mathbf{x})\right|^2 . \tag{4.40}$$

This contribution, called Lamb shift, shifts the eigenvalue by $E_n - \Delta E_{nl}$ such that the hydrogen wave functions are modified and read $\exp\{-i(E_n - \Delta E_{nl})t\}\psi_{nl0}(\mathbf{x})$. Eq. (4.40)

produces a magnitude of $|\Delta E_{ln}/E_n| \lessapprox 10^{-8}$ for the ground state and the first excited state of a hydrogen atom (4.25). By precisely measuring these energy levels in an experiment, the effect of the QED vacuum on the atom could be determined [100].

The time-dependent contribution (4.38), on the other hand, introduces dynamic effects on the electron's bound states. Performing the K integration yields

$$\Lambda_2(x) = \frac{\alpha}{8\pi^2}\left[\frac{1}{2} - \gamma + \frac{x^2}{4}\,{}_2F_3\left(\begin{matrix}1,\,1\\2,\,2,\,3\end{matrix}\middle|\,-x^2\right) - \ln(x)\right], \tag{4.41}\,{}^{p}_{\mathcal{Q}\mathcal{H}\mathcal{S}}$$

where γ is the Euler-Mascheroni constant and $x := \tau\sec(\varpi)$. The logarithm in (4.41) dominates the small τ behavior, whereas the hypergeometric term controls the intermediate part, which is the most relevant one for our investigation on atomic scales. For large radii or after long times, the Serber potential goes to zero, i.e. $\lim_{x\to\infty}\Lambda_2(x) = 0$.

Similar to the Uehling potential in (4.39), we define the Serber potential S with

$$\int \mathrm{d}^4y\, S(\tau)\Box\Box J^\mu_y\,. \tag{4.42}\,{}^{p}_{\mathcal{Q}\mathcal{H}\mathcal{S}}$$

Performing the integration over ϖ the closed form of the Serber potential reads

$$S(\tau) = \frac{\alpha}{8\pi^2}\left[\frac{\sqrt{\pi}}{4}\mathrm{G}^{2,2}_{3,5}\left(\begin{matrix}1,1;5/2\\1,2;-1,0,0\end{matrix}\middle|\,\tau^2\right) - \frac{2\ln(\tau)}{3} - \frac{2}{3}\left(\frac{1}{3} + \gamma - \ln(2)\right)\right], \tag{4.43}\,{}^{p}_{\mathcal{Q}\mathcal{H}\mathcal{S}}$$

with G the Meijer G-function. For small $\tau \ll 1$, the Serber potential is expanded as $S(\tau) = -\alpha\ln(\tau)/12\pi^2 + \mathcal{O}(\tau^0)$ and thus diverges logarithmically at zero. Asymptotically, for $\tau \gg 1$, the Serber potential is given by a damped oscillation, that is $\lim_{\tau\to\infty} S(\tau) \propto [\cos(2\tau)]/\tau^3 + \mathcal{O}(1/\tau^4)$ as seen in Fig. 4.6.

As before with the Uehling potential leading to the Lamb shift, we now investigate the effect of the Serber potential on the bound state electron. In this analysis, we concentrate on the influence of quantum fluctuations on the bound state electron while neglecting the effect on the Coulomb potential itself. Because we have a time-dependent potential, energy conservation is not enforced, causing tensions owing to the assumption of an eternal Coulomb field. In this regard, because we are using the electron in the bound state as a detector for QED processes, we must consider the system to be open. To remove this tension, the process has to include the dynamical resolution of the Coulomb potential[3], its quantum corrections, and the proton to establish a closed system. The similarities with particle production by black-holes are intriguing and worth considering [37]. Because protons are subject to quantum chromodynamics, they are not included in the QED

[3]Despite recent research in this direction such as in [80], resolving the Coulomb potential in terms of fundamental degrees of freedom has not been achieved yet.

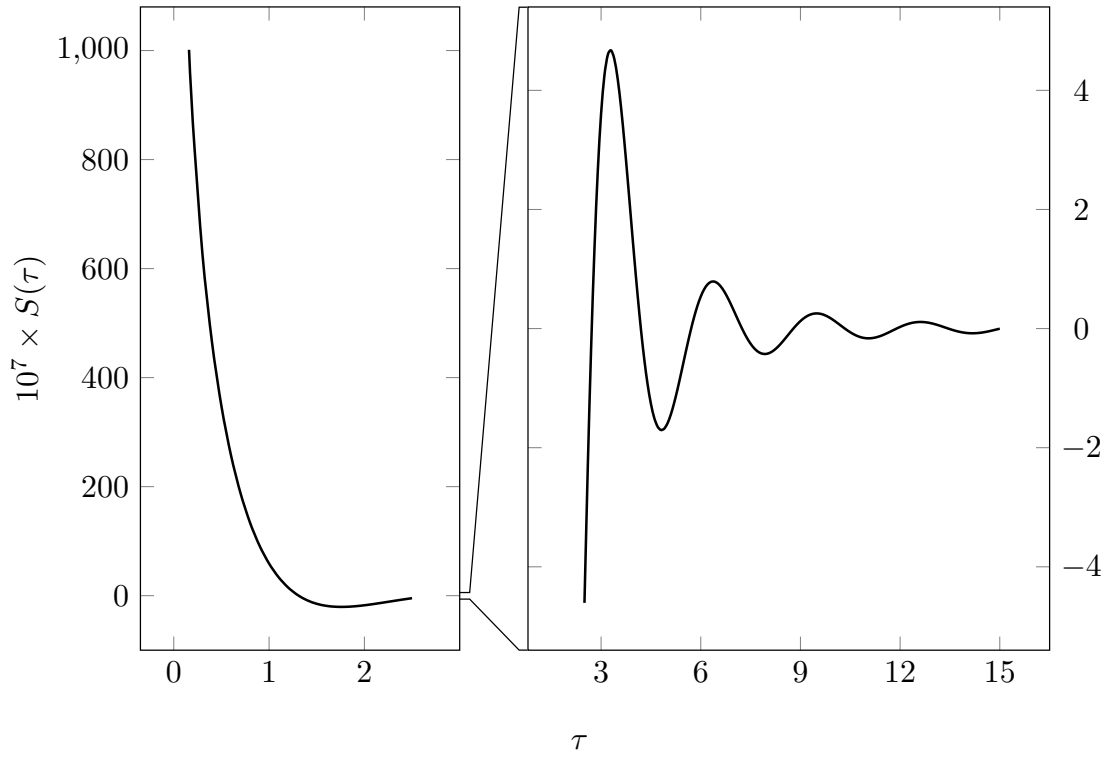

Figure 4.6.: The left panel shows the Serber potential $S(\tau)$ for $\tau \in [0.16, 2.5]$ where the logarithmic divergence is dominant and oscillatory contributions are highly suppressed. For the interval $\tau \in [2.5, 15]$ in the right panel the Meijer G-function becomes relevant such that the potential performs damped oscillations.

spectrum. In the case of positronium, a full QED process may be employed to characterize the bound state, but because this configuration is unstable, it may be inappropriate for analyzing small alterations produced by vacuum fluctuations. Only in a closed system with a microscopic description of the Coulomb potential can a comprehensive account of the energy fluxes be obtained. The back reaction is described as a scattering process in this model, with the elements constituting the classical potential such that energy conservation is assured through unitarity.

At the moment, however, we are operating with the semi-classical approximation, and hence in an open quantum system. We employ the Rayleigh-Schrödinger perturbation theory for time-dependent potentials to investigate the effect of the Serber potential on atomic states. In this context, we find in particular an instability of the ground state using Fermi's golden rule,

$$P^{(1)}(t) = \left| i \int_{t_0}^{t} \mathrm{d}\xi e^{i(E_n - E_i)\xi} \langle 200|S(\xi)|100\rangle \right|^2 \neq 0\,. \tag{4.44}$$

As a result, the Serber potential allows that the electron trapped in the 1S orbital can

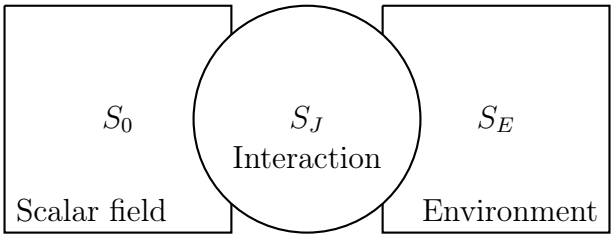

Figure 4.7.: Schematic depiction of the action composed of a scalar field part S_0 and an external source with action S_E and the coupling between them with S_J.

transition to the 2S orbital. In this regard, we can observe that the hydrogen ground state is not a QED ground state. As a quantitative example, we take the typical time for an atomic transition with $t \in [0, 10^{-17}]$ and $r \in [10^{-3}\, a_0, 10\, a_0]$, resulting in a transition probability of order $\mathcal{O}(10^{-20})$. The Serber potential makes no contribution to the selection criteria outlined in Sec. 4.2.1, since the probability of any $\psi_{nlm}(r)$ being excited to $\psi_{nl+1m}(r)$ by the Serber effect is zero. In a technical sense, the electron of a hydrogen atom couples to an electron-positron vacuum bubble through two photons. Because this 2-photon coupling cannot alter the electron's angular momentum by one, the Serber contribution does not follow the typical selection rules, but instead concerns transitions that occur, for example, in 2-photon excitation.

Through spontaneous excitation of the atom ground state, non-trivial vacuum effects caused by the Coulomb potential may be detected in this manner. As a result, the atom may be employed as a detector for QED vacuum effects. When an atom is placed in a curved spacetime, there is an extra source of vacuum induced spontaneous excitation of the atom, as we shall see in the next Section.

4.3. Vacuum Persistence in Curved Spacetimes

As described in the introduction, we are interested in the persistence of the vacuum of a probe field in a curved background. This persistence is given by the amplitude $\langle\, 0_f \,|\, 0_i \,\rangle$, relating the initial vacuum state $|\, 0_i \,\rangle$ with the final vacuum state $|\, 0_f \,\rangle$. As in the previous Section we could take the QED vacuum and analyze spontaneous excitation of an atom in a curved spacetime. However, to concentrate on the phenomena introduced by the curved background, we choose the most simple probe field, a massless, real scalar field ϕ and as a detector an external source J, as shown in Fig. 4.7. Since we do not know the dynamics of an external source and thus have no information about its kinetic action S_E, we treat it as an environment. We place this arrangement in a Minkowski spacetime $(\mathcal{M}, \eta)$ and thus the action is given by $S = S_0 + S_J$,

$$S = -\frac{1}{2}\int_{\mathcal{M}} \mathrm{d}\mu_x \left(\eta^{\mu\nu}\partial_\mu\phi\partial_\nu\phi + 2\phi J\right) =: \frac{1}{2}\int_{\mathcal{M}} \mathrm{d}\mu_x\, \mathrm{d}\mu_y \left(\phi_x K_{xy}\phi_y - 2\phi_x J_x \delta^{(4)}_{xy}\right), \qquad (4.45)_{\mathcal{HS}}$$

with $K_{xy} := \Box_x \delta^{(4)}_{xy}$.

To calculate the vacuum persistence amplitude, there is a plethora of methods. Here, we use the approach relying on the path integral quantization of a free scalar field ϕ with an external source J and consider the generating functional [68, 101, 102],

$$\langle\, 0_f \,|\, 0_i \,\rangle_J = \int_{\phi_i}^{\phi_f} \mathcal{D}\phi\, e^{iS[\phi,J]}\,. \qquad (4.46)_{\mathcal{QHS}}$$

The boundaries of the path integral can conveniently be rewritten as $\langle\, 0_f \,|\, \phi_{t_f} \,\rangle$ and $\langle\, \phi_{t_i} \,|\, 0_i \,\rangle$ due to the orthonormality of the states. Since the initial and final sates are vacuum states in a free theory, these amplitudes can be expressed as Gaussian functionals in ϕ. These functionals are then conveniently reformulated as an $i\epsilon$ prescription in (4.46) with K_{xy} replaced by $K^\epsilon_{xy} = (\Box_x - i\epsilon)\,\delta^{(4)}_{xy}$ with the limit $\epsilon \to 0$ understood [102]. Adopting this procedure and performing a substitution $\phi \to \bar{\phi}$ with $\bar{\phi}_x = \int \mathrm{d}\mu_y \sqrt{K^\epsilon_{xy}}\phi_y$ as in [68] or $\bar{\phi}_x = \phi_x + \int \mathrm{d}\mu_y (K^\epsilon)^{-1}_{xy} J_y$ the generating functional becomes [103]

$$\langle\, 0_f \,|\, 0_i \,\rangle_J \propto \sqrt{\det(\Delta)}\, \exp\left\{\frac{i}{2}\int \mathrm{d}\mu_x\, \mathrm{d}\mu_y J_x \Delta_{xy} J_y\right\}, \qquad (4.47)_{\mathcal{QHS}}$$

where we performed the $\int \mathcal{D}\bar{\phi}$ integral using $(\Box_x - i\epsilon)\,(K^\varepsilon)^{-1}_{xy} = \delta^{(4)}_{xy}$ and the Feynman propagator fulfilling $\Delta_{xy} = (K^\varepsilon)^{-1}_{xy}$.

In Sec. 4.1.2, we argued that in the context of open quantum systems, the states of a subsystem have to be properly normalized. Since we are interested in whether the vacuum changes due to the presence of the external source, we normalize the total amplitude by dividing the expression without sources $\langle\, 0_f \,|\, 0_i \,\rangle^0_J := \langle\, 0_f \,|\, 0_i \,\rangle_J / \langle\, 0_f \,|\, 0_i \,\rangle_0$. In this way, the normalization of the vacuum states is guaranteed and the contributions not coming from the source are taken out such that in (4.47) only the exponential depending on the external source remains. Historically [104], this is the first setup in which the VPA was discussed, and from which the following expression of the VPA was derived with the Schwinger action principle,

$$\langle\, 0_f \,|\, 0_i \,\rangle^0_J := \frac{\langle\, 0_f \,|\, 0_i \,\rangle_J}{\langle\, 0_f \,|\, 0_i \,\rangle_0} = \exp\left\{\frac{i}{2}\int \mathrm{d}\mu_x\, \mathrm{d}\mu_y J_x \Delta_{xy} J_y\right\} =: e^{iW_J}\,. \qquad (4.48)_{\mathcal{QHS}}$$

For real W_J, the VPA is just a phase and the vacuum is stable. The probability for the

vacuum state to be persistent is affected by the imaginary part [104],

$$\left|\langle\, 0_f \,|\, 0_i \,\rangle_J^0\right|^2 = e^{-2\mathrm{Im}(W_J)} = \exp\left\{-\int \frac{\mathrm{d}^3k}{(2\pi)^3 2\omega_k}\Big|\int \mathrm{d}\mu_x\, e^{-ikx} J_x\Big|^2_{k_0=\omega_k}\right\}, \tag{4.49}_{\mathcal{QHS}}$$

where we assumed the external source to be real, i.e. $\mathrm{Im}(J) = 0$.

It is common practice to use the VPA to analyze the unitarity of quantum systems [105, 106]. There is also a plethora of similar techniques examining the same question which are connected to the VPA. For instance, a suitable way to investigate whether unitarity is broken is to check the optical theorem in the context of scattering theory. If the imaginary part of a forward scattering amplitude is positive, for example in considering tachyonic degrees of freedom, the optical theorem does not hold and the quantum system evolves non-unitarily. This has been used extensively to shrink the parameter space in model building such as in [77, 78] for effective field theories and in [107] for inflation models.

For a quantum system evolving unitarily, the probabilistic interpretation is guaranteed at all times, i.e., the transition probabilities are bounded by zero and one. Therefore, in a properly functioning quantum system the VPA satisfies the condition,

$$|\langle 0_f|0_i\rangle_J^0|^2 \leq 1\,. \tag{4.50}_{\mathcal{QHS}}$$

In general, the external source J radiates and thus fills the system with particles that were not present before the source was turned on. This decreases the transition probability for the system to remain in the initial vacuum state, which is therefore a measure of particle production. The transition probability (4.49) satisfies (4.50) as we will show for specific external sources in the next Section. The inclusion of other contributions such as a curved background may potentially yield $|\langle 0_f|0_i\rangle_J^0|^2 > 1$, which would reflect an inconsistency that violates the probabilistic interpretation of quantum field theory [105, 106]. In this way, the determination of the VPA is an important consistency check for quantum field theory in curved spacetimes which we will apply for black-hole formation in Sec. 4.3.2 using the external sources which we characterize in a Minkowski background in the next Section.

4.3.1. Construction of Privileged External Sources

In order to study the VPA in the context of black-hole formation and thus for a thin shell geometry, we first analyze the external sources that we intend to use in a Minkowski

background. Of primary interest to us will be a temporally smeared-out point source

$$J_x^s = \frac{1}{\sqrt{2\pi\sigma^2}} \exp\left\{\frac{-(t-t_0)^2}{2\sigma^2}\right\} \delta_{\mathbf{x}}^{(3)}\,, \tag{4.51}_{\mathcal{QHS}}$$

with standard deviation σ. The VPA in Minkowski (4.49) using such a source then becomes

$$\left|\langle\, 0_+ \,|\, 0_- \,\rangle_{J^s}^0\right|^2 = \exp\left\{-\int \frac{\mathrm{d}^3k}{(2\pi)^3 2\omega_k 2\pi} e^{-\omega_k^2\sigma^2}\right\} = \exp\left\{-\frac{1}{2(2\pi)^3\sigma^2}\right\}. \tag{4.52}_{\mathcal{QHS}}$$

Switching the source on and off adiabatically with $\sigma \to \infty$ the transition amplitude is one and therefore the vacuum state remains in the initial state. Notice, the result does not depend on t_0, i.e. we loose all information when the sources are switched on. Thus, the vacuum decay does not depend on absolute time but only on relative times as required by the Poincaré symmetry of the Minkowski spacetime.

The limit $\sigma \to 0$ describes a source which is turned on and off again in an instant and $J_x^s \to \delta_x^{(4)}$. The VPA (4.52) jumps to zero in an arbitrary short amount of time indicating a pathology. This pathology is caused by an external source which could not be created by reasonable physics since to manufacture a $\delta_x^{(4)}$ source one would require modes with arbitrary high energy and thus exceeding the Plank energy scale. Those modes are not part of the standard model and therefore we cannot expect a $\delta_x^{(4)}$ source to yield something meaningful.

In the intermediate region in which σ is finite and non-zero the VPA returns a probability $0 < p < 1$. In summary, the VPA of any point source reduced in time in Minkowski satisfies the bound (4.50), and thus we can use it for curved backgrounds in the following section.

A more involved source is composed of an emitter and an absorber source $J = J^e + J^a$. We switch on the emitter source which radiates away particles until it is switched off again. Afterwards particles can be absorbed by the source J^a which is temporarily switched on. This way the two sources have different support in time which do not overlap: $\int \mathrm{d}t\, J_x^e J_x^a = 0$. We take the emitter and absorber source to be temporally smeared-out point sources (4.51) such that a communication source reads

$$J_x^c = \frac{1}{\sqrt{8\pi\sigma^2}} \left(\delta_{\mathbf{x}\mathbf{x}_e}^{(3)} \exp\left\{\frac{-(t-t_e)^2}{2\sigma^2}\right\} + \delta_{\mathbf{x}\mathbf{x}_a}^{(3)} \exp\left\{\frac{-(t-t_a)^2}{2\sigma^2}\right\}\right). \tag{4.53}_{\mathcal{QHS}}$$

Inserting this source into the VPA (4.49) results in four terms in the exponential. Two terms are self-interacting contributions and depend either solely on J^e or J^a leading to $|\langle\, 0_f \,|\, 0_i \,\rangle_{J^e}^0|^2$ and $|\langle\, 0_f \,|\, 0_i \,\rangle_{J^a}^0|^2$ analogous to (4.52). The other two terms include both J^e

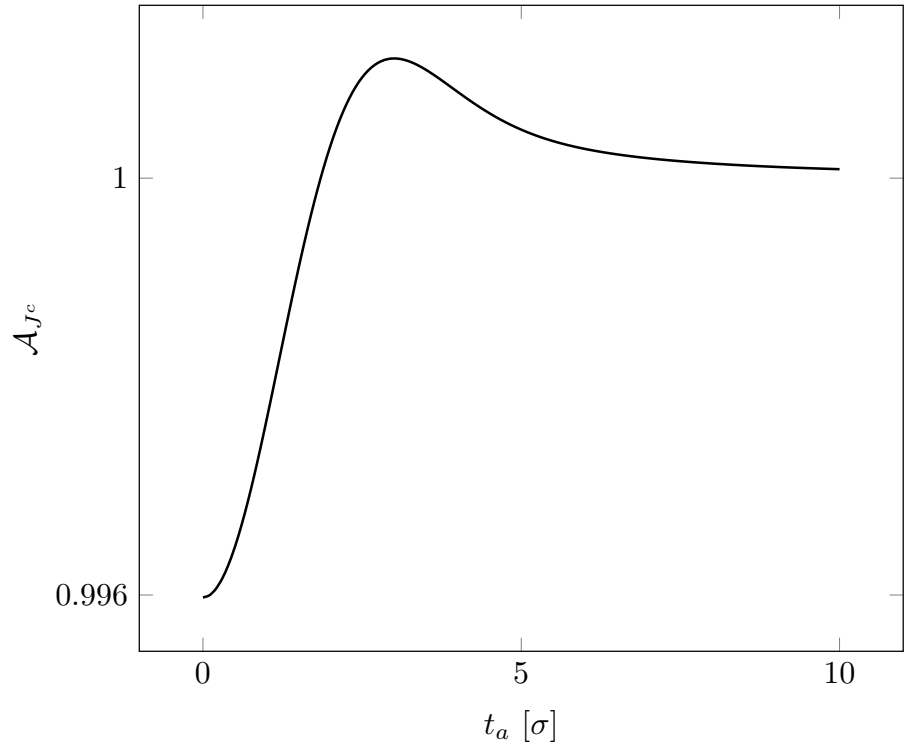

Figure 4.8.: Causal contribution to the VPA for an external point source which is switched on and off two times with a temporal Gaussian profile centered around $t_e = 0$ and t_a with standard deviation σ.

and J^a and thus require the propagator between the emitter and absorber. This new contribution reads

$$\mathcal{A}_{J^c} := \frac{|\langle\, 0_f \,|\, 0_i \,\rangle^0_{J^c}|^2}{|\langle\, 0_f \,|\, 0_i \,\rangle^0_{J^e}|^2 \, |\langle\, 0_f \,|\, 0_i \,\rangle^0_{J^a}|^2} = \exp\left\{ -\int \frac{\mathrm{d}^3k}{(2\pi)^3} \frac{e^{-\omega_k^2\sigma^2}}{16\omega_k\pi} \cos\left[\omega_k(t_a - t_e) - \mathbf{k}(\mathbf{x}_a - \mathbf{x}_e)\right] \right\}. \tag{4.54}$$ $\mathcal{QHS}$

$\mathcal{A}_{J^c}$ either amplifies the self-interaction contribution or decrease its effect depending on the spatial distance between the sources $\mathbf{x}_a - \mathbf{x}_e$ and the temporal difference $t_a - t_e$. However, this effect is strictly smaller than the self-source effects $|\langle\, 0_f \,|\, 0_i \,\rangle^0_{J^e}|^2$ and $|\langle\, 0_f \,|\, 0_i \,\rangle^0_{J^a}|^2$ such that the VPA remains smaller than one.

As a first example let us consider an external point source (4.53) which is turned on and off smoothly two times with $J^c|_{\mathbf{x}_e=\mathbf{x}_a}$ and σ finite. We choose the values $t_e = 0$ and $t_a > 0$ for clarity. Performing the integration yields the behavior depicted in Fig. 4.8. We can see that if the difference between t_e and t_a is taken sufficiently large $t_a \gg \sigma$, the causal part of the VPA (4.54) is negligible due to the smallness of the overlap of the Gaussian functions. For $t_a = 0$ the source (4.53) is not turned on and off twice but only once and thus reduces to the source (4.51) and the VPA (4.52). Between those two extremes of

$t_a = 0$ and $t_a \gg \sigma$, a transition from a decrease of the VPA to an enhancement can be seen in a region where the Gaussian functions overlap substantially $t_a \approx 3\sigma$.

In this Section, we analyzed the sources (4.51) and (4.53) in a Minkowski spacetime. With these results we can in the next Section place the very same sources into the background of the fixed shell and evaluate the differences. This way we analyze the contribution of the curved background and use this external source construction as a tool to detect potential pathologies introduced by the background geometry.

4.3.2. Vacuum Persistence in a Suspended Shell Background

To analyze whether quantum fields evolve unitarily throughout all phases of black-hole formation, we compute the vacuum persistence amplitude (VPA) in a fixed shell geometry as in [12] together with Florian Niedermann. To this end, we analyze the stability of the initial vacuum state $|0_i\rangle$ associated with an inertial observer inside the shell. Since the interior is a Minkowski spacetime with line element (3.63), we construct the quantum field inside the shell as follows,

$$\phi_x = \int \frac{\mathrm{d}^3k}{\sqrt{(2\pi)^3 2\omega_k}} \left(e^{ik_\mu x^\mu} a_{\mathbf{k}} + e^{-ik_\mu x^\mu} a^\dagger_{\mathbf{k}} \right), \tag{4.55}\,{}^{b}_{\mathcal{Q}\,\mathcal{H}\,\mathcal{G}}$$

with the creation operator $a^\dagger_{\mathbf{k}}$ and the annihilation operator $a_{\mathbf{k}}$ which annihilates the vacuum $a_{\mathbf{k}} |0_i\rangle = 0$. Next, we place a source J inside the fixed shell and use the propagator (3.68) together with the RNC expansion point (3.73) for the VPA (4.48),

$$\left| \langle\, 0_f \,|\, 0_i \,\rangle^0_J \right|^2 = \exp\left\{ - \operatorname{Im}\left(\int_{\mathcal{M}} \mathrm{d}\mu_x \, \mathrm{d}\mu_y J_x \Delta_{xy} J_y \right) \right\} . \tag{4.56}\,{}^{b\,a\,l\,p\,s}_{\mathcal{Q}\,\mathcal{H}\,\mathcal{G}}$$

Since the source J is located in the interior of the shell, the VPA (4.56) contains nontrivial information about the curved geometry in the exterior through the reflection part of the propagator Δ and therefore the reflection coefficient in (3.71). We have found the non-perturbative reflection propagator by applying various approximation methods and constraints $(a\,l\,p\,s)$, and thus must choose a source that consistently accounts for all of these as well. As shown in App. D, the temporally smeared-out point source (4.51) can satisfy these criteria. Localizing the source at $\mathbf{x}_J$, it scales in configuration space with $J_x \propto \delta^{(3)}_{\mathbf{x}\mathbf{x}_J} \exp\{-(x^t)^2/(2\sigma_t^2)\}$ and is given in momentum space by

$$J(\mathbf{k}) = \frac{1}{\sqrt{2\pi}} e^{i\mathbf{k}\mathbf{x}_J} \exp\left\{ -\frac{\left(\omega_k - \langle\omega_k\rangle\right)^2}{2} \sigma_t^2 \right\}, \tag{4.57}\,{}^{}_{\mathcal{Q}\,\mathcal{H}\,\mathcal{S}}$$

with the mean $\langle\omega_k\rangle$. σ_t and $\langle\omega_k\rangle$ are both constrained by the validity of the used approxi-

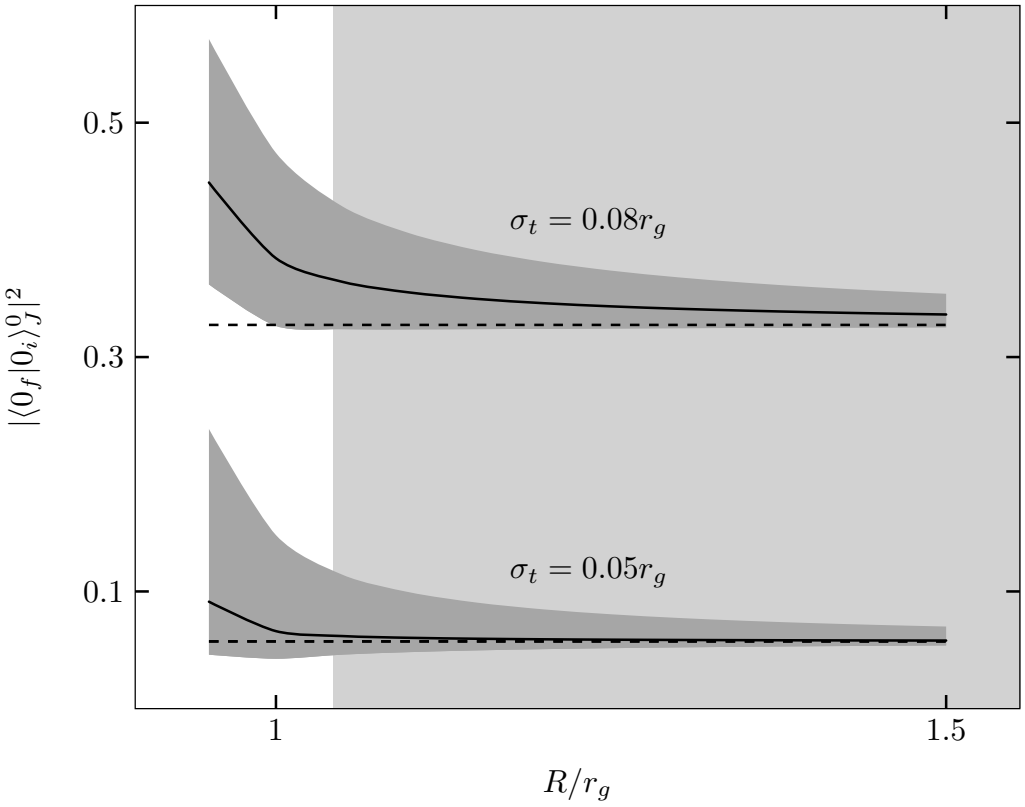

Figure 4.9.: Vacuum persistence amplitude (4.56) for a temporally smeared-out point source (4.57) inside a fixed shell of radius R. The distance from the source to the shell is $0.005r_g$ for the central solid line and zero for the upper and $0.01r_g$ for the lower boundary of the dark shaded regions. The RNC are constructed around the point (3.73) for $\alpha = 0$. The parameters for the source used in the upper plot are $\sigma_t = 0.08r_g$ and $\langle\omega_k\rangle = 4/\sigma_t$ while for the lower plot $\sigma_t = 0.05r_g$ in line with the validity discussion in App. D. The dashed lines are the Minkowski contributions of the sources, which serve as a reference corresponding to the fraction that is insensitive to the shell and its external geometry. The radii $R/r_g > 25/24$ are presented shaded in the background to depict the region in which the shell can be stabilized with respect to standard matter.

mations as explained in App. D. As valid examples, we choose $\sigma_t/r_g = 0.08 \ll 1$ together with $\sigma_t/r_g = 0.05 \ll 1$ and $\langle\omega_k\rangle r_g = 4r_g/(\sigma_t) \gg 1$ to investigate the influence of σ_t on the VPA.

With all this in mind, we present in Fig. 4.9 the VPA (4.56) as a function of the shell radius R/r_g and the distance between the shell and the source at $\mathbf{x}_J$. The dashed lines are the VPAs in the absence of the shell and are thus given by the results of Sec. 4.3. The deviation from this Minkowski result is more pronounced as R approaches r_g, indicating a change in the vacuum structure close to black-hole formation. Due to the spatial fall-off of the propagator, the effect of reflection is less significant when the boundary is farther away. The central result of this analysis is that the VPA is smooth and always less than one, thus respecting the bound (4.50) and preserving the probabilistic interpretation of

quantum field theory in this setup. However, in Fig. 4.9 it can also be seen that especially for $R \approx r_g$ the VPA increases for larger σ_t. This raises the research question of whether this amplification leads to a VPA larger than one when σ_t is comparable to the black-hole lifetime and this way connecting to the work of Page [21]. This long-time behavior could be studied using FNC, which do not share the time constraint of the RNC construction, as discussed in Sec. 3.1.5.

While these results allow for a first consistency check for black-hole formation, the fixed shell has to be replaced with a collapsing shell in order to validate that black-hole formation is indeed paradox-free. Since the techniques developed in this Chapter reach their limits for a collapsing shell with radius $R \approx r_g$, we investigate in the next Chapter the complement approach of quantum graphs which does allow for such an analysis.

5. Analyzing Black-Holes with Quantum Graphs

As we have seen in the last Chapter, there is a need for a new approach in quantum field theory in curved spacetimes to investigate black-hole formation. In this Chapter we investigate a novel approach of compact quantum graphs which consist of idealized one-dimensional edges connected by vertices as depicted in Fig. 5.1. As we will show, quantum graphs contain the essential structure to grasp the black-hole properties such that it can conveniently be extracted by feasible analytical calculations. In Sec. 5.1 we introduce the construction of quantum graphs in the optical analogue system to investigate propagation across transitions and generalize to entanglement entropy and black-holes in Sec. 5.2 and Sec. 5.3.

5.1. Quantum Graphs

Consider a quantum graph $\mathcal{G}$ embedded in a globally hyperbolic manifold $\mathcal{M} = \mathbb{R}_T \times \Sigma$ with metric g and thus a generalized version of previous works of quantum graphs in a Minkowski background [108, 109]. As depicted in Fig. 5.1 for a $(2+1)$ dimensional setup, we choose a quantum graph which is constructed out of straight edges e, which are connected via vertices v. Furthermore, we parameterize a position on a specific edge of length ℓ with $x \in \mathcal{I} := [0, \ell]$. Then $Z : \mathbb{R}_T \times \mathcal{I} \to \mathcal{M}$ maps a point on the edge to the manifold $\mathcal{M}$ and a scalar field $\varphi : \mathcal{M} \to \mathbb{R}$ assigns any point in the manifold a certain value. With these definitions we can define a real scalar field confined onto the edge with $\phi := \varphi \circ Z$:

$$\begin{aligned} &\Phi : \mathbb{R}_T \times \mathcal{I} \to \mathbb{R} \,, \\ &\phi_x = \varphi\big(Z_x\big) \,. \end{aligned} \tag{5.1}$$

This resembles a conformal field theory for ϕ which as previously discussed simplifies computations of observables tremendously no matter how complicated the background geometry is. For instance, the mode functions on each edge are plane waves.

The Laplace operators introduced in the equations of motion on each edge can be

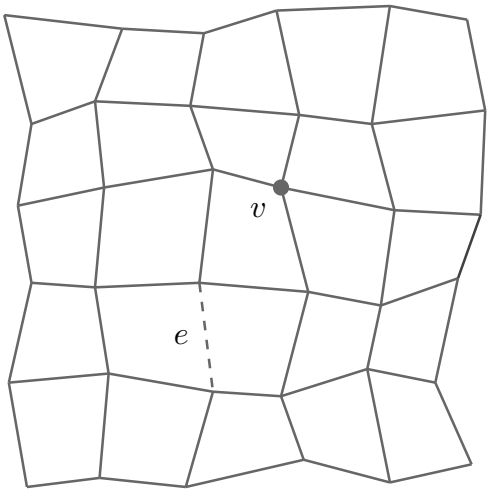

Figure 5.1.: A $(2+1)$ dimensional quantum graph made up of straight edges like the dashed one e that are linked with vertices like v depicted with a dot.

generalized to a self-adjoint operator on the whole graph if certain boundary conditions for ϕ are applied at each vertex [108,109]. The condition on self-adjointness, however, does not uniquely determine the boundary conditions but leaves room for ambiguousness which are relevant for the physical properties of the vertices [110]. We choose the Kirchhoff-Neumann boundary conditions which preserve the current and thus are preferred for describing the propagation of a field through a quantum graph. For a vertex connecting two edges, these conditions translate to the standard continuity conditions for ϕ which we encountered at the reflection and transmission off interfaces. In this way, at each vertex transmission and reflection can occur encoding properties of the spacetime or medium the quantum graph is embedded in.

To illustrate this, let us investigate the optical setup of two half-spaces filled with different media which we discussed in Sec. 2.1.2. First, we take the simple graph setup of one edge in each half-space connected with a vertex at the interface as depicted in Fig. 5.2a). Analogous to the $(3+1)$ dimensional counterpart in (2.24), the action of the scalar field on this graph reads

$$S = -\frac{1}{2}\int_{\mathcal{S}^C} \mathrm{d}\mu\,(\eta_\varepsilon^{\mu\nu}\partial_\mu\phi\partial_\nu\phi + 2\phi J) - \frac{1}{2}\int_{\mathcal{S}} \mathrm{d}\mu\,\eta_{\varepsilon_S}^{\mu\nu}\partial_\mu\phi\partial_\nu\phi\,, \qquad (5.2)\,{}^{b}_{\mathcal{H}\,\mathcal{S}}$$

with measure $\mathrm{d}\mu_x = \mathrm{d}^2x\sqrt{-\det(\eta)}$ and $\eta_{\varepsilon|\varepsilon_S} = \mathrm{diag}(-1/\varepsilon|\varepsilon_S, 1)$. Following the same steps as in Sec. 2.1.2 the reflection and transmission propagators read

$$G^<_{xy} = -\int_k^\varepsilon e^{-ik(x+y)}\mathcal{R} \qquad G^>_{xy} = \int_k^\varepsilon e^{iqx-iky}\,\mathcal{T} \qquad (5.3)\,{}^{b}_{\mathcal{H}\,\mathcal{S}}$$

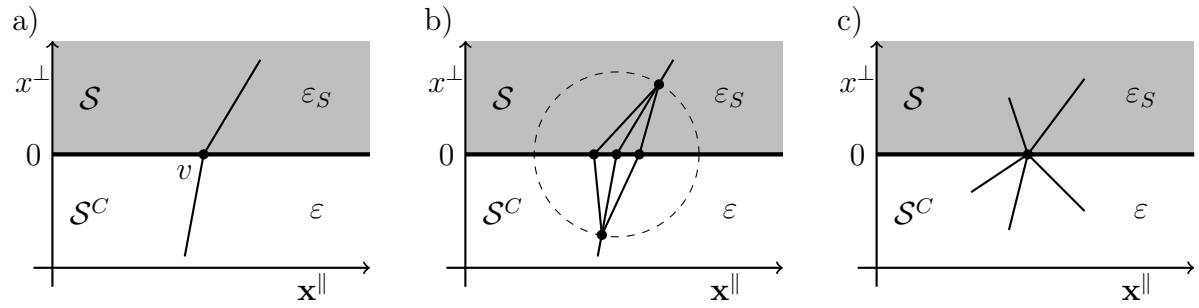

Figure 5.2.: Quantum graphs probing the properties of the two half-space system with susceptibility ε_S in $\mathcal{S}$ and susceptibility ε in $\mathcal{S}^C$. a) depicts the minimal construction with a vertex v located on the interface such that the quantum field follows a dispersion relation which depends solely on one susceptibility for each edge. In b) is a quantum graph shown which depends on the angles between the external edges and the interface such that it is sensitive to angle dependent phenomena in $(3+1)$ dimensions. Compared to the graph in a) two paths are added, which can be generalized to more paths in order to increase the resolution on the angle dependency. In c) a star graph is shown with which any graph can be constructed.

with $q^2 = k^2\varepsilon_S/\varepsilon$ and the shorthand now reads

$$\int_k^\varepsilon := i\int \frac{\mathrm{d}k}{4\pi\omega_k^\varepsilon\varepsilon} e^{-i\omega_k^\varepsilon(x^t-y^t)}\,. \tag{5.4}$$

The reflection and transmission coefficients are equivalent to the normal incidence case of (2.32),

$$\mathcal{R} = \frac{q-k}{k+q} = \frac{\sqrt{\varepsilon_S}-\sqrt{\varepsilon}}{\sqrt{\varepsilon}+\sqrt{\varepsilon_S}}\,, \qquad \mathcal{T} = \frac{2k}{k+q} = \frac{2\sqrt{\varepsilon}}{\sqrt{\varepsilon}+\sqrt{\varepsilon_S}}\,. \tag{5.5}$$

The dependence on the incident angle in (2.32) is encoded in q whereas (5.5) does not encode any angle information. Therefore, in this minimal graph setup we can only investigate the normal incident scenario of the full $(3+1)$ dimensional treatment. To recover the angle dependency, more complex graphs must be explored, such as the one in Fig. 5.2b), which is being investigated in collaboration with Cecilia Giavoni with findings which will be published elsewhere. With the additional edges and vertices there are more paths to propagate from the lower half-space to the upper half-space which can lead to constructive or destructive interference. Taking the external edges to be normal to the dashed circle, the internal lines will change depending on the angle between the external lines and the interface. In this way the interior of the dashed circle acts like an extended vertex which is sensitive to these angles and $(3+1)$ dimensional effects such as the Brewster angle can be investigated.

Both graphs in Fig. 5.2a) and Fig. 5.2b) rely on vertices on the interface which connect

two edges and thus the standard smoothness conditions on ϕ are applied. Nevertheless, the Kirchhoff-Neumann boundary conditions generalize to vertices with more edges attached such as the star graph in Fig. 5.2c). As explored with Patricia Ribes Metidieri in [110], the reflection and transmission coefficients for such a star graph in the two half-space system are given by

$$\mathcal{R} = 1 - \frac{2\sqrt{\varepsilon}}{\sum_i \sqrt{\varepsilon_i}}\,, \qquad \mathcal{T} = \frac{2\sqrt{\varepsilon}}{\sum_i \sqrt{\varepsilon_i}}\,, \tag{5.6}\,{}^{b}_{\mathcal{H}\,\mathcal{S}}$$

where ε_i is the susceptibility of the medium in which the ith edge is located. With the description of a star graph at hand, arbitrary complicated graphs such as the one in Fig. 5.1 can be constructed by combining star graphs with each other.

Although we only demonstrated quantum graphs in an optical test setup in this Section, their applicability is far ranging. For instance, as investigated in [110], quantum graphs allow to analyze an accelerating interface in the two half-space system. This can be viewed as a generalization of the (1+1) dimensional analysis of moving mirrors introduced in [111] since with quantum graphs the interface does not have to reflect totally and effects which are present in $(3 + 1)$ dimensions can be addressed. Accelerated mirror models are of particular interest since they serve as toy models for the gravitational collapse [112–114]. Therefore, generalizing the investigation of moving mirror models with quantum graphs also expands the research of particle creation or black-hole formation in gravitational collapse models.

In this work, we introduce quantum graphs for black-holes by establishing the area law of entanglement entropy. The area law is a quantum field theory effect that depends on a geometrical $(3 + 1)$ dimensional quantity and thus illustrates the emergence of higher dimensional effects on a graph naturally.

5.2. Entanglement Entropy of Black-Holes

There is a deep connection between the entanglement entropy and Hawking radiation in black-hole thermodynamics and thus to the information paradox. Therefore, understanding the entanglement entropy of a black-hole opens up new possibilities for the understanding of quantum field theory in curved spacetimes. Seminal work towards a microscopic derivation of the entanglement entropy of a black-hole was performed in [115] in which a sphere was traced out in a Minkowski background simulating a black-hole. In this Section we summarize the investigation of this entanglement entropy using quantum graphs carried out in collaboration with Cecilia Giavoni in [39]. Before we employ quantum graphs in Sec. 5.2.2, we summarize the treatment of a partly traced out scalar field

as presented in [115, 116] for a $(3+1)$ and $(1+1)$ dimensional setup.

5.2.1. The Area Law of Entanglement Entropy

As introduced in Sec. 4.1, employing the Schrödinger picture of quantum field theory the Hamilton operator for a scalar field with mass m in a Minkowski background reads

$$H[\Phi] = \frac{1}{2}\int \mathrm{d}^3\mathbf{x}\left[\Pi_{\mathbf{x}}^2 + |\nabla\Phi_{\mathbf{x}}|^2 + m^2\Phi_{\mathbf{x}}^2\right] . \tag{5.7}$$ $_{\mathcal{Q}\,\mathcal{H}\,\mathcal{S}}$

We trace out the quantum field within a sphere and thus exploit the spherical symmetry by using spherical coordinates and expand Φ and Π in real spherical harmonics Y_{lm}. Discretizing the system with a spherical lattice constructed out of N shells, the Hamilton operator (5.7) can be written as $H[\Phi] = \sum_{lm} H_{lm}[\Phi]$ with [115]

$$H_{lm}[\Phi] = \frac{1}{2a}\sum_{i=1}^{N}\left(\tilde{\Pi}_{lm,i}^2 + \sum_{j=1}^{N}\Phi_{lm,i}K_{ij}\Phi_{lm,j}\right) , \tag{5.8}$$ $^{d}_{\mathcal{Q}\,\mathcal{H}\,\mathcal{S}}$

where a is the distance between nearest neighbor shells, $\tilde{\Pi}_i = a^2\Pi_i$ and

$$K_{ij} = \left(\frac{l(l+1)}{i^2} + m^2a^2 + \frac{(i-\frac{1}{2})^2}{i^2} + \frac{(i+\frac{1}{2})^2}{i^2}\right)\delta_{ij} - \frac{(j+\frac{1}{2})^2}{j(j+1)}\delta_{i,j+1} - \frac{(i+\frac{1}{2})^2}{i(i+1)}\delta_{i+1,j} , \tag{5.9}$$ $^{d}_{\mathcal{Q}\,\mathcal{H}\,\mathcal{S}}$

where we chose Dirichlet boundary conditions such that $\Phi_{lm,0} = 0$ and $\Phi_{lm,N+1} = 0$. Except for the angular momentum and mass term, the terms in (5.9) encapsulate the oscillators' nearest neighbor interaction.

As in the original article [115], we analyze the scalar field's ground state $|\,\psi\,\rangle$ and trace out a sphere with radius $R = a\,(n+1/2)$. The resulting entanglement entropy is calculated using the density operator $|\,\psi\,\rangle\langle\,\psi\,|$, which is determined by the matrix $\Omega = \sqrt{K}$, which we cast into the form,

$$\Omega = \begin{bmatrix} \mathcal{A} & \mathcal{B} \\ \mathcal{B}^T & \mathcal{C} \end{bmatrix} , \tag{5.10}$$ $^{d}_{\mathcal{Q}\,\mathcal{H}\,\mathcal{S}}$

where $\mathcal{A}$ is a $n \times n$ matrix accounting for correlations and self-interactions between the n traced out oscillators, $\mathcal{C}$ is a $(N-n)\times(N-n)$ matrix accounting for (self-)correlations between oscillators outside the entanglement sphere, and $\mathcal{B}$ is a $n \times (N-n)$ matrix accounting for correlations across the entanglement sphere surface. We will use indices with subscript 1, i_1, ranging from 1 to n and indices i_2 ranging from $(n+1)$ to N such that the different parts of Ω can easily be identified in the following expressions.

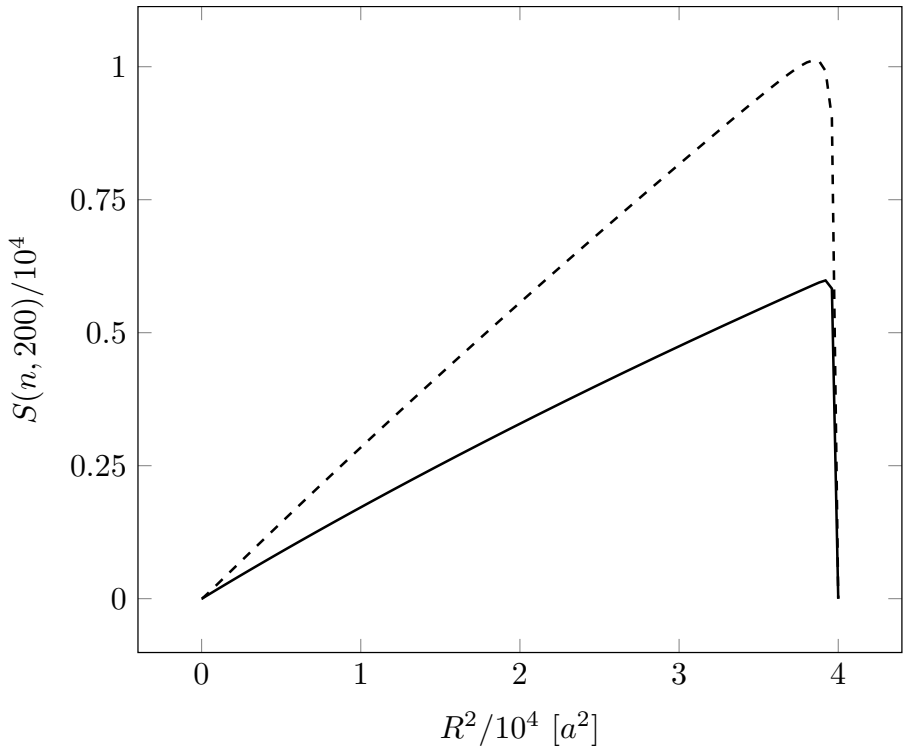

Figure 5.3.: Entanglement entropy in $(3+1)$ dimensions as a function of the entangling sphere radius squared with $N = 200$ for a scalar field with $ma = 1$ for the solid line and $m = 0$ for the dashed line.

With this construction, as discussed in [115], the entanglement entropy with n traced out harmonic oscillators can be determined with $S(n, N) = \sum_l (2l+1) S_l(n, N)$, where

$$S_l(n, N) = \sum_{i_2=n+1}^{N} \left(-\ln(1-\xi_{i_2}) - \frac{\xi_{i_2}}{1-\xi_{i_2}} \ln \xi_{i_2} \right) . \tag{5.11}$$ $^d_{\mathcal{Q}\mathcal{H}\mathcal{S}}$

With the eigenvalues λ_{i_2} of the matrix $\gamma^{-1}\beta$, ξ_{i_2} is computed with

$$\xi_{i_2} = \frac{\lambda_{i_2}}{1 + \sqrt{1-\lambda_{i_2}^2}} , \qquad \beta = \frac{1}{2} \mathcal{B}^T \mathcal{A}^{-1} \mathcal{B} , \qquad \gamma = \mathcal{C} - \beta . \tag{5.12}$$ $^d_{\mathcal{Q}\mathcal{H}\mathcal{S}}$

The numerical result of the entanglement entropy as a function of the entangling sphere's radius for a scalar field with different masses is presented in Fig. 5.3. The plots' linearity demonstrates the area law of entanglement entropy, i.e. $S(n, N) \propto R^2$, as originally demonstrated in [115]. Because the whole system is integrated out for $n = N$, the entanglement entropy vanishes for $n \to N$. However, decreasing entropies occur only in finite-size systems, which is not the case for a black-hole in an unlimited universe which makes this effect of secondary interest for our investigation.

We now repeat the same procedure in $(1+1)$ dimensions because a single edge of a

quantum graph is a $(1+1)$ dimensional entity and thus the microscopic phenomenology of entanglement entropy on a graph is related to the entanglement entropy in $(1+1)$ dimensions. For that matter, consider a free massive scalar quantum field on a $(1+1)$ dimensional lattice with Hamilton operator

$$H[\Phi] = \frac{1}{2a}\sum_{i=1}^{N}\left(\tilde{\Pi}_i^2 + \sum_{j=1}^{N}\Phi_i K_{ij}\Phi_j\right), \tag{5.13}\,{}^{d}_{\mathcal{Q}\,\mathcal{H}\,\mathcal{S}}$$

where with Dirichlet boundary conditions K is given by

$$K_{ij} = \left[2 + m^2a^2\right]\delta_{ij} - \delta_{i,j+1} - \delta_{i+1,j}\,. \tag{5.14}\,{}^{d}_{\mathcal{Q}\,\mathcal{H}\,\mathcal{S}}$$

As we will see, the analytic derivation of the entanglement entropy in (1+1) is important for our investigation of entanglement entropy on quantum graphs. Therefore, we follow closely [116] for the analytical derivation and rewrite K as

$$K_{ij} = \left(\frac{k_i}{\varepsilon}\right)^2\delta_{ij} - \delta_{i+1,j} - \delta_{i,j+1}\,, \tag{5.15}\,{}^{d}_{\mathcal{Q}\,\mathcal{H}\,\mathcal{S}}$$

with

$$k_i := \varepsilon\sqrt{2 + m^2a^2}\,. \tag{5.16}\,{}^{d}_{\mathcal{Q}\,\mathcal{H}\,\mathcal{S}}$$

The auxiliary parameter ε specifies the ratio of K's non-diagonal and diagonal terms. As can be seen in (5.15), diagonal terms dominate for large masses, such that ε can be regarded as a smallness parameter if the mass is chosen sufficiently large. Computing Ω to the leading order of ε, results in

$$\mathcal{A}_{i_1j_1} = \frac{k_{i_1}}{\varepsilon}\delta_{i_1j_1} + O(\varepsilon)\,, \quad \mathcal{C}_{i_2j_2} = \frac{k_{n+i_2}}{\varepsilon}\delta_{i_2j_2} + O(\varepsilon)\,, \quad \mathcal{B}_{i_1j_2} = -\frac{\delta_{i_1,n}\delta_{j_2,1}\varepsilon}{k_n + k_{n+1}} + O(\varepsilon^3)\,. \tag{5.17}\,{}^{d}_{\mathcal{Q}\,\mathcal{H}\,\mathcal{S}}$$

Notice that $\mathcal{A}$ is diagonal, implying that the oscillators in the interior of the entangling sphere are decoupled. The same applies to the exterior since $\mathcal{C}$ is diagonal too. Nonetheless, in $\mathcal{B}$, we take the correlation between the n-th oscillator and the $n+1$-th oscillator across the entangling sphere into account.

Following the previously described derivation for the entanglement entropy, one obtains [116],

$$S_{1+1}(n,N) = \frac{1 + 2\ln[4\,(2+m^2a^2)]}{16\,(2+m^2a^2)^2} + O(\varepsilon^8)\,, \tag{5.18}\,{}^{d}_{\mathcal{Q}\,\mathcal{H}\,\mathcal{S}}$$

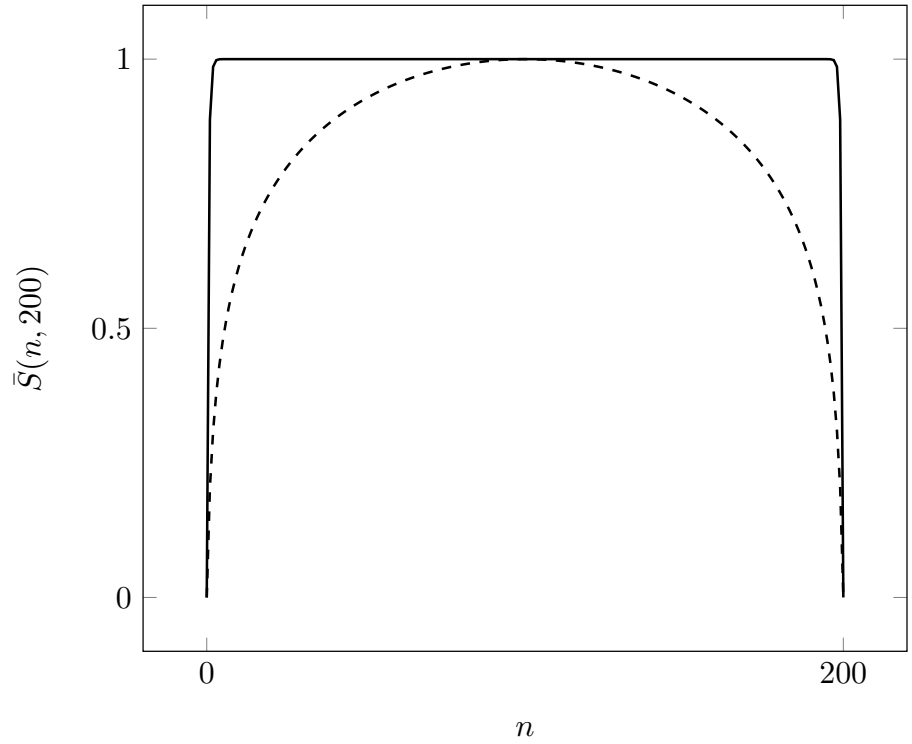

Figure 5.4.: The entanglement entropy of a chain of $N = 200$ oscillators in $(1 + 1)$ dimensions as a function of the number of traced out oscillators n is displayed. For the solid line, $ma = 1$, and for the dashed line, $m = 0$, which for better comparability is normalized to one for $n = 100$.

where n should not be chosen close to the boundaries $n = 0$ and $n = N$ in order to avoid boundary effects. The entanglement entropy, which displays the influence of the boundaries depending on the mass of the field, is numerically obtained in Fig. 5.4. From the numerical result, it is evident that the constant behavior in (5.18) is only a reliable approximation if the mass is large enough. That the entanglement entropy in $(1 + 1)$ dimensions is independent of n in the large mass limit is essential for our consideration. This conclusion is nothing else than the area law in $(1+1)$ dimensions because the *surface* of the interaction between the last traced out oscillator and the first one outside is just one point, regardless of which n-th oscillator is considered. With the area law in $(3 + 1)$ and $(1 + 1)$ dimensions discussed, we now analyze the entanglement entropy on quantum graphs in the next Section.

5.2.2. Quantum Graph Analysis of the Area Law

In this part, we investigate how the area law of entanglement entropy is encoded on quantum graphs. We discover that all graphs that yield the area law are similar to a three dimensional mesh graph for which we depicted a two dimensional version in Fig. 5.5. To calculate the entanglement entropy of these network graphs, we use a bottom-up approach,

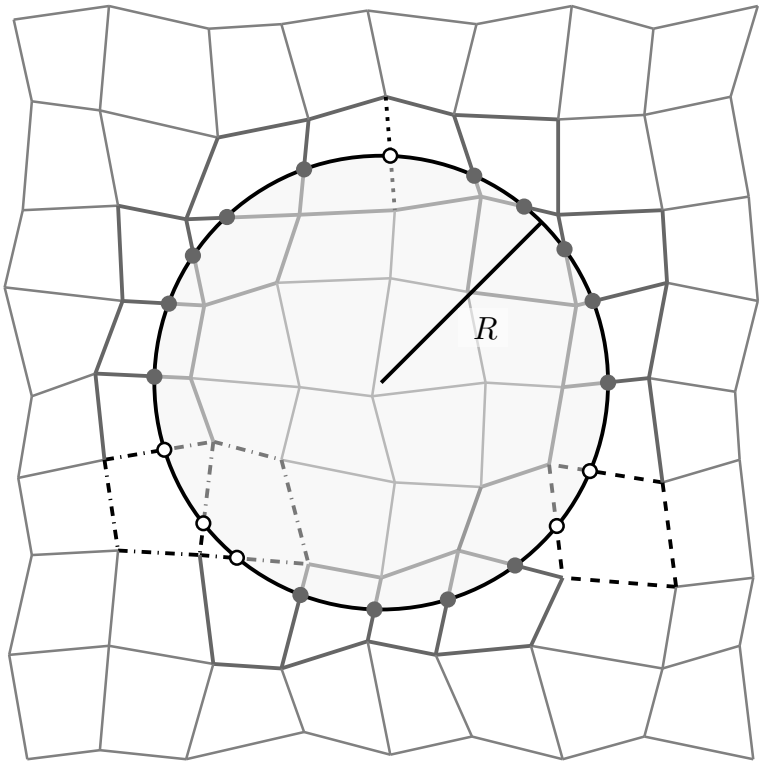

Figure 5.5.: A mesh graph in $(2+1)$ dimensions with the interior of a circle of radius R traced out. With thick edges, a ring-shaped subgraph is highlighted that includes all intersection points with the circle indicated with dots. As examples of basic building parts of this graph we show a dotted line for a single edge graph, a dashed line for a one loop graph, and a dot dashed line for a two loop graph.

starting with the microscopic components of a network graph, such as the highlighted parts in Fig. 5.5. With the microscopic characteristics of entanglement entropy analyzed then allows us to fully investigate the macroscopic entanglement entropy later on.

Microscopic Picture

The most fundamental building block of a mesh-like graph is a single edge, such as the dotted one shown in Fig. 5.5. Since an edge is a $(1+1)$ dimensional object, the entanglement entropy of a scalar field in $(1+1)$ dimensions, as defined in Sec. 5.2.1, is also the entanglement entropy of a scalar field restricted to a single edge. In this regard, (5.18) provides the entanglement entropy for a scalar field with a large mass on an edge. Since for now we are only interested in the relative change of the entanglement entropy in terms of n and not its precise value, we normalize the entanglement entropy to the value of a $(1+1)$ dimensional reference system at $n = N/2$,

$$\bar{S}(n,N) = \frac{S(n,N)}{S_{1+1}(N/2,N)}\,. \tag{5.19}$$

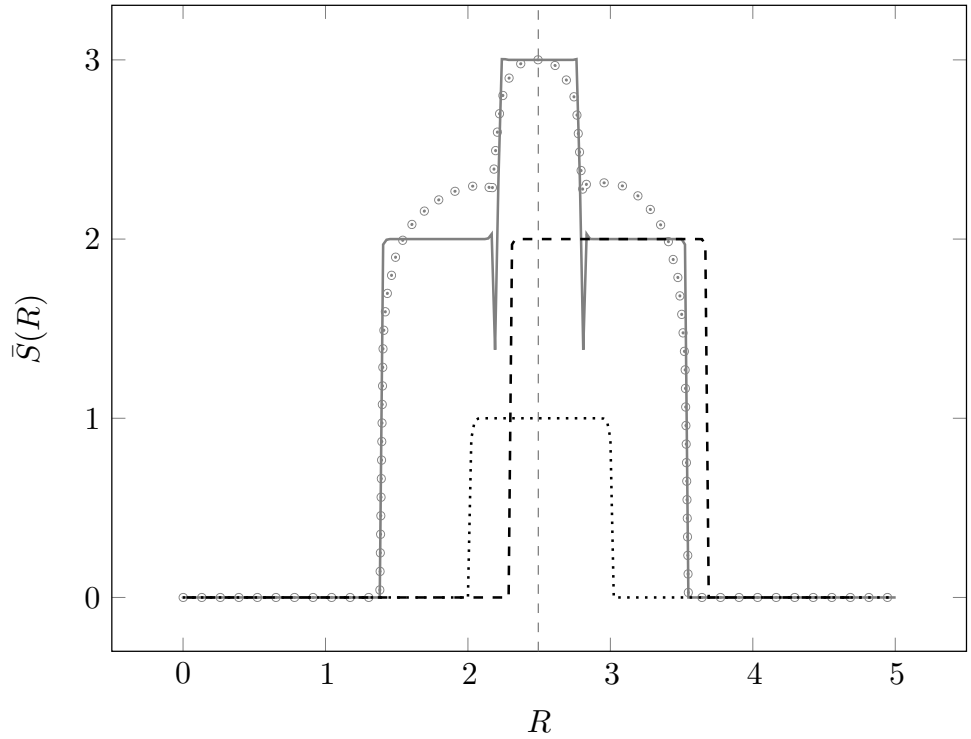

Figure 5.6.: Entanglement entropy in terms of the radius of the entangling sphere for the basic graphs presented in Fig. 5.5. In particular, the entanglement entropy for the edge graph (dotted), one loop graph (dashed), and two loop graph (solid for $ma = 1$ and normalized for $m = 0$ shown with circles) is provided. A vertical dashed line at $R = 2.5$ indicates the entangling sphere radius explicitly chosen in Fig. 5.5.

With this normalization, the entanglement entropy of the dotted edge in the arrangement depicted in Fig. 5.5 is set to $\bar{S}_{\text{edge}}(n, N) = 1$. When the radius of the entanglement sphere is doubled or halved, the edge is traced out entirely or not at all, leading to a vanishing entanglement entropy. Apart from small modifications due to boundary effects the numerical evaluation of the entanglement entropy shown in Fig. 5.6 emerges.

We can now design more complex components of the mesh graph using the edge as a fundamental building piece. By gluing four edges together, a *loop* graph resembling a loop, such as the dashed one in Fig. 5.5, may be created. For an analytic derivation of the entanglement entropy, gluing the ends of an edge graph together to form a loop graph is easier. In this manner, we use K from Eq. (5.14) and introduce an interaction between the first and N-th oscillator,

$$K_{ij} = \left[2 + m^2 a^2\right] \delta_{ij} - \delta_{i,j+1} - \delta_{i+1,j} - \delta_{i,1}\delta_{N,j} - \delta_{i,N}\delta_{1,j} \,. \tag{5.20}$$ $^{d}_{\mathcal{Q}\,\mathcal{H}\,\mathcal{S}}$

As a result, each oscillator now has two nearest neighbors and is hence indistinguishable from one another. In the large mass expansion, this leads to a change to (5.17) in the

matrix $\mathcal{B}$, which now reads

$$\mathcal{B}_{i_1 j_2} = -\frac{\delta_{i_1,n}\delta_{j_2,1}}{k_n + k_{n+1}}\varepsilon - \frac{\delta_{i_1,1}\delta_{j_2,N-n}}{k_1 + k_N}\varepsilon + O(\varepsilon^3)\,. \tag{5.21}$$

The two contributions to $\mathcal{B}$ correspond for the two intersection points, which are depicted in Fig. 5.5 as two white points. In comparison to the single edge graph, this extra intersection point results in an additional non vanishing eigenvalue ξ_N for the ground state density matrix. This eigenvalue adds a new n independent term to $S(n, N)$ in (5.11), contributing in $S(n, N)$ with the same value as ξ_{n+1} such that $\bar{S}_{loop}(n, N) = 2\bar{S}_{\text{edge}}(n, N) = 2$. This analytic result is in agreement with a numerical calculation of the entanglement entropy shown in Fig. 5.6 for the dashed loop graph given in Fig. 5.5.

In summary, only interactions across the surface of the entanglement sphere are significant in the large mass expansion. Therefore, one edge crossing the surface twice (or two edges crossing it once each) results in the same entanglement entropy [39]. Unlike a mesh graph, the radius of the entangling sphere has no effect on any of such graphs other than determining if the entanglement entropy is zero or not since the number of intersections is unaffected by the radius.

Until now, all graphs we investigated were totally describable using approaches of quantum field theory on a lattice. The single edge graph was quantum field theory in $(1 + 1)$ dimensions, and the loop graph simply modified the Dirichlet boundary conditions to periodic ones. In any case, we now explore more sophisticated graphs, which necessitate the use of graph concepts as introduced in Sec. 5.1.

Consider the dot dashed two loop graph in Fig. 5.5. Instead of gluing several loop graphs together, we make X loop graphs by taking a one loop graph and adding internal edges. For example, the dot dashed two loop graph in Fig. 5.5, may be constructed using a one loop graph and an extra internal edge. As a result, we produce vertices that link three edges, for which the Kirchhoff-Neumann boundary conditions must be applied, as explained in Sec. 5.1. For technical aspects, we refer the reader to [117].

As a result of implementing a new edge and connecting it to two locations on the one loop, additional terms in K of Eq. (5.20) are introduced. The radius of the entanglement sphere R, as well as the form and position of the two loop graph, determine whether a new term in K impacts the matrices $\mathcal{A}$, $\mathcal{B}$, or $\mathcal{C}$. The additional interactions at the vertices contribute in the large mass expansion only if they appear as a term in $\mathcal{B}$, i.e., if they create an intersection. As a result, the entanglement entropy of two loop graphs or in general X loop graphs is non-trivial in terms of R.

To demonstrate this, Fig. 5.6 depicts the entanglement entropy of the two loop graph seen in Fig. 5.5. Aside from boundary effects, the entanglement entropy, as anticipated,

depends only on the number of intersection points with the entangling sphere. Since the boundary effects are more widespread for lower masses, the step-like behavior of the entanglement entropy is less prominent, as seen in Fig. 5.6.

This section concludes with the following observation: The number of intersections with the entangling sphere determines the microscopic entanglement entropy of a mesh graph in the large mass limit. This insight is essential for the justification of exchanging the mesh graph with simpler graphs in the following Section.

Macroscopic Picture

As previously demonstrated, the entanglement entropy of a scalar field with sufficiently large mass relies solely on the number of intersections of the graph with the entangling sphere surface. In this situation, a graph encompassing only the entangling sphere surface's vicinity may be sufficient to compute the correct entanglement entropy. In the example given in Fig. 5.5, the graph constructed out of the thick edges is a X loop graph that contains all intersections of the mesh graph with the entangling sphere surface. For different sphere radii, we must pick a distinct X loop graph to contain all intersection points. In this sense, the greater the radius of the entangling sphere, the greater the number of intersection points.

In [39], we examine various types of graphs, implementing the procedure to choose a distinct graph for each radius of the entangling sphere. Most importantly, we discovered that the interactions between the oscillators in angular directions have no effect in the large mass limit. Because of this, we can now use a basic graph construction to obtain the entanglement entropy of the system. The entanglement entropy of a single radial edge in the large mass limit is given by (5.18). Taking one such minimal graph for a unit area element $\tilde{a}^2$, we construct a star graph with the vertex in the origin such that each edge equally contributes to the entanglement entropy. Due to the Poincaré invariance of the quantum field, we must implement $\tilde{a}$ as a constant and therefore not dependent on R, such that the density of the local interactions is uniform throughout the spacetime. In this way, the area of the entangling sphere determines the number of these radial graphs and the entanglement entropy for a given radius R is given by

$$S(R) = \frac{4\pi R^2}{\tilde{a}^2} S_{1+1}\left(\frac{N}{2}, N\right) = \frac{4\pi R^2}{\tilde{a}^2}\left[\frac{1 + 2\ln[4\,(2+m^2a^2)]}{16\,(2+m^2a^2)^2} + \mathcal{O}(\varepsilon^8)\right]. \qquad (5.22)\,{}^{d}_{\mathcal{Q}\mathcal{H}\mathcal{S}}$$

This yields the area law in $(3+1)$ dimensions, $S(R) \propto R^2$. In this construction, the area law emerged in the large mass limit since it only depends on the number of intersection points with the entangling sphere surface. The main advantage of this minimal approach compared to others is that we just had to compute the entanglement entropy in $(1+1)$

dimensions. Because of its simplicity, this method is ideally suited for treatments in more complicated contexts, such as that of a gravitational collapse. Nevertheless, this technique necessitates sophisticated knowledge of the system, here the microscopic entanglement entropy, and is dependent on the large mass limit.

Therefore, we also examined mesh graphs in [39] that do not require that knowledge and also allow to obtain the area law for the entanglement entropy for low masses. In order to obtain the area law for low masses correlations on a graph in angular directions are needed. In a nutshell, edges in angular directions allow for the emergence of angular momentum which itself acts like a mass term such that the large mass result, the area law, is obtained. The very same behavior can be studied in $(3+1)$ dimensions by artificially restricting to certain modes with specific angular momentum in (5.9). The are law only emerges if either a large mass is chosen such that $ma \gg 1$ or enough modes of different angular momenta are taken [39]. Taking a star graph previously does not account for any angular momentum such that only the $l = 0$ mode contributes which only results in an area law if the mass is sufficiently large. In addition, we used mesh graphs to validate all of the previously chosen assumptions [39].

In conclusion, the study of entanglement entropy on quantum graphs revealed three key facts. First, taking a mesh graph all phenomena of $(3+1)$ dimensions can be analyzed despite its construction only relying on $(1+1)$ dimensions. Second, if we limit ourselves to a subset of observables, such as taking only fields with large masses into consideration, we may construct simpler quantum graphs that produce correct results for this subset of observables. These simpler graphs enable quicker numerical computation or even analytical derivation, such as in the case of the star graph employed in the large mass limit. Third, quantum graphs may be used as a diagnostic tool, identifying, amplifying, or weakening certain aspects of a physical process. For example, by choosing specific graphs for our entanglement entropy analysis, we were able to focus in detail on different contributions, such as the ones close to the entangling sphere surface in the microscopic picture, bulk contributions in the macroscopic picture, modes without angular momentum using a star graph, and so on and so forth. This procedure allowed us to develop a thorough understanding of the system at hand and is entirely general enough to be applied to more complex systems, as discussed in the next Section.

5.3. Quantum Graphs in Curved Spacetimes

The strength of quantum graphs was demonstrated in the previous Section on a Minkowski background, so we can now outline their applicability on a curved background. In that regard, we will first review the developments in $(1+1)$ dimensional black-hole formation

and later on discuss what quantum graphs can add to them.

In $(1+1)$ dimensions the Einstein-Hilbert action does not yield a dynamical equation of motion since it is a boundary term [118]. Non-trivial gravity actions are obtained for example by dimensionally reducing their $(3+1)$ dimensional counterparts. For the Schwarzschild black-hole, this means one integrates over the angular coordinates to obtain a $(1+1)$ dimensional action for gravity which now possesses a dilaton field [119]. In terms of analyzing the lower dimensional analogue of Hawking radiation the CGHS-model has been investigated which includes a dilaton field inspired by String theory [120]. In summary, as put in [121], these so-called generalized dilaton theories offer three central motivations to study them. First, as already mentioned higher dimensional gravity theories can yield one specific generalized dilaton theory after dimensional reduction. Second, String theory is a generalized dilaton theory in a certain limit. Third, since they allow for explicit computations they are taken as toy models to quantize gravity or to compute quantum field theory in curved spacetime effects such as Hawking radiation.

In addition to this bottom-up strategy, there is a top-down approach to studying black-hole formation. Instead of investigating a $(1+1)$ dimensional collapse to investigate black-hole formation, this approach takes the standard gravitational collapse in $(3+1)$ dimensions such as the Oppenheimer-Snyder model of a collapsing dust cloud and analyzes it for fixed angular coordinates [122]. This means, the probe field only exists along a radial line with constant angular coordinates and the boundary condition in the origin is usually taken such that the field is reflected to simulate the $(3+1)$ dimensional behavior [123]. This is equivalent to investigating black-hole formation in $(3+1)$ dimensions using a single radial edge graph with one end at the origin and the other one reaching to infinity. Because of this equivalence, we utilize this graph setup as the basis for more complex graph systems that allow us to be sensitive to additional effects of the black-hole formation, and therefore extend the research in the field.

Before we address our perspective on black-hole formation utilizing quantum graphs, we elaborate on the literature about angular coordinate restricted studies, that can always be thought of as investigations on a single radial edge graph. First and foremost the motivation to restrict the angular coordinates is because the resulting $(1+1)$ dimensional action for the probe field allows for analytic computations of effects such as Hawking radiation [123]. Since the motivation is clearly to still analyze properties of the $(3+1)$ dimensional collapse, this simplification comes with a cost. First, ambiguities solely related to $(1+1)$ dimensional scalar fields in curved spacetimes, such as how the Unruh state Wightman function changes due to isometries induced by the Killing vector field, must be addressed [123]. Second, findings in the $(1+1)$ dimensional treatment may not provide a complete picture of the process in $(3+1)$ dimensions, necessitating the construction

of a bridge between the higher and lower dimensional systems. For example, it is stated in [122] that during a gravitational collapse, the energy momentum tensor of a scalar probe field restricted to a set of angular coordinates is irrelevant to the dynamics of the collapse during black-hole creation. This statement is generalized to $(3+1)$ dimensions by employing energy conservation, which is suggested to connect the energy flux F^{3+1} across a sphere surface with radius R at light-like infinity $\mathcal{J}^+$ to the flux in $(1+1)$ dimensions F^{1+1} as follows [124],

$$F^{3+1}(\mathcal{J}^+) = \frac{\Gamma_0}{4\pi R^2} F^{1+1}(\mathcal{J}^+)\,. \tag{5.23}$$

The lower dimensional flux is distributed over the entire sphere's surface and hence divided by its area. It is worth noting that the same prefactor emerges when we employ a star graph, as we did in the context of entanglement entropy in Sec. 5.2. By incorporating the gray body factor Γ_0, the following effect of higher dimensions is taken into consideration. In contrast to the $(1+1)$ dimensional case, fields scatter off the gravitational background in $(3+1)$ dimensions, and hence some of the outgoing fields reflect back to the collapsing object and finally to the black-hole, and thus do not reach $\mathcal{J}^+$ which reduces the flux $F^{3+1}(\mathcal{J}^+)$ compared to $F^{1+1}(\mathcal{J}^+)$. Another contribution to the outgoing flux that cannot be included in the lower dimensional analysis comes from modes with non-zero angular momentum, because only spherical waves can be tracked along a radial line with constant angular coordinates. While some of these modes are capable to reach $\mathcal{J}^+$, most of them backscatter and contribute to energy fluxes in angular directions. The question of whether these contributions might possibly accumulate and drastically change the result of [122] cannot be answered in this $(1+1)$ dimensional framework.

Taking quantum graphs, however, we can conduct the following gedankenexperiment. Placing a radial edge graph in the system of a gravitational collapse, as previously described, provides the $(1+1)$ dimensional flux F^{1+1}. Generalizing to a star graph accounts for the area of the sphere surface in (5.23). Connecting the radial edges in the shape of a spider web, for instance, permits fields to propagate back and hence backscatter, potentially producing the gray body factor Γ_0 in (5.23). Moreover, as in the examination of entanglement entropy in Sec. 5.2, modes with angular momentum are included as well for such a graph. As shown in Sec. 3.3, the backscattering effect in $(3+1)$ dimensions is the reason why fields cannot leave a black-hole in the first place, hence performing these computations on systems with this property, such as a spider web graph, is desirable. In this way, as we will investigate in future work, quantum graphs provide a profound analysis of the gravitational collapse in $(3+1)$ dimensions while maintaining the simplicity of using $(1+1)$ dimensional physics on each edge.

6. Conclusion and Outlook

The goal of this work was to determine whether the evolution of quantum fields during black-hole formation is paradox-free. In analogy to this question, we first studied the propagation in optical systems possessing boundaries and interfaces between media with different susceptibilities. Thereby, we developed techniques to determine the propagator of a field crossing an interface that correctly reproduce known results of classical field theory. More precisely, we constructed methods to determine the Feynman propagator perturbative and non-perturbative in the difference of the susceptibilities and showed their compatibility. Since this approach is universal, we applied it to obtain the propagator in normal environments. Additionally, we investigated the domain of validity, causality in black-hole geometries and the explicit construction of the normal coordinates. The latter were Riemann normal coordinates, Fermi normal coordinates, and newly constructed temporally expanded Fermi normal coordinates.

For the analysis of black-hole formation, we considered a thin shell at rest made of physical matter and determined the surface pressure required to stabilize the shell. We then investigated this geometry in a local environment covering a part of the shell using normal coordinate patches such that we could formally map this system to the previously discussed optical one with two media. In this way, we succeeded in deriving the propagator for the thin shell system using the perturbative as well as the non-perturbative approach.

By using the propagator for the thin shell system, we analyzed how the formation of a horizon affects communication. A signal sent from the inside of the shell to the outside uses the transmitting part of the propagator and thus its transmittance. If the shell radii R are chosen closer and closer to the gravitational radius $R \to r_g$, the transmittance decreases smoothly until it finally vanishes for $R \leq r_g$. As a consequence, communication breaks down as soon as the shell exceeds its own horizon in accordance with causality.

With the propagator fulfilling these plausibility checks we considered the vacuum persistence amplitude inside the shell using an external source. Compared to the case without the shell, i.e. for a Minkowski spacetime, the amplitude is enhanced the closer the source is placed to the shell. This effect is stronger the longer the source is switched on and the closer the shell radius R is chosen to the gravitational radius r_g. Despite these origins of amplification, the amplitude never exceeds unity and thus the quantum field in the system

of a fixed shell possesses a unitary evolution. It should be noted, however, that this result was found under certain assumptions and constraints. Most remarkably, the setup used is only sensitive to microscopic time scales compared to the black-hole lifetime. Since sources that are turned on for longer periods of time showed larger amplification, it will be of particular interest in the future to investigate a setup that allows larger time scales. As suggested in earlier work, most notably by Page [21], relevant corrections should occur on time scales on the order of the black-hole lifetime. Since the time limiting factor for the system under consideration was the construction of a RNC patch, an analogous analysis with an FNC construction for an orbiting observer should allow an arbitrarily time-extended, but still local, investigation.

Consequently, one possibility to extend the research of fixed shells is to ask whether a quantum field in the fixed-shell background remains unitary on arbitrarily long time scales. Furthermore, the approximation of the outer geometry of the shell can be improved by either including more RNC patches or by increasing the adiabatic order of the RNC expansion. Additionally, since a fixed shell can at best approximate the various stages of black-hole formation, the switch to a dynamically collapsing shell and overcoming the difficulties involved is an essential part of future investigations. Since the spacetime of a collapsing shell is dynamical, we will study the vacuum persistence amplitude in dynamical spacetimes separately with the help of the Schrödinger picture of quantum field theory in [38].

Apart from all the improvements one can achieve for our black-hole formation analysis, the developed framework allows for a plethora of directions that can be taken for future projects. For example, the evanescent wave that we observed in the case of total reflection for a stabilized shell with radius $R < r_g$ might be related to particle creation and thus Hawking radiation. In this context, the entanglement entropy of a black-hole deserves special attention with a local treatment.

We took the first steps in this direction by analyzing the entanglement entropy resulting from tracing out a sphere of a quantum field in a Minkowski background as introduced in [125]. For that matter, we took quantum graphs and showed how they can supplement and complement the local computation of observables using normal neighborhoods. We demonstrated that quantum graphs can be applied for quantum fields in complicated backgrounds in two distinct manners. First, choosing a quantum graph with simple structure explicitly designed for the observable and system in question, one can analyze analytically the full $(3+1)$ dimensional effect while relying on easier $(1+1)$ dimensional physics on each edge of the graph. The second approach uses a mesh graph in order to be sensitive to any observables in an arbitrary system, which, however, requires a numerical derivation of expectation values due to the involved structure. Using both strategies, we

analyzed the entanglement entropy in Minkowski locally thoroughly and found matching results with the literature whenever present. This validates quantum graphs' capability to examine observables in quantum field theory and forecasts their eminent utility in any application of quantum fields in complicated systems such as dynamical and inhomogeneous gravitational or optical backgrounds.

With all the techniques developed in this thesis we plan as the next steps to investigate the following key aspects:

- Throughout analysis of the signature of dynamical black-hole formation on the entanglement entropy and particle production.
- Exploring open quantum system techniques for quantum fields in dynamical backgrounds to refine the tools for deducing quantum inconsistencies during the lifetime of a black-hole.

In conclusion, the local investigation of observables in complicated systems, such as the formation of black-holes employing normal neighborhoods and/or quantum graphs, is by no means completed and will reveal even more exciting discoveries in the future.

A. Principles, Restrictions and Approximations

Principles

The principles used in the main text and indicated as subscripts at equation numbers are listed here alphabetically. Note, the selection of principles is not unique, but was chosen to give an overall picture of the ideas that influenced this work the most.

$\mathcal{C}$ - Classical Physics of Point like Objects

The dynamics of a classical system is determined by the equations of motion, which can be derived from the action with the help of *Hamilton's Principle* [126]. In this way, for example, geodesics of point particles or *Fermat's Principle* (1662) of ray optics can be obtained. These solutions constitute a trajectory in configuration space, traversed by a point-like object, which thus perceives the system at a single point at any time.

$\mathcal{G}$ - General Relativity

General relativity is the natural extension of the Special Theory of Relativity by also covering accelerated observers. Due to the *Principle of Equivalence*, an observer cannot distinguish between being accelerated and being subjected to a homogeneous gravitational field [43]. General relativity can then be derived as a geometric theory of gravity in which masses curve spacetime, which is assumed to be torsion-free.

$\mathcal{H}$ - Huygens' Principle

Huygens' Principle serves as the basis for describing the propagation of waves of any kind [127]. Introduced on the level of the action using *Hamilton's Principle* the *Huygens' Principle* generates terms including spatial derivatives in contrast to point objects. This reflects that the described degrees of freedom perceive the system non-locally making all paths in configuration space relevant.

$\mathcal{Q}$ - Quantum Physics

In quantum physics, objects obey the *Principle of Superposition of States*, so that the results of measurements are only based on probabilities [128]. In the configuration space of a point particle this means that following *Huygens' Principle* a superposition of all paths with a weight determined by the action is considered [129]. A measurement singles out one path, and wave properties are observed by repeating the experiment many times.

$\mathcal{S}$ - Special Relativity

Special relativity relies on the restriction that the spacetime is isotropic and homogeneous, making all points in the spacetime indistinguishable. The *Principle of Relativity* holds, thus the laws of physics are equal for all observers which are at rest or moving with a constant velocity. With these ideas one can show that a maximum velocity exists and derive the formalism of special relativity [130].

Restrictions and Approximations

The restrictions and approximations used in the main text and indicated as superscripts at equation numbers are listed here alphabetically.

a - Finite Adiabatic Order

Spacetimes expanded in normal coordinates typically yield a metric with infinitely many terms [44, 45]. Working with a finite adiabatic order, i.e., truncating the series, is only reasonable if the higher order terms are negligible. This can be achieved for fields with small enough wavelengths. Similarly, in adiabatically evolving spacetimes, observables can be computed using finite adiabatic orders, for example, by employing a WKB ansatz [68].

b - Back-Reaction

Particles and fields are treated as perfect probes. This means that the effect they have on the medium or on the geometry is ignored.

c - Causal Order

If one specifies the causal order of two events connected by a Feynman propagator, one contribution of the propagator is filtered out, i.e., either that of the future light cone or that of the past light cone. In this way, the propagator can be derived more easily for one of the two contributions, and the other is subsequently added.

d - Discretization

To compute observables of quantum fields numerically, we discretize the spacetime, resulting in oscillators that are coupled to their nearest neighbors.

e - External Potential

Describing an atom we treat the Coulomb potential of the nucleus as an external quantity, i.e. classical, inert and the fundamental degrees of freedom creating this potential are not resolved.

l - Locality

Normal neighborhoods usually have finite spatial and temporal validity. Therefore, the calculations must be constrained in time and space to be correct in accordance with the size of the normal neighborhood patch.

n - Normal Incidence

Normal incidence is given when the direction of propagation of a plane wave is perpendicular to a plane surface, i.e. the angle of incidence is zero.

p - Perturbative

The propagator for an interacting field theory is typically derived considering finite orders in a perturbative calculation with the interaction strength as the smallness parameter.

r - Long Time Restriction

When describing scattering experiments, it is often convenient to choose a large time difference between the initial setup and the measurement. This usually makes it possible to describe the initial and final states in a non-interacting setup, which simplifies calculations.

s - Small Angle Approximation - Near Normal Incidence

Restricting the setup to the case of near normal incidence simplifies the calculations by allowing the incidence angle of a plane wave to be considered as a smallness parameter.

v - Vacuum Space-Times

Vacuum spacetimes are a group of spacetimes for which the Ricci scalar and the Ricci tensor vanish, making certain calculations easier. Since the geometry we are interested in is that of a thin shell and the interior and exterior are vacuum spacetimes, we use this simplifying constraint whenever it is worth doing so.

t - Time Average

To eliminate the oscillatory contribution to an expression, one integrates over one period of the harmonic part and divide by the period time.

B. Dark Matter Jets of Kerr Black-Holes

In this Appendix we summarize the investigation of dark matter jets of rotating black-holes in collaboration with Ottavia Balducci [131]. Dark matter particle decay and annihilation into Standard Model particles provide the most direct way to discover properties of dark matter. Some recent experiments have produced encouraging findings in this regard [132–136]. Of course, we do not know if the observed signals are indeed caused by dark matter particles, but it is an intriguing hypothesis.

The WIMP effective cross section is a typical effective cross section for the annihilation of dark matter particles, however it is too small to explain the measured fluxes of dark matter annihilation products. To explain the observations potentially connect to dark matter, a boost factor B, often of the order of $10^2 - 10^4$, is introduced to dark matter models [137–141]. Various causes for the needed dark matter overdensity are suggested, such as density inhomogeneity on small scales [142] or Sommerfeld enhanced annihilation cross sections [143]. B is defined for an entering dark matter particle beam that annihilates certain target dark matter particles by

$$B = \frac{\rho_B}{\rho_0}\frac{\rho_T}{\rho_0} \tag{B.1}_{\mathcal{G}}$$

where ρ_B and ρ_T are the densities of the beam and the target, respectively, which we normalize with the dark matter density in the solar system ρ_0 [144, 145].

We propose a novel explanation for such dark matter overdensities in our neighborhood by using rotating black-holes. A spinning black-hole forms a dark matter jet that might be directed towards us, resulting in the target dark matter particles being in our local neighborhood and thus $\rho_T/\rho_0 = 1$. The Penrose process underlies jet production and is hence applicable to all massive particles [146]. However, for charged particles, electromagnetic jet production is dominating compared to the gravitational effect, so we are only concerned with neutral particles such as WIMPs.

As a starting point, we study galaxies with a spinning Kerr black-hole at their core. Particles that follow geodesics from the accretion disk into the black-hole may collide

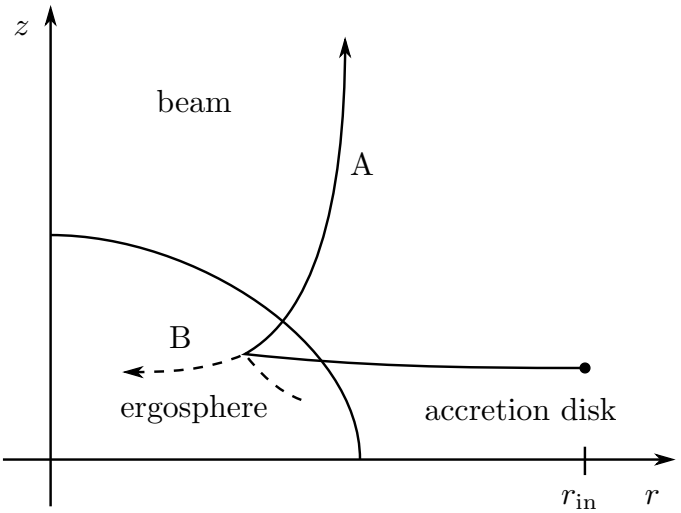

Figure B.1.: A typical geodesic in a Kerr spacetime is presented schematically, which is relevant for dark matter jet production. The solid line depicts a geodesic of particle A traveling from the accretion disk into the black-hole, where it scatters off particle B. Particle A then escapes the black-hole and proceeds parallel to the rotation axis, whereas particle B falls into the black-hole's singularity.

with other particles in the black-hole ergosphere. According to [146], due to the Penrose process, some of these particles may subsequently follow a geodesic heading out of the ergosphere and traveling parallel to the axis of rotation, as illustrated in Fig. B.1. Collecting all geodesics of this type, the black-hole generates a dark matter jet along its rotating axis. The strength of this process determines whether or not an overdensity of dark matter may be observed within the jet. Since the particles in the jet take up very little volume compare to those in the accretion disk, the density in the jet can theoretically be much higher.

To get a quantitative estimate of the dark matter density in the jet, we use the Kerr metric of a black-hole with mass M and angular momentum Ma. The motion of a particle in this background is dictated by the constants of motion, which are the particle's mass, energy, angular momentum, and the Carter constant which reads

$$Q = (u_\theta)^2 + a^2 \cos^2(\theta)\left(1 - E^2\right) + \frac{\cos^2(\theta)}{\sin^2(\theta)} L^2 \,, \tag{B.2}_{\mathcal{G}}$$

where u, E and L are the particle's corresponding proper velocity, total energy, and angular momentum. Using the constants of motion and the dark matter particle's initial position and velocity, we can calculate its final position and velocity, and thus whether it contributes to jet formation.

We determine the boost function to investigate the overdensity created by these geodesics

along the rotation axis,

$$B(\mathbf{x}) = \frac{\rho_{\text{out}}(\mathbf{x})}{\rho_0(\mathbf{x})} \,. \tag{B.3}_{\mathcal{G}}$$

The density of the outgoing particles ρ_{out} inside the dark matter jet is calculated by integrating over all outgoing velocities $\mathbf{v}_{\text{out}}$,

$$\rho_{\text{out}}(\mathbf{x}) = \int \frac{\mathrm{d}^3\mathbf{v}_{\text{out}}}{V_{\text{out}}(\mathbf{x}, \mathbf{v}_{\text{out}})} \frac{\mathrm{d}N_{\text{out}}}{\mathrm{d}\mathbf{v}_{\text{out}}}(\mathbf{x}, \mathbf{v}_{\text{out}}) \,, \tag{B.4}_{\mathcal{G}}$$

with the number of particles in the beam $N_{\text{out}}(\mathbf{x}, \mathbf{v}_{\text{out}})$ at $\mathbf{x}$ with velocity $\mathbf{v}_{\text{out}}$ occupying the volume $V_{\text{out}}(\mathbf{x}, \mathbf{v}_{\text{out}}) = r_{\text{out}}^2 \sin(\theta) v_{r,\text{out}}$. The number of outgoing particles, N_{out}, is given by the number of particles falling into the ergosphere and filtering out all of those that follow paths that do not end up in the beam. Explicitly, it is obtained with

$$N_{\text{out}}(\mathbf{x}, \mathbf{v}_{\text{out}}) = \eta P_{\text{scat}} \int \mathrm{d}^3\mathbf{v}_{\text{in}} f(\mathbf{v}_{\text{in}}) \rho_{\text{in}} V_{\text{in}}(\mathbf{x}, \mathbf{v}_{\text{in}}, \mathbf{v}_{\text{out}}) \,. \tag{B.5}_{\mathcal{G}}$$

The volume occupied by particles with initial velocities of $\mathbf{v}_{\text{in}} = (v_r, v_\phi, v_\theta)$ that reach at $\mathbf{x}$ in the jet with final velocity $\mathbf{v}_{\text{out}}$ is denoted by V_{in}. The incident particle density is specified by ρ_{in}, and the velocity distribution function is provided by $f(\mathbf{v}_{\text{in}})$. The prefactor consists of the efficiency of the Penrose process η and the probability P_{scat} that an incoming particle is scattered in the ergosphere and not before in the accretion disk. In the next section, we will introduce approximations to simplify (B.4) allowing to numerically compute the boost function (B.3).

Approximations and Assumptions

In order to numerically compute (B.4) for the specific galaxy in question, we systematically simplify (B.4) using various approximations and assumptions in this section.

Volume of infalling particles:

The volume occupied by the incoming particles is described as a ring with radius r_{in}, height $\Delta z = z_{\max} - z_{\min}$, and width $v_r \Delta t$, such that it reads $V_{\text{in}}(\mathbf{x}, \mathbf{v}_{\text{in}}, \mathbf{v}_{\text{out}}) = 2\pi r_{\text{in}} v_{\text{r}} \Delta t \Delta z(\mathbf{x}, \mathbf{v}_{\text{in}}, \mathbf{v}_{\text{out}})$. A more precise method would start by tracing particles in the jet with known velocities back to the ergosphere and accretion disk during a specific time period. All relevant geodesics like the one depicted in Fig. B.1 may then be gathered and utilized to calculate how many particles from the accretion disk finally end up in the jet. To substantially cut calculation time, we approximate this technique with an incident ring. There are various competing effects in this scenario, such as a bigger radius implying a larger volume but also a lower dark matter density. As a result, there is an

area in the accretion disk where the majority of the particles relevant to jet formation are produced. The most relevant geodesics are collected by suitably selecting $r_{\rm in}$ inside this region. To get an upper bound, we pick $r_{\rm in}$ so that we get the highest boost factor. For the Andromeda galaxy this is 0.1 pc.

Carter constant:

As in [146], we assume the scattering in the ergosphere has no effect on the value of the Carter constant and that particles with the correct value of the Carter constant $Q_{\rm out}$ end up in the jet and do not follow any other geodesic with the same value. We determine the starting position that the particles must have in order to end up in the beam at $\mathbf{x}$ by holding all other parameters constant and solving $Q_{\rm in} = Q_{\rm out}$ for $z\left(\mathbf{x}, \mathbf{v}_{\rm in}, \mathbf{v}_{\rm out}\right)$. There does not exist a geodesic if this equation has no solution for a given set of parameters.

Distribution function:

The velocity distributions of the infalling particles are assumed to be Gaussian,

$$f\left(\mathbf{v}_{\rm in}\right) := \frac{\exp\left\{-\frac{1}{2}(\mathbf{v}_{\rm in}-\mathbf{v}_0)^T\Sigma^{-1}(\mathbf{v}_{\rm in}-\mathbf{v}_0)\right\}}{\sqrt{(2\pi)^3|\det(\Sigma)|}}\,. \tag{B.6}_{\mathcal{G}}$$

To keep the model simple, we assume that the covariance matrix is diagonal and isotropic such that $\Sigma = \mathrm{diag}(\sigma^2, \sigma^2, \sigma^2)$, and assume that the dark matter particles follows a stable orbit with $\mathbf{v}_0 = (0, 0, v_{\phi,0})$. The orbit velocity $v_{\phi,0}$ is extracted from the data on the Milky Way rotation curves in [147]. We utilize Fig. 2 from [148] to compute the mass accretion rate $\mathrm{d}M/\mathrm{d}t$ of supermassive black-holes. With this accretion rate we determine the standard deviation σ by equating it with the particle infall rate near the black-hole and numerically solving this equation for σ,

$$\frac{\mathrm{d}M}{\mathrm{d}t} = 4\pi r_{\rm in}^2 \rho_{\rm in} \int_0^1 \mathrm{d}v_r \frac{1}{\sqrt{2\pi\sigma^2}} e^{-\frac{v_r^2}{2\sigma^2}} v_r\,. \tag{B.7}_{\mathcal{G}}$$

The dark matter density in the accretion disk may then be approximated as $\rho_{\rm in}\left(0.1\,\mathrm{pc}\right) = 30\rho_0$ for the Andromeda galaxy at $r_{\rm in} = 0.1\,\mathrm{pc}$ with a cored dark matter profile [149].

Penrose efficiency:

The Penrose process' efficiency is depends solely on the black-hole's angular momentum, and for extreme black-holes, it may reach a maximum of 0.52 [150]. We assume a Penrose efficiency of $\eta = 0.01$ since the angular momentum of the black-holes in the galaxies' cores is unknown.

Mean free path:

Since we follow the dark matter particles along a single geodesic, we must account for the possibility of scattering with other dark matter particles in the accretion disk. To do so, we use the particles' mean free path and assume that just one scattering event happens

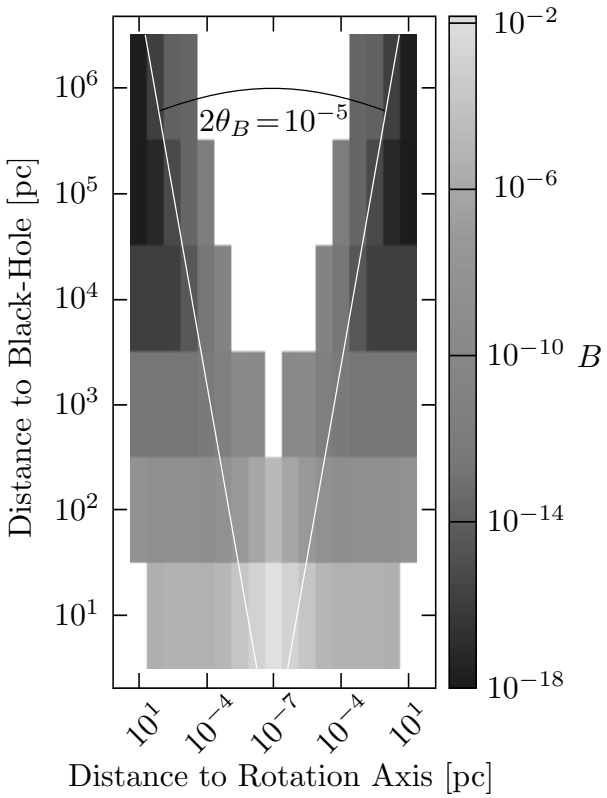

Figure B.2.: Dark matter boost function B in the beam is given for different distances from the black-hole and the rotation axis. With white lines the opening angle of the beam $2\theta_B$ is indicated schematically. There is no data for the white pixels due to the in-applicability of our estimations.

on average within the ergosphere. We derive $P_{\text{scat}} = \lambda_{\text{mfp}}/r_{\text{in}} \approx 2M/r_{\text{in}}$ by considering that the dark matter density does not vary significantly along the geodesic.

Results

The dark matter density produced by a dark matter beam from a black-hole is now quantitatively calculated using these approximations. We do this by performing a Riemann sum over the dark matter particles' initial velocities in (B.5). In this procedure, the integration limits and step size are numerically changed to take advantage of the sweet spot between accuracy and calculation time, as described in our supplied code [131]. Moreover, there is a lower boundary constraint on the outgoing radial velocity, because the particles arriving today had to be expelled away from the black-hole at earliest during its creation, thus $v_{r,\text{out}} > r_{\text{out}}/t_{\text{age}}$ with the black-hole's age t_{age}.

As a first example, we consider the black-hole in the center of the Andromeda galaxy. Its rotation axis is oriented toward the solar system, allowing us to compute the dark matter overdensity caused by the dark matter ray in our local neighborhood. Assuming

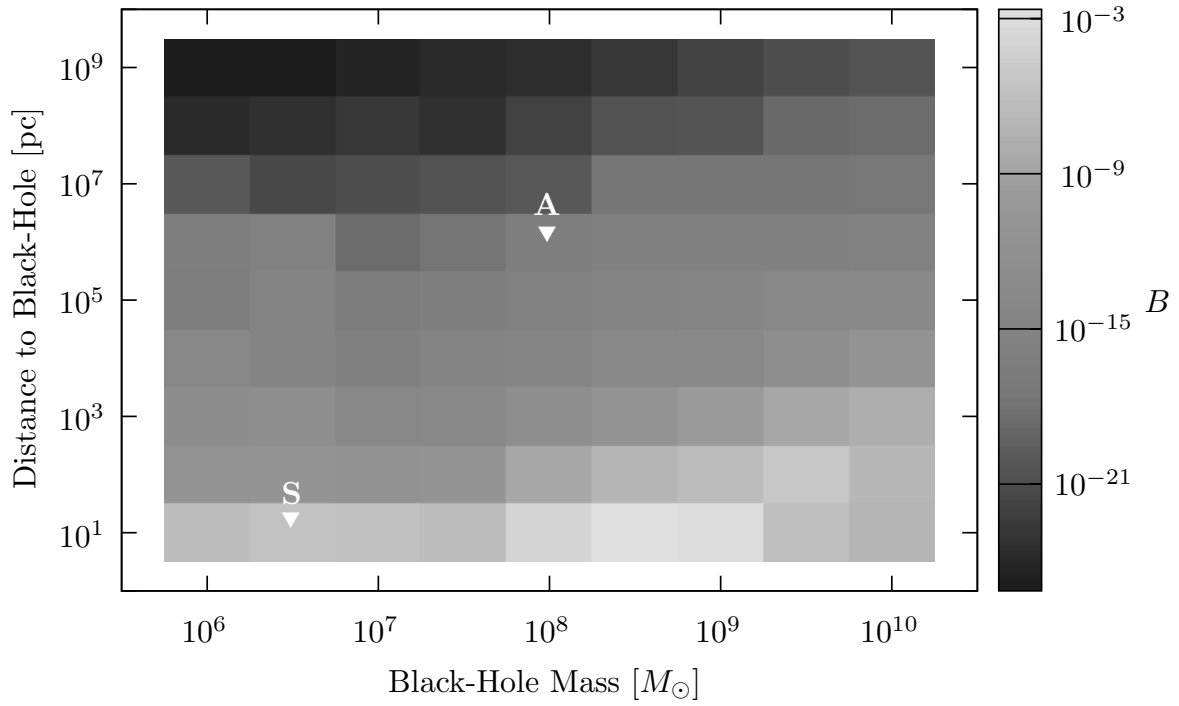

Figure B.3.: The boost factor B of a DM beam at different distances from the black-hole r_{out} and masses M is shown for $\theta = 10^{-8}$. The mass range covers both smaller black-holes found in galactic centers and the biggest black-holes ever observed. The symbols A and S represent the two cases addressed in the text, Andromeda and Sagittarius A*.

that the age of the black-hole is the same as the age of the galaxy, $t_{\text{age}} = 10^{10}\,\text{yrs}$, the dark matter boost function in the solar system $B \approx 10^{-12}$. Although this is the most promising candidate, the overdensity yields a boost factor with $B \ll 1$ and thus cannot explain boost functions of the order 10^4 required to explain indirect dark matter data in the solar system.

The density profile of the Andromeda black-hole's dark matter beam is depicted in Fig. B.2. We can infer the following conclusions from this result. To begin, the beam is substantially collimated with an aperture angle of $2\theta_B \approx 10^{-5}$. Furthermore, the beam's range allows it to be distinguished from the background even at a distance of 1 Mpc. Finally, as one approaches the black-hole and its axis of rotation, the dark matter density of the jet grows by several orders of magnitude. Despite of this increase, it never achieves a considerable overdensity. Based on these observations, we may conclude that the Andromeda black-hole is capable of emitting a sharp, long-range, but faint dark matter beam.

To learn more about this dark matter beam, we examined its qualitative behavior for various values of the black-hole's angular momentum a. We find that the dark matter density of a Schwarzschild black-hole, $a = 0$, is 8 orders of magnitude lower than that of a $a = M/2$ [131]. Geodesics reaching the target location without any Kerr phenomena asso-

ciated with rotating black-holes, such as the Penrose process, account for this background contribution. Since this contribution is minimal in comparison to the dark matter density in the beam for rotating black-holes, the dark matter beam is substantially produced by Kerr metric effects. Furthermore, the bigger the a value, the more collimated is the dark matter beam [131], in accordance with intuition.

In Fig. B.3, we plot the boost factor as a function of the black-hole mass and the distance to the black-hole, allowing us to examine many different astrophysical black-holes. To investigate an interesting possibility, we take the black-hole Sagittarius A* in the center of the Milky Way and calculate the boost function at a distance of 10 pc. Observing the annihilation or decay products in this region, which is so close to a black-hole, could open up new opportunities for the indirect detection of dark matter in the vicinity of black-holes. However, as shown in Fig. B.3, the boost factor for Sagittarius A* even that close to it is so small that further investigation in this direction is not justified. From Fig. B.3 we extract an ideal boost function for lower distances and masses in the $10^8\,M_\odot$ to $10^9\,M_\odot$ range, with a maximum boost of $B_{\max} \approx 40$. This dark matter overdensity, however, is still much too low for indirect dark matter observations. In this regard, we summarize that dark matter jets are formed by rotating black-holes, but they are so faint that they do not significantly contribute to dark matter overdensities. Because our investigation of spinning black-hole effects connected with dark matter was only the first step in this field, we expect that owing to its unique characteristics, this area of dark matter overdensity sources will get more attention in the future.

C. Mass Insertion

The procedure of mass insertion shows in an illuminating way how a kinetic term in the action can be considered as an interaction term. Thus it serves as a guide for the perturbative approach finding the propagator across interfaces in Sec. 2.2. To this end, we restate the mass insertion as treated, for example, in [63] and carefully analyze its properties.

The Feynman propagator of massless scalar fields ϕ interacting due to the mass term in the action can be calculated analogously to (2.37) and is

$$\Delta^m_{xy} = i \left\langle T\phi_x\phi_y \exp\left\{-\frac{i}{2}\int \mathrm{d}\mu_z\, m^2\phi_z^2\right\}\right\rangle_{\mathcal{HS}}. \tag{C.1}$$

Expanding the exponential and contracting the fields we find the series

$$\begin{aligned}\Delta^m_{xy} &= -\int \frac{\mathrm{d}^4\mathrm{k}}{(2\pi)^4}\frac{e^{-ik(x-y)}}{k^2-i\epsilon}\left(1-\frac{m^2}{k^2-i\epsilon}+\left(\frac{m^2}{k^2-i\epsilon}\right)^2+\cdots\right)\\ &= -\int \frac{\mathrm{d}^4\mathrm{k}}{(2\pi)^4}\frac{e^{-ik(x-y)}}{k^2+m^2-i\epsilon},\end{aligned} \tag{C.2}_{\mathcal{HS}}$$

where we used the Geometric Series in the last step. The result is the massive propagator, which we would also have obtained by solving the fundamental equation of the propagator for massive fields. This is the well-known method of mass insertion, which we will now analyze in more detail.

Performing the k_0 integration of the massive propagator yields

$$\Delta^m_{xy} = \Theta_{x^ty^t}G^m_{xy} + \Theta_{y^tx^t}G^m_{yx}, \tag{C.3}_{\mathcal{HS}}$$

with the Wightman distributions of massive scalar fields

$$G^m_{xy} := i\int \frac{\mathrm{d}^3k}{(2\pi)^3 2\omega^m_k} e^{-i\omega^m_k(x^t-y^t)}e^{i\mathbf{k}(\mathbf{x}-\mathbf{y})}, \tag{C.4}_{\mathcal{HS}}$$

together with the dispersion relation $(\omega^m_k)^2 = \mathbf{k}^2 + m^2$. Let us first check whether instead of the whole propagator we can derive the massive Wightman distributions with the mass

insertion procedure. The first non-trivial contribution to a potential massive Wightman distribution is given by

$$\begin{aligned} i\int_z G_{xz}\, m^2 G_{zy} &= -im^2 \int \frac{\mathrm{d}^3k}{(2\pi)^3 2\omega_k}\frac{\mathrm{d}^3q}{2\omega_q} e^{-i(\omega_q x^t+\omega_k y^t)} e^{i(\mathbf{kx}-\mathbf{qy})}\delta(\omega_q-\omega_k)\delta^{(3)}(\mathbf{q}-\mathbf{k}) \\ &= -im^2 \int \frac{\mathrm{d}^3k}{(2\pi)^3 4\omega_k^2} e^{-i\omega_k(x^t-y^t)} e^{i\mathbf{k}(\mathbf{x}-\mathbf{y})}\delta(0)\,, \end{aligned} \tag{C.5}_{\mathcal{HS}}$$

where $G_{xy} = G^m_{xy}\big|_{m=0}$. Performing the k_0 integration of the corresponding term in Eq. (C.2) and projecting it onto the positive frequency contribution, we obtain instead

$$\begin{aligned} &\Theta_{x^t y^t}\int \frac{\mathrm{d}^4k}{(2\pi)^4}\frac{e^{-ik(x-y)}}{k^2-i\epsilon}\frac{m^2}{k^2-i\epsilon} \\ &\qquad = -im^2\Theta_{x^t y^t}\int \frac{\mathrm{d}^3k}{(2\pi)^3 4\omega_k^2} e^{-i\omega_k(x^t-y^t)} e^{i\mathbf{k}(\mathbf{x}-\mathbf{y})}\left(x^t-y^t-\frac{i}{\omega_k}\right). \end{aligned} \tag{C.6}_{\mathcal{HS}}$$

For $x^t-y^t\to\infty$ this expression also diverges. Taking in (C.5) also the finite time interval x^t-y^t, the diverging $\delta(0)$ is replaced by x^t-y^t and apart from the Heaviside step function agrees with the first two terms in (C.6).

The missing Heaviside step function together with the restricted z^t integration can be introduced with the correct combination of Heaviside step functions for the Wightman distributions,

$$i\int_z \Theta_{x^t z^t} G_{xz}\, m^2 \Theta_{z^t y^t} G_{zy} = -im^2\Theta_{x^t y^t}\int \frac{\mathrm{d}^3k}{(2\pi)^3 4\omega_k^2} e^{-i\omega_k(x^t-y^t)} e^{i\mathbf{k}(\mathbf{x}-\mathbf{y})}(x^t-y^t)\,. \tag{C.7}_{\mathcal{HS}}$$

This expression is the outcome of the k_0 integration in (C.1). This, however, generates the following contribution as well,

$$i\Theta_{x^t y^t}\int_z \Theta_{x^t z^t} G_{xz}\, m^2 \Theta_{y^t z^t} G_{yz} = im^2\Theta_{x^t y^t}\int \frac{\mathrm{d}^3k}{(2\pi)^3 4\omega_k^2} e^{-i\omega_k(x^t-y^t)} e^{i\mathbf{k}(\mathbf{x}-\mathbf{y})}\frac{i}{\omega_k}\,. \tag{C.8}_{\mathcal{HS}}$$

Both contributions (C.7) and (C.8) together yield (C.6), as expected, since we only changed the order of integration over z and k_0. This shows that we cannot find the massive Wightman distributions simply by gluing together massless Wightman distributions, since crucial contributions such as (C.8) would not be considered. This instructive example demonstrates, that the computation of a propagator in an interacting theory with (C.1) must be performed with the free propagators.

D. RNC Size Quantum Experiment

This Appendix is about an error analysis for the systems we study in Sec. 4.3.2. Since this system uses a normal neighborhood in the exterior of the shell, we start with the domain of validity discussed in Sec. 3.1.3. The minimum Schwarzschild radius that can be described with the considered RNC patch anchored at the expansion radius r_0 is given by (3.38). The expansion point used in (3.73) has a maximum radius of $r_0 = 5/4R$ for $R \to r_g$. We demand that the Minkowski patch reaches the fixed shell with radius $r_{\min} = R$ and obtain with Eq. (3.38) a maximal error of $\delta \approx 5 \times 10^{-2}$, which is sufficient.

For the application in question, we need the propagator of a scalar field in the RNC patch as derived in Sec. 3.1.1. As can be seen, for example in (3.17), the adiabatic expansion of the metric amounts for the propagator to a large momentum expansion. Therefore, the RNC propagator for a finite adiabatic order is not trustworthy if the momentum is too small or the wavelength too large, i.e., on the order of the curvature length scale. We circumvent this problem by introducing an infrared energy cutoff ω_{IR}. We demand that the error due to neglecting the curvature terms affects the result by at most one percent which requires the cutoff to be $\omega_{\mathrm{IR}} \approx 4\sqrt{r_g/2}/(r_0)^{3/2}$.

To avoid any dependence on the exact value of ω_{IR}, we only study observables that are not infrared sensitive. For example, in applications with external sources J, we can choose J such that the contribution from infrared physics is negligible. In Sec. 4.3.2 we use the source (4.57) that has a Gaussian dependence in energy space, and thus we must choose the standard deviation σ_t and the mean $\langle \omega_k \rangle$ such that the observable in question does not depend on ω_{IR}. In addition, for a chosen σ_t, we must ensure that the temporal validity of the system under consideration is large enough. The temporal validity of a RNC patch given by Eq. (3.37) depends on the mass of the black-hole. Taking $\delta = 10^{-2}$ as before, a Minkowski patch anchored at r_0 yields a time restriction of $|x^t| < t_{\max}(R) = 0.16\, r_0^{3/2}\sqrt{f(R)}/[r_g f(r_0)]$. Since in Sec. 4.3.2 we use this source for different values of R and $t_{\max}$ increases monotonically for $R > r_g$, we choose the most restrictive radius for which the shell can be stabilized, i.e., $R \to 25r_g/24$. Taking r_0 as in (3.73), we obtain $\sigma_t = t_{\max}(25r_g/24)/2 \approx 0.08 r_g$ and $\langle \omega_k \rangle = 4/\sigma_t$ such that the cutoff ω_{IR} is not relevant. For astrophysical black-holes with masses ranging from one to 10^{11} solar masses, the validity in time ranges from $t_{\max} = 1\,\mu\mathrm{s}$ to $t_{\max} = 40\,\mathrm{h}$ in SI units.

Now that the temporal constraint on the external source is established, only the spatial restriction needs to be examined. The source in Sec. 4.3.2 is a point source located inside the shell at $\mathbf{x}_J$. This point must be taken sufficiently close to the surface of the shell such that it can be approximated as flat. We require that the error introduced by this approximation be of the order of 10^{-2}. A geometric consideration then provides that the distance between the shell and the source is constrained to be $R - x_J^{\perp} < 0.1R$.

Acknowledgements – Danksagung

Die vorliegende Arbeit ist keineswegs eine Einzelleistung. Sie ist das Ergebnis einer langen Reise mit vielen Begegnungen, die diese Arbeit formten und ermöglichten.

An erster Stelle möchte ich Dir, Stefan, meinen tiefsten Dank aussprechen. Mit Deiner leidenschaftlichen Hingabe zur theoretischen Physik und Deinem einzigartigen Charakter hast Du meine Forschung und diese Arbeit geprägt wie kein anderer. Die unzähligen Gespräche, sowohl über unsere gemeinsamen Projekte als auch über Gott und die Welt haben mich zu dem Wissenschaftler und weltoffenen Geist werden lassen, der ich heute bin. Großen Menschen gebührt großer Dank, vielen vielen Dank!

Jörg Schreiber danke ich für die langjährige moralische und beratende Unterstützung. Unsere unzähligen Gespräche waren mir jederzeit eine wertvolle Hilfe.

Für administrative und florale Fragen erhielt ich jederzeit Unterstützung von der guten Seele des Stockwerks, der Herta Wiesbeck-Yonis, wofür ich ihr recht herzlich danke.

Große Teile der Arbeit sind entscheidend geprägt durch gemeinsame Forschungsprojekte mit meinen Kollaboratoren Florian Niedermann, Ka Hei Choi, Cecilia Giavoni, Marc Schneider, Ottavia Balducci, Tehseen Rug, Lukas Gründing, Bruno Högl, Patricia Ribes Metidieri, Maximilian Urban, Alexis Kassiteridis, Thomas Steingasser und Ivana Babic. Vielen Dank für die großartige Zusammenarbeit.

Allen Mitgliedern des Prüfungskomitees danke ich für die Teilnahme und wünsche viel Vergnügen: Stefan Hofmann, Gerhard Buchalla, Jörg Schreiber und Harald Weinfurter.

For inspiring and instructive conversations at conferences, I would like to thank in particular Bill Unruh, Bob Wald, Viacheslav Emelyanov and Piero Nicolini.

Besonderer Dank gilt Ka Hei Choi, Cecilia Giavoni, Marc Schneider und Maximilian Urban für das Probelesen dieser Arbeit.

Für eine bunte und abwechslungsreiche Atmosphäre am Arnold-Sommerfeld-Center danke ich chronologisch meinen Kollegen: Tehseen Rug, Lukas Gründing, Daniel Flassig, Ottavia Balducci, Andreas Wegscheider, Marc Schneider, Alexis Kassiteridis, David Licht, Marin Ferara, Alexander Gussmann, Leila Mirzagholi, Sebastian Konopka, Katrin Hammer, Florian Niedermann, Stephen Brennan, Christoph Chiaffrino, Cecilia Giavoni, Ludwig Eglseer, Maximilian Urban, Thomas Steingasser, Annamaria Hell, Daniel Weiss, Allison Pinto, Jillur Rahman, Bruno Högl, Patrick Hager, Sophie Strobl, Till Heckel-

bacher, Christoph Mueller, Ka Hei Choi, Charlie Mattschas, Patricia Ribes Metidieri und Ivana Babic. Mit Freude sah ich dabei zu, wie Freundschaften entstanden, die auch außerhalb der Wissenschaft Fortbestand haben.

Meiner Familie verdanke ich emotionale Stabilität und Unterstützung, ohne der meine Forschungstätigkeit eines gewesen wäre: Arbeit. Ihr versetzt mein Leben mit den Zutaten, die es schmackhaft und neben der wissenschaftlichen Korrektheit auch magisch machen. Von Herzen vielen lieben Dank dafür Ramona, Gabriele, Detlef, Christian, Sebastian, Alexander, Petra, Killian, Inge, Maria und Elisa.

Bibliography

[1] B.P. Abbott et al. Observation of Gravitational Waves from a Binary Black Hole Merger. *Phys. Rev. Lett.*, 116(6):061102, 2016.

[2] Kazunori Akiyama et al. First M87 Event Horizon Telescope Results. I. The Shadow of the Supermassive Black Hole. *Astrophys. J.*, 875(1):L1, 2019.

[3] Kazunori Akiyama et al. First Sagittarius A* Event Horizon Telescope Results. I. The Shadow of the Supermassive Black Hole in the Center of the Milky Way. *Astrophys. J. Lett.*, 930(2):L12, 2022.

[4] S. W. Hawking. Particle Creation by Black Holes. *Commun. Math. Phys.*, 43:199–220, 1975. [Erratum: Commun.Math.Phys. 46, 206 (1976)].

[5] S.W. Hawking. Breakdown of Predictability in Gravitational Collapse. *Phys. Rev. D*, 14:2460–2473, 1976.

[6] William G. Unruh and Robert M. Wald. Information Loss. *Rept. Prog. Phys.*, 80(9):092002, 2017.

[7] Samir D. Mathur. The Information paradox: A Pedagogical introduction. *Class. Quant. Grav.*, 26:224001, 2009.

[8] Joseph Polchinski. The Black Hole Information Problem. In *Theoretical Advanced Study Institute in Elementary Particle Physics: New Frontiers in Fields and Strings*, pages 353–397, 2017.

[9] Ulrich H. Gerlach. The mechanism of blackbody radiation from an incipient black hole. *Phys. Rev. D*, 14:1479–1508, Sep 1976.

[10] Tanmay Vachaspati, Dejan Stojkovic, and Lawrence M. Krauss. Observation of incipient black holes and the information loss problem. *Phys. Rev. D*, 76:024005, 2007.

[11] Carlos Barcelo, Stefano Liberati, Sebastiano Sonego, and Matt Visser. Fate of gravitational collapse in semiclassical gravity. *Phys. Rev. D*, 77:044032, 2008.

[12] Stefan Hofmann, Maximilian Koegler, and Florian Niedermann. Perturbative quantum consistency near black-hole horizon formation. *Phys. Rev. D*, 104(12):125007, 2021.

[13] Oleg Lunin and Samir D. Mathur. AdS / CFT duality and the black hole information paradox. *Nucl. Phys. B*, 623:342–394, 2002.

[14] Pawel O. Mazur and Emil Mottola. Gravitational condensate stars: An alternative to black holes. 9 2001.

[15] Gia Dvali and Cesar Gomez. Black Hole's Quantum N-Portrait. *Fortsch. Phys.*, 61:742–767, 2013.

[16] Ahmed Almheiri, Donald Marolf, Joseph Polchinski, and James Sully. Black Holes: Complementarity or Firewalls? *JHEP*, 02:062, 2013.

[17] Stefan Hofmann and Tehseen Rug. A Quantum Bound-State Description of Black Holes. *Nucl. Phys. B*, 902:302–325, 2016.

[18] Raphael Bousso. *Black hole entropy and the Bekenstein bound*, pages 139–158. 2020.

[19] Geoff Penington, Stephen H. Shenker, Douglas Stanford, and Zhenbin Yang. Replica wormholes and the black hole interior. 11 2019.

[20] Maximilian Koegler. Space-time geometry of quantum mechanically resolved black holes. 2016.

[21] Don N. Page. Particle Emission Rates from a Black Hole: Massless Particles from an Uncharged, Nonrotating Hole. *Phys. Rev. D*, 13:198–206, 1976.

[22] Steven B. Giddings. Quantization in black hole backgrounds. *Phys. Rev. D*, 76:064027, 2007.

[23] Emil T. Akhmedov, Hadi Godazgar, and Fedor K. Popov. Hawking radiation and secularly growing loop corrections. *Phys. Rev. D*, 93(2):024029, 2016.

[24] C.P. Burgess, Joshua Hainge, Greg Kaplanek, and Markus Rummel. Failure of Perturbation Theory Near Horizons: the Rindler Example. *JHEP*, 10:122, 2018.

[25] Wojciech H. Zurek. Decoherence and the transition from quantum to classical. *Phys. Today*, 44N10:36–44, 1991.

[26] David Polarski and Alexei A. Starobinsky. Semiclassicality and decoherence of cosmological perturbations. *Class. Quant. Grav.*, 13:377–392, 1996.

[27] Angelo Bassi, André Großardt, and Hendrik Ulbricht. Gravitational Decoherence. *Class. Quant. Grav.*, 34(19):193002, 2017.

[28] Roseanne M. Cheng and Charles R. Evans. Relativistic effects in the tidal interaction between a white dwarf and a massive black hole in Fermi normal coordinates. *Phys. Rev.*, D 87(10):104010, 2013.

[29] Michael Kesden. Tidal disruption rate of stars by spinning supermassive black holes. *Phys. Rev.*, D 85:024037, 2012.

[30] T. S. Bunch and Leonard Parker. Feynman propagator in curved spacetime: A momentum-space representation. *Phys. Rev. D*, 20:2499–2510, Nov 1979.

[31] Leonard Parker. One-electron atom as a probe of spacetime curvature. *Phys. Rev.*, D 22:1922–1934, Oct 1980.

[32] Dario Bettoni, Jose María Ezquiaga, Kurt Hinterbichler, and Miguel Zumalacárregui. Speed of gravitational waves and the fate of scalar-tensor gravity. *Phys. Rev.*, D 95:084029, Apr 2017.

[33] Pablo Bueno, Vincent S. Min, Antony J. Speranza, and Manus R. Visser. Entanglement equilibrium for higher order gravity. *Phys. Rev.*, D 95:046003, Feb 2017.

[34] Pavel Castro-Villarreal. Brownian motion meets riemann curvature. *J. Stat. Mech.*, 2010(08):P08006, aug 2010.

[35] Uwe Muller, Christian Schubert, and Anton M. E. van de Ven. A Closed formula for the Riemann normal coordinate expansion. *Gen. Relativ. Gravit.*, 31:1759–1768, 1999.

[36] Bruno Hoegl, Stefan Hofmann, and Maximilian Koegler. Physics in Precision-Dependent Normal Neighborhoods. *Phys. Rev. D*, 102(8):084065, 2020.

[37] Maximilian Koegler and Marc Schneider. Vacuum Induced Ground-State Instabilities. 2022. Manuscript in preparation.

[38] Ka Hei Choi, Stefan Hofmann, and Maximilian Koegler. Non-Unitary Evolution of Instantaneous Vacuum States in Conformal FLRW Spacetimes. 2022. Manuscript in preparation.

[39] Cecilia Giavoni, Stefan Hofmann, and Maximilian Koegler. Quantum graphs as a beacon for quantum field theory in curved spacetime. 2022. Manuscript in preparation.

[40] Matthew D. Schwartz. *Quantum Field Theory and the Standard Model*. Cambridge University Press, 3 2014.

[41] Ka Hei Choi. Scattering properties of a scalar field in an analogical gravitational collapse model. 2019.

[42] Patrick Hager. Smooth interface geometries and unitarity in curved space-times. 2019.

[43] Albert Einstein. Über das Relativitätsprinzip und die aus demselben gezogene Folgerungen. (German) [On the Relativity Principle and the conclusions drawn from it]. *Jahrb. Radioakt. Elektron.*, 5:98–99, 1907.

[44] Aleksej Z. Petrov. *Einstein Spaces*. 1969.

[45] S. Kobayashi and K. Nomizu. *Foundations of Differential Geometry, Volume 1*. A Wiley Publication in Applied Statistics. Wiley, New York, 1996.

[46] R. Penrose and R. M. Floyd. Extraction of rotational energy from a black hole. *Nature*, 229:177–179, 1971.

[47] J. R. Oppenheimer and H. Snyder. On continued gravitational contraction. *Phys. Rev.*, 56:455–459, Sep 1939.

[48] G. D. Birkhoff. *Relativity and Modern Physics*, volume 23008297. Harvard University Press, 1923.

[49] A. Hosoya Y. Kanai, M. Siino. Gravitational collapse in Painlevé-Gullstrand coordinates.

[50] F. K. Manasse and C. W. Misner. Fermi Normal Coordinates and Some Basic Concepts in Differential Geometry. *J. Math. Phys. (N.Y.)*, 4:735–745, 1963.

[51] Wann-Quan Li and Wei-Tou Ni. Expansions of the affinity, metric and geodesic equations in fermi normal coordinates about a geodesic. *J. Math. Phys. (N.Y.)*, 20(9):1925–1929, 1979.

[52] Alexander I. Nesterov. Riemann normal coordinates, Fermi reference system and the geodesic deviation equation. *Classical Quantum Gravity*, 16:465–477, 1999.

[53] C. Chicone and B. Mashhoon. Explicit fermi coordinates and tidal dynamics in de sitter and gödel spacetimes. *Phys. Rev.*, D 74:064019, Sep 2006.

[54] Bruno Hoegl, Stefan Hofmann, and Maximilian Koegler. Physics in Precision-Dependent Normal Neighborhoods. https://doi.org/10.5281/zenodo.3966891. July 2020.

[55] Valerio Faraoni. *Cosmological and Black Hole Apparent Horizons*, volume 907. 2015.

[56] W. Israel. Singular hypersurfaces and thin shells in general relativity. *Nuovo Cim. B*, 44:1, 1966. [Erratum: Nuovo Cim.B 48, 463 (1967)].

[57] Bryce S. DeWitt. Quantum theory of gravity. i. the canonical theory. *Phys. Rev.*, 160:1113–1148, Aug 1967.

[58] H. P. Breuer and F. Petruccione. *The theory of open quantum systems*. 2002.

[59] Angel Rivas and Susana F Huelga. *Open quantum systems*, volume 10. Springer, 2012.

[60] Andrzej Kossakowski. On quantum statistical mechanics of non-hamiltonian systems. *Reports on Mathematical Physics*, 3(4):247–274, 1972.

[61] Stefan Hofmann and Marc Schneider. Classical versus quantum completeness. *Phys. Rev. D*, 91(12):125028, 2015.

[62] B. Hatfield. *Quantum Field Theory Of Point Particles And Strings*. Frontiers in Physics. Avalon Publishing, 1998.

[63] Matthew D. Schwartz. *Quantum Field Theory and the Standard Model*. Cambridge University Press, 3 2014.

[64] A. Ashtekar and A. Magnon-Ashtekar. A GEOMETRICAL APPROACH TO EXTERNAL POTENTIAL PROBLEMS IN QUANTUM FIELD THEORY. *Gen. Rel. Grav.*, 12:205–223, 1980.

[65] Abhay Ashtekar, Tommaso De Lorenzo, and Marc Schneider. Probing the Big Bang with quantum fields. *Adv. Theor. Math. Phys.*, 25:7, 2021.

[66] Robert M. Wald. *Quantum Field Theory in Curved Space-Time and Black Hole Thermodynamics*. Chicago Lectures in Physics. University of Chicago Press, Chicago, IL, 1995.

[67] Alejandro Corichi, Jeronimo Cortez, and Hernando Quevedo. On the relation between Fock and Schrodinger representations for a scalar field. *Annals Phys.*, 313:446–478, 2004.

[68] N. D. Birrell and P. C. W. Davies. Quantum Fields in Curved Space. *Cambridge Univ. Press*, 2, 1984.

[69] Alejandro Corichi, Jeronimo Cortez, and Hernando Quevedo. On the Schrodinger representation for a scalar field on curved space-time. *Phys. Rev. D*, 66:085025, 2002.

[70] Ivan Agullo, William Nelson, and Abhay Ashtekar. Preferred instantaneous vacuum for linear scalar fields in cosmological space-times. *Phys. Rev. D*, 91:064051, 2015.

[71] D. J. Toms L. E. Parker. Quantum Field Theory in Curved Spacetime. *Cambridge University Press*, page 136, 2009.

[72] T. S. Bunch and P. C. W. Davies. Quantum Field Theory in de Sitter Space: Renormalization by Point Splitting. *Proc. Roy. Soc. Lond. A*, 360:117–134, 1978.

[73] S. A. Fulling, M. Sweeny, and Robert M. Wald. Singularity Structure of the Two Point Function in Quantum Field Theory in Curved Space-Time. *Commun. Math. Phys.*, 63:257–264, 1978.

[74] S. A. Fulling, F. J. Narcowich, and Robert M. Wald. Singularity Structure of the Two Point Function in Quantum Field Theory in Curved Space-time. II. *Annals Phys.*, 136:243–272, 1981.

[75] Valter Moretti. Comments on the stress energy tensor operator in curved space-time. *Commun. Math. Phys.*, 232:189–221, 2003.

[76] Stefan Hofmann, Marc Schneider, and Maximilian Urban. Quantum complete prelude to inflation. *Phys. Rev. D*, 99(6):065012, 2019.

[77] Allan Adams, Nima Arkani-Hamed, Sergei Dubovsky, Alberto Nicolis, and Riccardo Rattazzi. Causality, analyticity and an IR obstruction to UV completion. *JHEP*, 10:014, 2006.

[78] Nima Arkani-Hamed, Tzu-Chen Huang, and Yu-Tin Huang. The EFT-Hedron. *JHEP*, 05:259, 2021.

[79] Reinaldo de Melo e Souza, François Impens, and Paulo A Maia Neto. Microscopic dynamical casimir effect. *Physical Review A*, 97(3):032514, 2018.

[80] Paul Hoyer. Born Level Bound States. *Few Body Syst.*, 58(3):128, 2017.

[81] E.A. Uehling. Polarization effects in the positron theory. *Phys. Rev.*, 48:55–63, 1935.

[82] P. A. M. Dirac. Discussion of the infinite distribution of electrons in the theory of the positron. *Mathematical Proceedings of the Cambridge Philosophical Society*, 30(2):150?163, 1934.

[83] Werner Heisenberg. Bemerkungen zur diracschen theorie des positrons. In *Original Scientific Papers/Wissenschaftliche Originalarbeiten*, pages 132–154. Springer, 1989.

[84] Jochen Zahn. The renormalized locally covariant dirac field. *Reviews in Mathematical Physics*, 26(01):1330012, 2014.

[85] Jochen Zahn. The current density in quantum electrodynamics in time-dependent external potentials and the schwinger effect. *Journal of Physics A: Mathematical and Theoretical*, 48(47):475402, 2015.

[86] Jan Schlemmer and Jochen Zahn. The current density in quantum electrodynamics in external potentials. *Annals of Physics*, 359:31–45, 2015.

[87] Markus B Fröb and Jochen Zahn. Trace anomaly for chiral fermions via hadamard subtraction. *Journal of High Energy Physics*, 2019(10):1–40, 2019.

[88] D. B. Blaschke, A. V. Prozorkevich, C. D. Roberts, S. M. Schmidt, and S. A. Smolyansky. Pair production and optical lasers. *Phys. Rev. Lett.*, 96:140402, Apr 2006.

[89] C. Gabriel and P. Spindel. Quantum Charged Fields in (1+1) Rindler Space. *Ann. Phys.*, 284, 2000.

[90] J Dimock. Dirac quantum fields on a manifold. *Transactions of the American mathematical Society*, 269(1):133–147, 1982.

[91] Julian Schwinger. Coulomb Green's Function. *J. Math. Phys.*, 5:1606–1608, 1964.

[92] M. K. F. Wong and H. Y. Yeh. SIMPLIFIED SOLUTION OF THE DIRAC EQUATION WITH A COULOMB POTENTIAL. *Phys. Rev. D*, 25:3396–3401, 1982.

[93] Morris Edgar Rose and WG Holladay. Relativistic electron theory. *Physics Today*, 14(11):58, 1961.

[94] Paul C Martin and Roy J Glauber. Relativistic theory of radiative orbital electron capture. *Physical Review*, 109(4):1307, 1958.

[95] L_C Biedenharn. Remarks on the relativistic kepler problem. *Physical Review*, 126(2):845, 1962.

[96] MKF Wong and Hsin-Yang Yeh. Simplified solution of the dirac equation with a coulomb potential. *Physical Review D*, 25(12):3396, 1982.

[97] Jeng-Yih Su. Simplified solutions of the dirac-coulomb equation. *Physical Review A*, 32(6):3251, 1985.

[98] Robert Serber. Linear modifications in the maxwell field equations. *Physical Review*, 48(1):49, 1935.

[99] Alexei M Frolov and David M Wardlaw. Analytical formula for the uehling potential. *The European Physical Journal B*, 85(10):1–3, 2012.

[100] Retherford R. C. Lamb W. E. Quantum theory of gravity. i. the canonical theory. *Phys. Rev.*, 72:241, 1947.

[101] Ryoyu Utiyama and Bryce S DeWitt. Renormalization of a classical gravitational field interacting with quantized matter fields. *Journal of Mathematical Physics*, 3(4):608–618, 1962.

[102] Steven Weinberg. *The Quantum Theory of Fields*, volume 1. Cambridge University Press, 1995.

[103] A. Neagu. Path Integrals I. *Seria Seminarii De Fizica*, 1, 1995.

[104] J. Schwinger. The Theory of quantized fields, III. *Physical Review*, 91:728, 1953.

[105] Felix Berkhahn, Dennis D. Dietrich, and Stefan Hofmann. Cosmological Classicalization: Maintaining Unitarity under Relevant Deformations of the Einstein-Hilbert Action. *Phys. Rev. Lett.*, 106:191102, 2011.

[106] Sungmin Hwang and Dennis Schimmel. Vacuum Persistence in Fierz-Pauli Theory on a Curved Background. *Phys. Rev. D*, 92(4):044044, 2015.

[107] Daniel Baumann, Daniel Green, Hayden Lee, and Rafael A. Porto. Signs of Analyticity in Single-Field Inflation. *Phys. Rev. D*, 93(2):023523, 2016.

[108] B. Bellazzini, M. Burrello, M. Mintchev, and P. Sorba. Quantum Field Theory on Star Graphs. *Proc. Symp. Pure Math.*, 77:639, 2008.

[109] Robert Schrader. Finite propagation speed and causal free quantum fields on networks. *J. Phys. A*, 42:495401, 2009.

[110] Patricia Ribes Metidieri. Exploring quantum field theory in curved space-times with extended information networks. 2021.

[111] P. C. W. Davies and S. A. Fulling. Radiation from a moving mirror in two-dimensional space-time conformal anomaly. *Proc. Roy. Soc. Lond. A*, 348:393–414, 1976.

[112] P. C. W. Davies, S. A. Fulling, and W. G. Unruh. Energy Momentum Tensor Near an Evaporating Black Hole. *Phys. Rev. D*, 13:2720–2723, 1976.

[113] M. Castagnino and R. Ferraro. THE RADIATION FROM MOVING MIRRORS: THE CREATION AND ABSORPTION OF PARTICLES. *Annals Phys.*, 154:1–23, 1984.

[114] C. D. Fosco, F. C. Lombardo, and F. D. Mazzitelli. Quantum dissipative effects in moving mirrors: A Functional approach. *Phys. Rev. D*, 76:085007, 2007.

[115] Mark Srednicki. Entropy and area. *Physical Review Letters*, 71(5):666, 1993.

[116] Dimitrios Katsinis and Georgios Pastras. An inverse mass expansion for entanglement entropy in free massive scalar field theory. *The European Physical Journal C*, 78(4):1–18, 2018.

[117] Christophe Besse, Romain Duboscq, and Stefan Le Coz. Numerical simulations on nonlinear quantum graphs with the grafidi library. *arXiv preprint arXiv:2103.09650*, 2021.

[118] Thomas Klosch and Thomas Strobl. Classical and quantum gravity in (1+1)-Dimensions. Part 1: A Unifying approach. *Class. Quant. Grav.*, 13:965–984, 1996. [Erratum: Class.Quant.Grav. 14, 825 (1997)].

[119] W. G. Unruh. Notes on black hole evaporation. *Phys. Rev. D*, 14:870, 1976.

[120] Curtis G. Callan, Jr., Steven B. Giddings, Jeffrey A. Harvey, and Andrew Strominger. Evanescent black holes. *Phys. Rev. D*, 45(4):R1005, 1992.

[121] D. Grumiller, W. Kummer, and D. V. Vassilevich. Dilaton gravity in two-dimensions. *Phys. Rept.*, 369:327–430, 2002.

[122] Bruno Arderucio-Costa and William Unruh. Model for Quantum Effects in Stellar Collapse. *Phys. Rev. D*, 97(2):024005, 2018.

[123] Benito A. Juárez-Aubry and Jorma Louko. Quantum fields during black hole formation: How good an approximation is the Unruh state? *JHEP*, 05:140, 2018.

[124] D. W. Ring. A linear approximation to black hole evaporation. *Class. Quant. Grav.*, 23:5027–5037, 2006.

[125] Mark Srednicki. Entropy and area. *Phys. Rev. Lett.*, 71:666–669, 1993.

[126] Pierre-Louis MOREAU DE MAUPERTUIS. Accord de differentes loix de la nature qui avoient jusqu'ici paru incompatibles. *Histoire de l'academie royale des sciences et des belles-lettres de Berlin [pour l'annee], 1744*, pages 417–426, 1748.

[127] Christiaan Huygens. Traité de la lumière. 1690.

[128] P. A. M. Dirac. *The Principles of Quantum Mechanics*. Clarendon Press, 1930.

[129] Paul A. M. Dirac. The Lagrangian in quantum mechanics. *Phys. Z. Sowjetunion*, 3:64–72, 1933.

[130] Albert Einstein. Zur Elektrodynamik bewegter Körper. (German) [On the electrodynamics of moving bodies]. *Ann. Phys. (Berlin)*, 322(10):891–921, 1905.

[131] Ottavia Balducci, Stefan Hofmann, and Maximilian Koegler. Dark Matter Jets of Rotating Black Holes. 2022. Manuscript in preparation.

[132] Oscar Adriani et al. An anomalous positron abundance in cosmic rays with energies 1.5-100 GeV. *Nature*, 458:607–609, 2009.

[133] M. Aguilar et al. First Result from the Alpha Magnetic Spectrometer on the International Space Station: Precision Measurement of the Positron Fraction in Primary Cosmic Rays of 0.5–350 GeV. *Phys. Rev. Lett.*, 110:141102, 2013.

[134] G. Ambrosi et al. Direct detection of a break in the teraelectronvolt cosmic-ray spectrum of electrons and positrons. 2017.

[135] F. Aharonian et al. Very high-energy gamma rays from the direction of Sagittarius A*. *Astron. Astrophys.*, 425:L13–L17, 2004.

[136] Christoph Weniger. A Tentative Gamma-Ray Line from Dark Matter Annihilation at the Fermi Large Area Telescope. *JCAP*, 1208:007, 2012.

[137] Lars Bergstrom, Torsten Bringmann, Martin Eriksson, and Michael Gustafsson. Gamma rays from heavy neutralino dark matter. *Phys. Rev. Lett.*, 95:241301, 2005.

[138] Lars Bergstrom, Torsten Bringmann, Martin Eriksson, and Michael Gustafsson. Gamma rays from Kaluza-Klein dark matter. *Phys. Rev. Lett.*, 94:131301, 2005.

[139] Dan Hooper, Albert Stebbins, and Kathryn M. Zurek. Excesses in cosmic ray positron and electron spectra from a nearby clump of neutralino dark matter. *Phys. Rev.*, D79:103513, 2009.

[140] Patrick Meade, Michele Papucci, Alessandro Strumia, and Tomer Volansky. Dark Matter Interpretations of the e+- Excesses after FERMI. *Nucl. Phys.*, B831:178–203, 2010.

[141] Lars Bergstrom, Joakim Edsjo, and Gabrijela Zaharijas. Dark matter interpretation of recent electron and positron data. *Phys. Rev. Lett.*, 103:031103, 2009.

[142] J. Lavalle, Q. Yuan, D. Maurin, and X. J. Bi. Full Calculation of Clumpiness Boost factors for Antimatter Cosmic Rays in the light of Lambda-CDM N-body simulation results. Abandoning hope in clumpiness enhancement? *Astron. Astrophys.*, 479:427–452, 2008.

[143] Junji Hisano, Shigeki Matsumoto, and Mihoko M. Nojiri. Explosive dark matter annihilation. *Phys. Rev. Lett.*, 92:031303, 2004.

[144] Lars Bergstrom. Dark Matter Candidates. *New J. Phys.*, 11:105006, 2009.

[145] Lars Bergstrom. Dark Matter Evidence, Particle Physics Candidates and Detection Methods. *Annalen Phys.*, 524:479–496, 2012.

[146] J. Gariel, M. A. H. MacCallum, and N. O. Santos. Kerr geodesics, the Penrose process and jet collimation by a black hole. 2010.

[147] Kuantay Boshkayev and Daniele Malafarina. A model for a dark matter core at the Galactic Centre. *Mon. Not. Roy. Astron. Soc.*, 484(3):3325–3333, 2019.

[148] W. N. Brandt and D. M. Alexander. Supermassive Black-Hole Growth Over Cosmic Time: Active Galaxy Demography, Physics, and Ecology from Chandra Surveys. *Proc. Nat. Acad. Sci.*, 107:7184, 2010.

[149] Sean Tulin and Hai-Bo Yu. Dark Matter Self-interactions and Small Scale Structure. *Phys. Rept.*, 730:1–57, 2018.

[150] Brian P. Dolan. Pressure and volume in the first law of black hole thermodynamics. *Class. Quant. Grav.*, 28:235017, 2011.